

DESIGN OF MINI SWIMMING ROBOT
USING PIEZOELECTRIC ACTUATOR

A THESIS SUBMITTED TO
THE GRADUATE SCHOOL OF NATURAL AND APPLIED SCIENCES
OF
MIDDLE EAST TECHNICAL UNIVERSITY

BY

SAFAKCAN TUNÇDEMİR

IN PARTIAL FULFILLMENT OF THE REQUIREMENTS FOR
THE DEGREE OF MASTER OF SCIENCE

IN

MECHANICAL ENGINEERING

DECEMBER 2004

Approval of the Graduate School of Natural and Applied Sciences.

Prof. Dr. Canan Özgen
Director

I certify that this thesis satisfies all the requirements as a thesis for the degree of Master of Science.

Prof. Dr. Kemal İder
Head of Department

This is to certify that we have read this thesis and that in our opinion it is fully adequate, in scope and quality, as a thesis for the degree of Master of Science.

Prof. Dr. Abdulkadir Erden
Co-Supervisor

Prof. Dr. Faruk Arınç
Supervisor

Examining Committee Members

Prof. Dr. H. Nevzat Özgüven (METU, ME) _____

Prof. Dr. Faruk Arınç (METU, ME) _____

Prof. Dr. Abdulkadir Erden (METU, ME) _____

Assoc. Prof. Dr. Mehmet Önder Efe (ETU, EEE) _____

Asst. Prof. Dr. Ahmet Bugra Koku (METU, ME) _____

I hereby declare that all information in this document has been obtained and presented in accordance with academic rules and ethical conduct. I also declare that, as required by these rules and conduct, I have fully cited and referenced all material and results that are not original to this work.

Name, Last Name :

Signature :

ABSTRACT

DESIGN OF MINI SWIMMING ROBOT USING PIEZOELECTRIC ACTUATOR

Tunçdemir, Safakcan

M.S., Department of Mechanical Engineering

Supervisor : Prof. Dr. Faruk Arinç

Co-Supervisor: Prof. Dr. Abdulkadir Erden

December 2004, 128 pages

This thesis deals with the design, fabrication and analysis of a novel actuator for a fish-like swimming mini robot. The developed actuator is tested on a mini boat. The actuator relies on a novel piezoelectric ultrasonic motor, developed according to the design requirements of actuator for fish-like swimming mini robots. Developed motor is within the dimensions of 25x6x6 mm in a simple mechanical structure with simple driving circuitry compared to its predecessor. Bidirectional rotation of the motor is transformed to a flapping tail motion for underwater locomotion in a simple mechatronic structure. The simplicity in the motor and actuator enables further development on the miniaturization, improvement on the performances as well as easy and low cost manufacturing. The developed actuator is a candidate to be used in mini swimming robot with fish-like locomotion.

Keywords: swimming robot, mini robot, piezoelectric, actuator, ultrasonic motor, frequency matching.

ÖZ

PIEZOELEKTRİK EYLEYİCİ KULLANARAK YÜZEN MINI ROBOT TASARIMI

Tunçdemir, Safakcan

Yüksek Lisans, Makine Mühendisliği Bölümü

Tez Yöneticisi : Prof. Dr. Faruk Arınç

Ortak Tez Yöneticisi: Prof. Dr. Abdulkadir Erden

Aralık 2004, 128 sayfa

Bu tez, baligimsi yüzüğe sahip mini bir robot için düşünülmüş yeni bir tür eyleyici sistemin tasarımını, üretimini ve analizini içerir. Tasarlanan eyleyici minyatür bir tekne üzerinde uygulanmıştır. Eyleyici, baligimsi yüzüğe sahip mini robotlarda kullanılacak eyleyicilerin tasarım gereksinimlerine göre geliştirilmiş yeni bir tür piezoelektrik ultrasonik motora dayanmaktadır. Gelistirilen motor 25x6x6 mm boyutlarındadır ve öncüllerine göre yalın bir sürücü devresi ile yalın bir mekanik yapısı vardır. Motorun iki yönlü dönüşü, basit bir mekatronik yapı içerisinde su altında itki elde etmek için kuyruk salinimine dönüştürülür. Motorun ve eyleyicinin yalınlığı daha fazla minyatürleştirme için geliştirmeye ve performans artımına olanak sağladığı gibi kolay ve ucuz üretime de olanak sağlar. Gelistirilen eyleyici, baligimsi yüzüğe sahip mini robotlarda kullanılmaya adaydır.

Anahtar Kelimeler: Yüzen robot, mini robot, piezoelektrik, eyleyici, ultrasonik motor, frekans esleme.

To My Father

ACKNOWLEDGEMENTS

Firstly, I would like to express my gratitude to my professor, Prof. Dr. Abdulkadir Erden for his guidance, suggestions and support in my walk through the fascinating world of mechatronics which results in this thesis. I owe to thank to Dr. Burhanettin Koç for all the inspiration, initiative force and supervision even from the other side of the world and introducing me to piezoelectrics; without him this study would not have reached to this point. Special thanks to Onur Soysal for his generous brotherhood, in any time ready to partake the nights, dreams, frustrations and plans which are the main motivation of my study when I feel alone. I would like to thank to Necati Deniz Yücel with whom I could apply section breaks to the study. Also I would like to thank to Serkan Güroglu, Kutluk Bilge Arikan and Ali Emre Turgut since they never avoided sharing their unique experiences as an elder. Övünç Okyay, Ömer Emre Tokel and my lovely sister Sebnem Tunçdemir who helped me to resist the life when it can not be anticipated, are the hidden heroes and heroin of this study.

This work was partially supported by the Scientific and Technical Research Council of Turkey, TUBITAK through Contract No: MISAG-209. Contributions of International Center for Actuators and Transducers (ICAT) at Pennsylvania State University are also acknowledged, for providing piezoelectric ceramics and adhesive chemicals. These sources of support are gratefully acknowledged.

Finally many thanks to my parents for their invaluable and endless support.

TABLE OF CONTENTS

ABSTRACT.....	iv
ÖZ	v
ACKNOWLEDGEMENTS	vii
TABLE OF CONTENTS	viii
LIST OF FIGURES	xii
LIST OF TABLES	xv
1. INTRODUCTION.....	1
1.1 Fish Locomotion	2
1.2 Locomotion in SR Using Fish-Like Propulsion.....	4
1.3 Scaling Down the Swimming Robots	5
1.4 Features and Applications of Swimming Robots	6
1.5 State of Art in SRFL.....	8
1.6 Motivation of the Thesis	9
1.7 Scope of the Thesis	9
1.8 Organization of the Thesis	9
2. LITERATURE SURVEY	11
2.1 SRFL with Electromagnetic Actuators:	13
2.2 Hydraulic Driven SRFL.....	19
2.3 SFRL with Semi-Free Stirling Piston.....	20
2.4 SRFL with Shape Memory Alloy Actuator.....	21
2.5 Muscle Powered SRFL.....	23

2.6 SRFL with Ionic Polymer Actuators	24
2.7 Piezoelectrically Actuated SRFL.....	26
3. PRELIMINARY DESIGN	30
3.1 Design Specification	30
3.1.1 Fish-like swimming.....	30
3.1.2 Small scale (miniaturization)	31
3.1.3 Broad range for tail-beat frequency and amplitude.....	32
3.2 Design Constraint	36
3.2.1 Constraint on Dimension and Weight	36
3.2.2 Effects of Downscaling on the SRFL.....	37
3.2.2.1 Unavailability of EMM for small scale SRFL...	40
3.2.2.2 Comparison of the available actuation mechanisms for small scale SRFL.....	41
3.3 Piezoceramics	43
3.3.1 Externally leveraged.....	45
3.3.2 Internally leveraged	45
3.3.3 Frequency leveraged	46
4. ACTUATOR DESIGN	47
4.1 Design of Piezoelectric Ultrasonic Motor: Resonator Design	47
4.1.1 Overview	50
4.1.2 Symmetric PZT/Elastic Cantilever Laminate	54
4.1.3 Derivation of Equation of Motion for Longitudinal Vibration of Bimorph Beam.....	56

4.1.4 Derivation of Equation of Motion for Lateral Vibration of Bimorph Beam	59
4.1.5 Frequency Matching on a Uniform Cantilever Bimorph..	62
4.1.6 Frequency Matching on a Tapered Cantilever Bimorph...	65
4.1.6.1 Approximate solution for the first three natural frequencies of longitudinal vibration using 6 modes	69
4.1.6.2 Approximate solution for the first three natural frequencies of bending vibration using 6 modes.....	70
4.1.7 Selection of the Bimorph Parameters for Constructing the Motor	73
4.2 Operating Principle of the Motor	74
4.3 Structure of the Motor	76
4.4 Fabrication of the Motor	79
4.5 Prototypes of the Motor	82
4.6 Driving Circuitry of the Motor.....	84
4.7 Measuring the Characteristics of the Motor	86
5. SWIMMING ROBOT.....	90
5.1 Flapping Tail Motion of Swimming Robot.....	90
5.2 Structure of Flapping Tail Actuator	90
5.3 Control of Angular Rotation	91
5.4 Test Boat as the Preliminary Design of Mini Swimming Robot	93
6. CONCLUSION	96
6.1 Discussion	96
6.2 Contribution of the Thesis.....	101

6.3 Suggestions for Future Work	102
REFERENCES	103
APPENDIX A - OBTAINING L1	116
kl_ml.m	116
t_freqL1.m.....	118
t_plotL1B3.m.....	118
APPENDIX B - OBTAINING B3	119
t_integrand_b.m.....	121
kb.m, mb.m.....	121
t_freqB3.m.....	121
APPENDIX C - CALCULATION of MOMENT of INERTIA of LOAD on MOTOR	122
APPENDIX D - MOTOR CHARACTERISTICS CALCULATIONS in MATLAB	124
APPENDIX E - FLAPPING ANGLE CONTROL USING PIC12F675	126

LIST OF FIGURES

Figure 1.1 Basic morphological features of a rover-predator fish.....	2
Figure 1.2 Classification of the basic swimming modes seen in fish.....	3
Figure 2.1 RoboTuna drivetrain and covered mock-up	14
Figure 2.2 Proteus with flapping foils in the test tank	14
Figure 2.3 BASS-III	15
Figure 2.4 Robofish.....	16
Figure 2.5 Two-joint controlled PPF-09	17
Figure 2.6 MHI real sized robot fish.....	18
Figure 2.7 Robot fish developed by BUAA	19
Figure 2.8 Structure of VCUUV	20
Figure 2.9 Flapping tail motion generation with SFPSE	21
Figure 2.10 SMA actuated lamprey robot	22
Figure 2.11 Basic operating principle of the muscle robot	23
Figure 2.12 Structure of the ICPF microrobot	24
Figure 2.13 Segmented artificial muscle with float	25
Figure 2.14 Magnification mechanism in MMR.....	27
Figure 2.15 Prototype of the miniature swimming vehicle	28
Figure 2.16 Four-Bar mechanism of miniature swimming vehicle	29
Figure 3.1 Mechanical model of ostraciform type swimming	31

Figure 3.2 Relationship between swimming velocity and frequency of caudal undulations (tail-beats) for dace (<i>Leuciscus leuciscus</i>).....	32
Figure 3.3 Forward swimming speed vs. tail-beat oscillation frequency characteristics of some swimming robots utilizing BCF type locomotion..	33
Figure 3.4 Thunder [®] Model TH 8-R	45
Figure 4.1 Energy flow schema of locomotion.....	48
Figure 4.2 Basic construction of piezoelectric ultrasonic motor.....	48
Figure 4.3 Structure of the motor given in (Tomikawa, 1992).....	52
Figure 4.4 Structure of the motor given in (Aoyagi and Tomikawa 1993).....	52
Figure 4.5 Rod type UM	53
Figure 4.6 The motor based on serial bending arms	53
Figure 4.7 Two different geometry proposed for the cantilever beam.....	54
Figure 4.8 Three layered symmetric piezoelectric/elastic laminate (cantilever bimorph) structure with coordinate axes and basic dimensioning	55
Figure 4.9 Forces on a small section of a beam in longitudinal vibration.....	56
Figure 4.10 Forces on a small section of a beam in transverse deflection.....	60
Figure 4.11 Natural frequencies of longitudinal and bending modes vs. elastic layer thickness.....	64
Figure 4.12 Natural Frequency (L1-B3) vs. the tapering ratio (b_0/b_1) for various thickness of resonator	72
Figure 4.13 ATILA simulation of the motion of the resonator excited by a single piezoelectric layer	75
Figure 4.14 Exploded view of the solid model of the motor.....	78
Figure 4.15 2-D machined components of motor prototypes.....	80

Figure 4.16 Resonators of prototypes	81
Figure 4.17 Pictures of the prototypes of motor.....	83
Figure 4.18 Driving circuitry of motor.....	85
Figure 4.19 Block diagram of the measuring system.....	86
Figure 4.20 Rotary inertia and encoder disk mounted on the motor.....	87
Figure 4.21 Transient speed under no-load condition.....	89
Figure 4.22 No-load characteristics of motor: Transient speed and power as a function of torque	89
Figure 5.1 Block diagram of the flapping-tail actuator	92
Figure 5.2 Components of the swimming robot.....	94
Figure 5.3 Test Boat and the fin attached actuator.....	94
Figure A.1 Flowchart of the method for obtaining L1 frequency explicitly.....	116
Figure B.1 Flowchart of the method for obtaining B3 frequency numerically...	119
Figure D.1 Flowchart of the algorithm followed for obtaining motor characteristics from angular speed data via real-time data acquisition card.....	124
Figure D.2 Matlab Simulink [®] model for real time data acquisition.....	124
Figure E.1 Flowchart of the flapping angle control algorithm.....	126

LIST OF TABLES

Table 2.1 Scales and utilized actuators of swimming robots with fish like locomotion.....	12
Table 3.1 Locomotion and dimensional characteristics of swimming robots.....	34
Table 3.2 Summary of the effect of scaling on some physical quantities	38
Table 3.3 Merits and demerits of piezoelectric actuation	44
Table 4.1 The material properties of metal and piezoelectric layers	65
Table 4.2 Dimensions of the symmetric piezoelectric/elastic laminate cantilever structure	74
Table 5.1 Weight and power requirements of the components.....	95
Table A.1 Functions used in the solution given in Appendix B	117
Table B.1 Functions used in the solution given in Appendix B.....	120

CHAPTER 1

INTRODUCTION

One of the theories that elucidate the question of where the life begins on earth claims that the initial form of life appeared in water. Although the ancestors of humankind had left the water millions of year ago, the growing transportation and resource needs of human beings, force them to focus on water. However, the difficulty in moving and locomotion in water hindered the utilization of waters.

The technological advancements on aquatic vehicles have exploited the movement capability of human in water. The robots, which are the intelligent connection of perception to action, increase their importance among the aquatic vehicles due to their superior mobility.

Although the majority of aquatic vehicles operate at the surface, the aquatic robotics studies are mostly focused on submersible floating type vehicles which are not confined to move on the bottom or on the surface (Dudek and Jenkin, 2000). Thus, submersible types extend the maneuverability.

Propellers, Forming jet and Deformable bodies are three main ways of generating propulsive forces for momentum transfer in submerged aquatic vehicles. Fish swimming has been directly related with deformable bodies and has been modeled as a waving plate since the studies of Lighthill (1960) and Wu (1960; 1971). Although propeller and water-jet systems have high efficiency at high speed, they lack this feature in low speeds (Tsai and Lo, 2002).

Waters of the world are dominated by about 30000 species of fishes through a marvelous variety of morphological, physiological and behavioral adaptations.

Thus, natural selection has ensured that the locomotion systems evolved in fish are highly efficient considering the extraordinary array of habitat of fishes. Although not optimal but highly efficient swimming mechanisms of fish, should guide the designers in the propulsion systems of swimming robots. Moreover, today there is an increasing effort on the swimming robots mimicking the various fish swimming modes in order to obtain highly maneuverable, efficient and stealthy platforms (Sfakiotakis et al., 1999). In this study, fish-like aquatic robots will be discriminated from the aquatic robots and will be named as swimming robots (SR). SR is defined by Yu et al (2004) as the fish-like aquatic mobile robot that is based on the swimming skills and anatomic structure of a fish.

1.1 Fish Locomotion

In order to swim, fish utilize various mechanisms. The main idea of all fish swimming mechanisms is generating an oscillatory based wake consisting of alternating vortices arranged in a jet pattern. The diversity of mechanisms depends on the wide variety of the body form of the fish because body shape determines the way of manipulating the wake. Rover-predators have the shape that is commonly used in literature and seen in nature. For assisting the identification and description of locomotion, Figure 1.1 is given with the basic morphological features of fish.

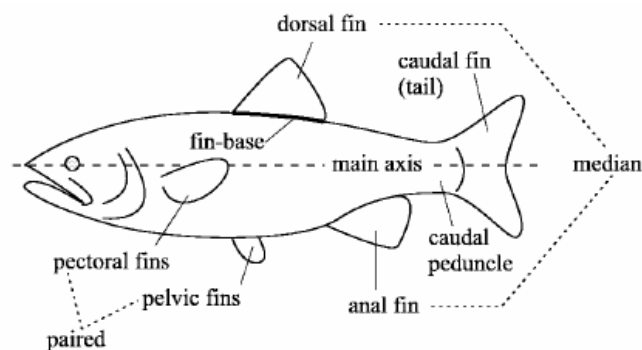


Figure 1.1: Basic morphological features of a rover-predator fish
(Sfakiotakis et al., 1999)

Figure 1.2, which is taken from the detail work of Sfakiotakis et al. (1999) summarizes and clarifies the swimming modes and the nomenclature that will be used in this study. In BCF (Body/Caudal Fin) mode, backward directed propulsive wave extending to the caudal fin generates the thrust by bending the body. Whereas, in MPF (Median/Paired Fin) mode thrust is generated by the undulatory waves passing down the fins (Moyle and Cech, 2004).

Despite the discrimination in the locomotion types, there is a continuum in two modes due to the derivation of the oscillatory movements from the gradual increase of the wavelength of the undulation. Most of the fish use both modes; one for the primary propulsor and other is the auxiliary. Nevertheless, forward propulsion mainly relies on BCF, while MPF provides stability and maneuverability (Moyle and Cech, 2004). Moyle and Cech divide the swimming modes into four basic types: (1) anguilliform, (2) carangiform, (3) ostraciform, (4) swimming with the fins alone (Moyle and Cech, 2004).

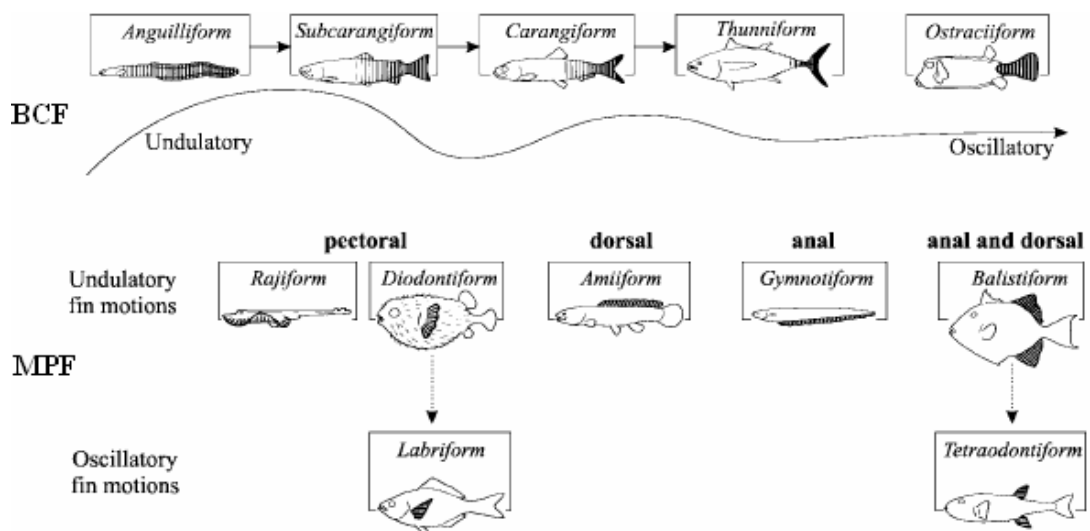


Figure 1.2: Classification of the basic swimming modes seen in fish (Sfakiotakis et al., 1999).

In **anguilliform**, the whole body is flexed into lateral waves as the propulsor. Thrust is produced by passing transverse wave from head to tail which allows backward swimming as reversing the direction of undulation. This type of locomotion is the typical of eels (*Anguilliformers*), lampreys and invertebrate amphioxus.

For **carangiform** type, undulation of the entire body which grows toward the tail is involved in locomotion. Jacks (*Carangidae*), mackerel and snapper are carangiform swimmers with a tall and forked tail attached to a narrow peduncle. Fish that have narrower, low drag, fusiform body shape with slim, lunate caudal fin are called as *thunniform* swimmers (lamnid sharks, billfish and tuna fish). While thunniform swimmers are the fastest of all, *subcarangiform* is on the other extreme of the carangiform with their slower speed characteristics and more body parts that is included in the undulation.

Ostraciform swimmers, like cowfish, trunkfish and boxfish (*Ostraciidae*) have a still body and a rigid fin swinging around a narrow peduncle to produce sculling type locomotion. Non-moving part of these fish are about the three fourths of the total body length.

Fish in **Swimming with fins alone** (MPF) category utilize the undulatory fin motions. The subcategories of this swimming mode are due to the location of the thruster fins as at pectoral, dorsal or anal regions. *Labriiform* (in *Labridae*) swimming includes the rowing and flapping motion of the separate pectoral fins for forward propulsion. *Rajiform* is the unique style of batoid fish (skate and ray) in which thrust is generated by undulatory waves passing down the enlarged wing-like fins.

1.2 Locomotion in SR Using Fish-Like Propulsion

In order to investigate and mimic fish-like locomotion, oscillating foil has been proposed as an alternative propeller to the conventional screw type propellers.

As a consequence of the studies of the group in MIT (Massachusetts Institute of Technology) beginning with (Triantafyllou et al., 1991) it was proven and demonstrated that power required to propel an actively swimming fish-like body was significantly smaller than the power required to tow the rigid body at the same speed. According to the operational requirements of the robot, the locomotion system can be designed to mimic any of the swimming modes in Figure 1.2. As stated and historically summarized by Colgate and Lynch (2004), most of the studies of *Swimming Robots with Fish-Like Locomotion (SRFL)* focus on carangiform due to the proved efficiency and strong background and research on the model of caudal fin movement initiated by RoboTuna (Barret et al., 1999). Another reason for this is easier control, modeling and mimicking of BCF than MPF. Whether the swimming mode is oscillatory or undulatory, actuators are required to swing. As the full rotation is not the primary concern of the fish-like locomotion contrary to the conventional screw type propellers, novel actuation mechanism are required for these robots. Actuator designs vary not only in mechanism design but also in the utilization of smart materials. The need of elaborate transmission systems for adequate torque/speed characteristics and noisy operations of electric motors foster the interest on developing novel actuation mechanisms and *smart muscle* (Madden et al., 2004), (Colgate and Lynch, 2004). Detailed analysis and applications of novel actuation mechanisms and utilization of smart materials in locomotion of SRFL will be presented in Chapter 2.

1.3 Scaling Down the Swimming Robots

Scaling down the robots is easier today as the consequence of the recent advances in the precise process and material technology (Fearing, 1992) and (Ishihara et al., 1996). Same as the other types of robots (terrestrial mobile, aerial, space, *etc.*), miniaturization of the swimming robots is a requirement mainly for decreasing the cost and exploiting the application domains. However, downscaling does not always enhance the features of the robots (Caprari, 2003).

As the size of the robot decreases, free volume for the required power sources decreases drastically. Free volume for the power sources limits the stored energy for operations and therefore the endurance limit of the robot (Trimmer and Jebens, 1989). Another problem arises with the downscaling of robots is the scaling effects on actuating forces. Miniaturized actuators sometimes suffer from the downscaling effects. These effects are investigated and summarized previously by Trimmer and Jebens (1989), Flynn et al. (1990) and Caprari (2003). Authors imply that the problems arose from these effects are avoided not only with the advanced power supplies but also by the help of improved hull design and novel actuator systems that increase the efficiency.

In order to benefit from the advantages of the miniaturized robots, emphasis will be placed on the small scale swimming robots with fish-like swimming, through the rest of the study. The effects of miniaturization in swimming robots will be investigated briefly in Chapter 3, taking the downscaling of robots as a design specification. Based on the previous studies (Bainbridge, 1958, Triantafyllou et al., 1991, Sfakiotakis et al., 1999, Moyle and Ceché, 2004, Colgate and Lynch, 2004), on the relation between body length, swimming speed and tail beat frequency, operating frequency range will be investigated as another actuator requirement for small scale swimming robots in Chapter 3.

1.4 Features and Applications of Swimming Robots

Swimming robots are mostly utilized in the physical domains where man can not operate safely due to physical limitations. Increased speed and payload capacity, reduced noise, independency to a tow cable, improved efficiency and endurance are key features of swimming robots which significantly expands the application area. Oceanographic technologies, marine-life inspection, pipeline inspection, entertainment, medical field and military applications are the most popular application areas of swimming robots.

In the field of **oceanographic studies**, although unmanned underwater machines are highly commercialized today (Videoray, 2004), the absence tow cable promised to increase the speed and range of the operation significantly with micro swimming robots. With the included perceptive and autonomous properties, they can be used more widely in various areas of oceanographic studies such as deep sea measurements, resource investigation *etc.* (Anderson and Kerrebrock, 1999), (Hirata, 2000).

Swimming robots using fish-like propulsion are already used in **marine life inspection** without disturbing the observed environment as behaving like one of the natural members of it. Robot Shark is one of the successful examples of this type of application (Robot Shark, 2004). Hirata (2002) proposes that migration paths of the whales or other sea animals would be inspected by utilizing the emerging swimming robots.

Due to the high maneuverability and autonomous features of the small scaled swimming robots, they have important roles on the **inspection of underwater pipelines** as stated in (Fukuda *et al.*, 1990) and (Kato and Furushima, 1996).

With the reduced cost of scaled down swimming robots, they will be more appropriate to be mass produced and to be commercialized for toy industry and for **entertainment purposes**. A real sized lifelike robot fish, sea-bream presented by Mitsubishi Heavy Industry (MHI, 1995) is a successful example of aqua-mechatronics in the field of entertainment. Japanese Toy Company, Takara's Fish Robot, Aquaroid, is one of the commercialized fish robot products (Aquaroid, 2004).

Compared to the conventional screw type propellers, swimming robots using fish-like locomotion generates less noise. VCUUV (Vorticity Controlled Unmanned Underwater Vehicle) is suggested for mine reconnaissance operations as well as surveillance operations in military fields (Anderson and Kerrebrock, 1999). Moreover, the miniaturized structure and the fish-like swimming make the robots to be camouflaged easily for stealthy and surveillance operations.

Due to the precise movement of the micro swimmers, they are appropriate for **surgical operations** avoiding unnecessary incisions. Edd *et al.* (2003) propose a swimming robot which is capable of operating inside the veins.

1.5 State of Art in SRFL

In the last decade, the studies on swimming robots mostly aimed to clarify the principles of fish swimming in order to utilize the biomimetic locomotion. The results of these studies revealed the already known theoretical facts that the numerous advantages of fish swimming over the conventional propellers. 200cm-sized to 10 cm sized swimming robots with fish-like swimming (SRFL) were prototyped and heavily tested in the past decade. Most famous ones are VCUUV of Charles Stark Draper Laboratories (Anderson and Kerrebrock, 1999, 2000), Robot Tuna and Robot Pike of MIT-Towing Tank (Towtank, 2004). However, today, the biomimetic swimming robot studies are mostly concentrated on the miniaturization. In order to avoid the problems of conventional actuators due to the miniaturization, novel actuator designs are being developed with great effort by different research groups all around the world. Ayers *et al.* (2000) at Northeastern University in US develop SMA (Shape Memory Alloy) actuators for their lamprey robots. Denis and Herr (2000) implement real muscles to swimming mini robot at MIT, US. Guo *et al.* (2003) build mini swimming robot with ICPF (Ionic Conductor Polymer Film) actuators in Japan. Mojarrad (2000) utilizes artificial polymeric gels for underwater locomotion. Sitti and Behkam (2004) built a real-sized prototype of surgical micro-robot which imitates the swimming of bacterium.

Despite the successful examples of prototype SRFL using smart actuators, scaling down the SFRL is still a standing goal to exploit the unique designs of biological systems. Miniaturization of swimming robots by utilizing smart actuation mechanism is the recent trend of swimming robot studies.

1.6 Motivation of the Thesis

The motivation of the thesis is the need of a novel actuator mechanism for mini swimming robot design in order to respond the further miniaturization demand on these robots.

1.7 Scope of the Thesis

This thesis aims mechatronic design of a novel actuation mechanism utilizing piezoelectric actuators for mini swimming robot. Downscaling effects on the actuators of swimming robots are discussed for indicating the advantages of piezoelectric actuators as well as their shortcomings for better understanding of the problem. Comparative analysis of a certain class of ultrasonic motors is done and a novel ultrasonic motor which is applicable for mobile robotics is devised. Improving the performance of the actuator was out of scope of the thesis due to lack of funding and facilities. Low performance motor is applied on the prototype swimming robot and preliminary measurements are performed with the actuator which is a completely novel design contributed by this thesis study.

1.8 Organization of the Thesis

In Chapter 2, overview of SRFL in literature is presented. Actuator dependency of the miniaturization and the swimming speed modulation is observed.

In Chapter 3, design specifications are stated and the constraints on the design are given. Preliminary design is carried out with these criteria which are based on the requirements given throughout the chapter and the findings of the Chapter 2.

In Chapter 4, the structure of the actuator is proposed. Piezoelectric ultrasonic motor design and fabrication are presented. Although it was not utilized in the present design, a novel methodology is developed for frequency matching on a piezoelectric bimorph.

In Chapter 5, implementation of the actuator to the robot is given with initial tests and measurements of the actuator system including the motor.

In Chapter 6, some concluding remarks are stated on the performance of actuator and the robot.

CHAPTER 2

LITERATURE SURVEY

As stated in Chapter 1, there is an increased interest in the use of Swimming Robots (SR) for various fields. Efforts on miniaturization of SR for exploiting the application domain as well as other mobile robots are also considerable. On the other hand, conventional rotary propellers can not serve the needs of further miniaturization and high maneuverability while sustaining the long-endurance and stealth. Due to the enviable performances of fish (high efficiency even at micro scales, great maneuverability, high acceleration and noiseless motion *etc.*), swimming robots with fish-like locomotion (SRFL) are being developed by several research groups. The main goal of the biomimetically actuated swimming robot studies is to achieve more efficient and more maneuverable locomotion than the conventional propellers. Since, there is no evidence that one locomotion mode is superior to others, locomotion types of biomimetic swimming robots vary from MPF to BCF. However, carangiform mode is used most due to the oscillatory behavior of it leading to the simplicity in mimicking the motion by reduced number of actuators. Nevertheless, the primary concern in swimming robot studies is not reducing the number of actuators but developing novel mechanisms considering the reduction in size.

As an amalgam of bio-mechanics and engineering, SR studies are multidisciplinary field that mainly involve hydrodynamics-based-control and actuation technology. In SR studies, dimensional characteristics of robot are mainly dependent on the utilized actuator as well as the imitated locomotion type. As seen in Table 2.1, utilizing conventional type actuators in SRFL becomes inappropriate as the scale goes down from macro to mini/micro.

Table 2.1: Scales and utilized actuators of swimming robots with-fish like locomotion

Actuator	Micro 10 mm	Mini 100 mm	Macro 1000 mm
Electromagnetic			2.1.1 RoboTuna 2.1.2 BASS 2.1.7 Coalecanth 2.1.8 BAUV 2.1.9 SPCII
Hydraulically Driven			2.1.3 RoboFish 2.1.4 BRF 2.1.6 NMRI 2.1.7 Sea Bream 2.1.9 Robot-eel 2.2.1 VCUUV
Semi-Free Stirling Engine			2.3.1 NMRI-SFSE
Shape Memory Alloy			2.4.1 Lamprey 2.4.2 Robo-Ray
Muscle Powered			2.5.1 Biomechatronics
Ionic Polymer		2.6.1 ICPF 2.6.2 IPMC 2.6.3 Soft Robot 2.6.4 IEMMC	
Piezoelectric		2.7.1 MMR	2.7.2 MSV

Since the aim of thesis is to design a mini swimming robot, this chapter is devoted to the detailed literature survey about SRFL by classifying the robots according to the utilized actuator, locomotion type and size rather than the hydrodynamics and control point of view. Although, in actuator technology, active or “smart” materials have opened new horizons in terms of actuation simplicity, compactness and miniaturization potential, most of the devices used in the previous work utilized conventional systems of gears and servomotors to provide the actuation power. Conventional methods leave little interior room for control systems and payload. The studies based on conventional systems in the existing literature have been crucial in developing an understanding of the hydrodynamics of fish-like swimming (Triantafyllou *et al.*, 2000). For this reason, ignoring the size of the robots and test apparatus, these systems are investigated under the title of Electromagnetic Actuators.

Some typical research will be summarized in the following sections:

2.1 SRFL with Electromagnetic Actuators:

The largest group of swimming robots utilizing fish-like locomotion is the one using electromagnetic actuators. DC motors and DC servo motors are classified under this group. Because of the availability of these actuators with improved performance over years, most of the mobile robotic studies are carried out with these actuators. As seen in Table 2.1, these actuators dominate swimming robot studies in number.

2.1.1 MIT RoboTuna and Robot Pike are the two successive robots as the resultant of the studies in MIT-Towing Tank Laboratory on the detailed measurements of the forces on actively controlled structure for modulating the vortex around the body (Triantafyllou and Triantafyllou, 1995, Barret et al., 1999, Towtank, 2004)

In 1994, Robot Tuna, an 8-link, 1.2 m biomimetic vehicle, is successfully, developed. It is accepted to be the first robot fish in the world. Robot Tuna has flexible posterior body and oscillating foil as a propeller. Thrust is generated by foil-flapping that mimics the thunniform swimming mode with a tail structure which is actuated by 6 brushless DC servomotors and cable-pulley systems. Each servomotor rates about 1.5 kW. The fundamental objective of the Robot Tuna control system is to produce a dynamic body motion that can realistically modulate the flow field that exists around a swimming biological tuna. The Robot Tuna's outer hull consists of a thin layer of flexible reticulated foam covered by a conformal lycra sock. Coating around the skeleton provides a smooth continuous free flexible outer hull. Robot Pike, as the successor of Robot Tuna, is not towed to tank and can swim freely at 6 m/s with acceleration rates of 8-12 g's. In addition to the fish-like robots developed in MIT Towing Tank Laboratory, sea-turtle or penguin-like swimming is imitated with flapping foils at rear end of a 3.4 m boat which is called Proteus (Towtank, 2004) (Figure 2.2).

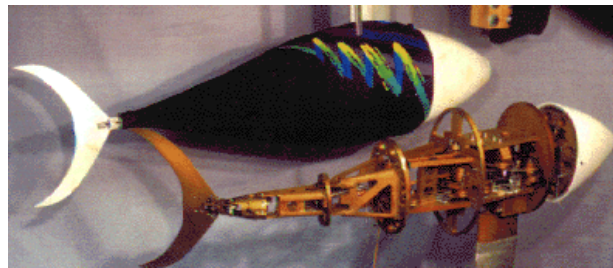


Figure 2.1: RoboTuna drivetrain and covered mock-up (Towtank, 2004)



Figure 2.2: Proteus with flapping foils in the test tank (Towtank, 2004)

In a deviation from actual penguin motion, Proteus uses vertically-oriented, rigid foils that move towards and away from each other, while also twisting much like two fish swimming side-by-side but out of phase. As a successor of RoboTuna, drive-train of Proteus are formed with four DC-servo motor and series of pulleys and cables.

2.1.2 BASS is the first prototype of Blackbass robots including the control of pectoral fin like mechanism as a propulsor (Kato and Furushima, 1996). Instead of thrust maximizing, the research on BASS aims to achieve highly maneuverable and stable underwater vehicle as in *labriform* type swimmers. In order to mimic oscillating pectoral fins which are used by many fish for their maneuvers at low swimming speeds, a pair of two-motor-driven mechanical pectoral fins is developed. Improving the design of 2 degree-of-freedom pectoral fins of BASSII (Kato, 2000), 3 degree-of-freedom BASSIII is presented by Kato et al in 2002 (Kato *et al.*, 2002). The locomotion of 2000 mm long BASS-III which is shown in Figure 2.3 relies on three-motor-driven mechanical pectoral fins. A *gimbal* structure is incorporated to allow three DC servo motors to independently generate the feathering, heaving and flapping motion of a rigid pectoral fin. Dimensions of the actuator unit are $375 \times 212 \times 400$ mm and weight of one unit is about 11 kg. If the oscillation frequency of the actuator is set to 0.5 Hz a forward speed of 50 mm/sec with negligible yaw angle change is recorded.



Figure 2.3: BASS-III (Kato, 2004)

2.1.3 Robofish, fully autonomous fish like swimming robot, is being developed in University of Washington aiming to build a platform for nonlinear control system design (Morgansen K., 2004a). Robofish, which is shown in Figure 2.4, mimics carangiform type swimming mode with its 2-DOF tail structure.

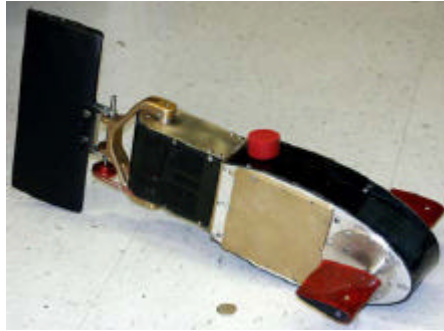


Figure 2.4: Robofish (Morgansen K., 2004a)

DC servo motors are powered and controlled onboard by a microcontroller. The whole body has a length of about 500 mm. Pectoral fins are used to propel as well as the oscillatory tail but only for the maneuvering purposes since forward locomotion with pectoral fins are not compromising. If the tail is beaten at 1.5 Hz, robot which is shown in Figure 2.4, can reach a forward speed of 600 mm/sec (Morgansen K., 2004b).

2.1.4 BRF is a 4-link and free-swimming biomimetic robot fish that uses a flexible posterior body and an oscillating foil as a propulsor was developed by the Laboratory for complex Systems and Intelligence Science of Chinese Academy of Sciences and Robotics Institute in Beijing University of Aeronautics and Astronautics. Robot has the dimensions of 400 mm in length, 78 mm in width and 40 mm in thickness and weighs about 500 gr. Maximum swimming speed in water, reaches to 0.32 m/s at the maximum frequency of 2 Hz with a lunate tail fin. Lunate tail and other joints are linked with aluminum exoskeleton. Radio-controlled robot is actuated by 4 DC servomotors. Motors are controlled by onboard microprocessor and a CPDL (Complex Programmable Logic Device).

The robot fish is partly submerged so that the balance, communication and buoyancy problems are avoided. Speed swimming is adjusted by modulating the joints' oscillating frequency, and its orientation is tuned by joints' deflections. Yu et al. (2003) concluded that speed increases with the oscillating frequency, but the maximum oscillating frequency is limited by the speed of the servomotors.

2.1.5 Fish Robot studies in NMRI (National Maritime Research Institute) in Japan aims to develop an intelligent marine robot and the application of fish locomotion to commercial ships (NMRI, 2000a). One of the prototypes developed in NMRI has 600 mm body length and mimics the carangiform type swimming mode by means of 3-joint tail structure (Hirata, 2000). 3 DC servomotors control the tail with a unique link mechanism. The prototype robot has been reported to swim 0.7 BL/s (body length per second) at frequency of 3 Hz. 2 degree-of-freedom tail structure of a new robot is actuated by two DC servomotors with Scotch-yoke mechanism (Hirata et al., 2000). Maximum swimming speed of 0.6 BL/s is reported to be due to the limited frequency (2.3 Hz max) and performance of servomotors. PPF-09, as an improved version of the robot which is shown in Figure 2.5, can reach to a top speed of 0.4 m/s at 10 Hz of oscillation frequency of tail (NMRI, 2000b). The requirement of high frequency range for high speed swimming is emphasized for all the robots (Hirata, 2000), (Hirata et al., 2000).

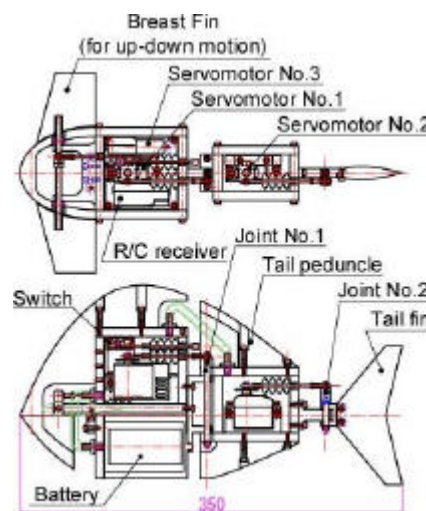


Figure 2.5: Two-joint controlled PPF-09 (NMRI, 2000-B).

2.1.6 MHI Real Sized Robot Fish constitutes of an oscillating fin propulsion system which was actuated by two-phase servo motors and belt systems (Yamamoto et al., 1993). Authors who are from Mitsubishi Heavy Industries LTD (MHI), Japan have revealed that the oscillating fin device can control both the thrust force and its direction, simultaneously. In addition, they showed that average thrust force increase in proportion to the oscillating frequency and stroke amplitude. An oscillating-drive device is developed for controlling the motion in sway and yaw directions (Yamamoto et al., 1995). In this work, an animatronic system including lifelike robotic fish, based on the technology of the flexible oscillating fin is presented. The fish-tail-type flexible fin is found to produce higher power compared with the same area of a rectangular rigid fin. The lifelike fish is controlled via a desktop computer by regulating the amplitude, frequency and phase of the joints of the fin. Two fish models shown in Figure 2.6 are developed. Sea-Bream type modern fish is 2.6 kg, 60 cm in length with a maximum speed of 0.25 m/sec while Coelacanth-type ancient robotic fish is 40 kg, 1.2 m in length with a maximum speed of 0.5 m/sec. Oscillating frequency of the fins of two fish is 0.2 and 1 Hz.



Figure 2.6: MHI real sized robot fish. a) Robot Sea-Bream and b) Robot Coelacanth

2.1.7 BAUV (Biomimetic Autonomous Underwater Vehicle) is locomoted by the undulatory motion of the flexible slender body which is totally 1.6 m in length (Chiu et al, 2002). The BAUV is divided to five segments: head, tail, fin and two pectoral fins. Six brushless DC servomotors are utilized to drive pectoral fins (2

for each) and joints between tail-head and fin-tail (1 for each). The robot can reach a forward mean speed of 150 mm/sec at beating frequency of 0.7 Hz. Speed of the vehicle is reported to be limited with the maximum operating frequency of the drivetrain (Chiu et al., 2002), (Guo et al., 2003).

2.1.8 BUAA (Institute of Robotics in Beihang University, China) robots, robot-eel and SPC-II are reported in (Dai, 2003). Remote control robot eel, shown in Figure 2.7 is 0.8 m long, and it can reach the maximum velocity of 0.75 BL/sec at the oscillation frequency of 2 Hz. In the same study Dai also reports a carangiform swimming robot, SPC-II which is shown in Figure 2.7.b. It weights 40 kg and has the length and height of 1210 mm and 510 mm. Robot can travel at 2000 mm/sec with DC powered actuators draining 300 W.

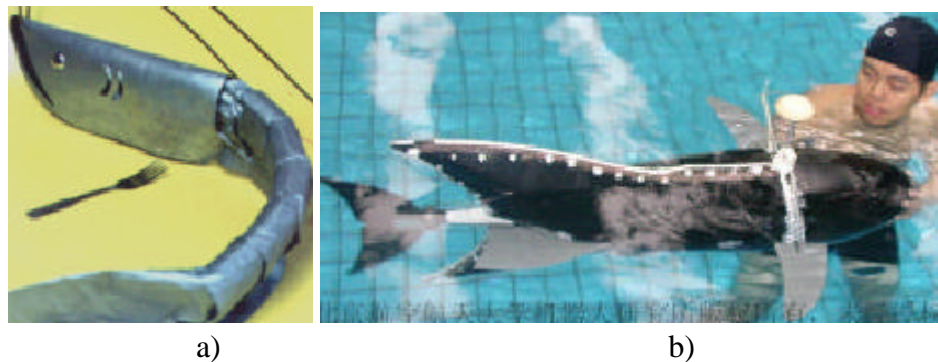


Figure 2.7: Robot fish developed by BUAA. a) eel-robot; b) SPC-II

2.2 Hydraulic Driven SRFL

In real sized applications, hydraulics can be successfully implemented in the locomotion with its linear stroke generation in high power densities

2.2.1 VCUUV (Vorticity controlled unmanned undersea vehicle) is developed in Charles Stark Draper Laboratory, US as a next generation of RoboTuna (Anderson and Kerrebrock, 1999, 2000). With its flexible hull, the autonomous fish-like swimming vehicle mimics the form and kinematics of a large yellow fin tuna possessing thunniform type motion. The localized tail motion due to the

thunniform swimming allows the front of the body be used as a rigid housing for energy, intelligence and drive-train. The vehicle is about 2.4 m in length, 0.5 m in height, 0.4 m in width and weighting 1334 N. The vehicle can reach up to 2.4 knots at oscillation frequency of 1 Hz. Three equal length links and the caudal fin which are actuated by a recirculating hydraulics system form the articulated tail structure as shown in Figure 2.8. Pectoral fins for dive control and stability are actuated by DC servo motors.

At present, the VCUUV is not intended to demonstrate advanced autonomy; thus, it operates in open loop, as pre-programmed to demonstrate the capability of simple swimming. Moreover, despite the success of the vehicle in real size application, miniaturization is out of concept for this work due to the difficulty of generating hydraulic power in a limited free-volume.

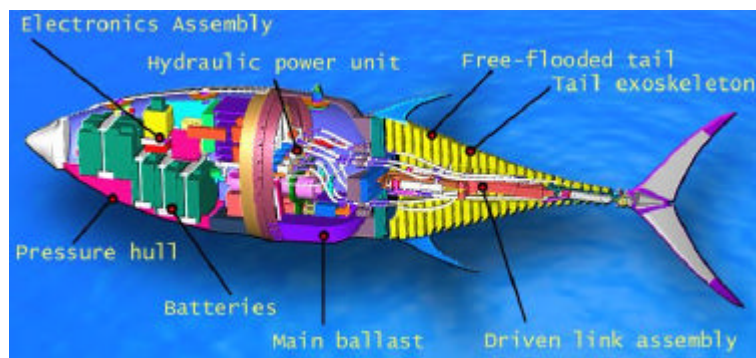


Figure 2.8: Structure of VCUUV (Anderson and Kerrebrock, 2000)

2.3 SFRL with Semi-Free Stirling Piston

SRFL with semi-free Stirling piston which will be presented in the next section is another example of swimming robots which is successful in macro domain but inapplicable for miniaturization as in the case of VCUUV.

2.3.1 SFPSE Fish Robot utilizes a semi-free piston Stirling engine (Hirata, 2001a). As shown in Figure 2.9 oscillating tail fin is directly driven by a reciprocating piston whose motion is due to electric motor via a displacer piston

(DP). Since the pressure difference on both side of the DP is very small, the power input to the electric is very small. If DP is driven to reciprocate with the same frequency as the resonant frequency of power piston (PP), the output stroke of PP becomes progressively greater.

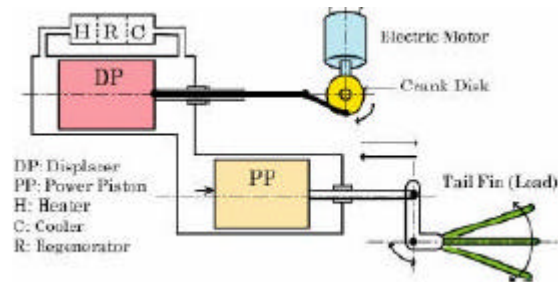


Figure 2.9: Flapping tail motion generation with SFPSE (Hirata, 2001b)

Actuator has the potential for long un-refueled operation because of both high energy efficiency potential of the engine itself and high energy density fuel availability. Engine operates in a frequency range of 0~12 Hz. When the engine is tested on an experimental boat in order to investigate the performance and any problems for adaptability for a fish robot, it was observed that maximum operating frequency degrades to 4 Hz. The total weight of the engine is about 2 kg. Top speed of 747 mm test boat is about 0.12 m/s at 3 Hz (Hirata, 2001a, 2001b).

2.4 SRFL with Shape Memory Alloy Actuator

Utilization of SMA in SRFL aims to increase the efficiency and durability even for small scale applications where electromagnetic actuators suffer and other two methods given in sections 2.2 and 2.3 are unavailable. General characteristic of the swimming robots utilizing SMA is their undulatory motion generation by means of an array of actuators.

2.4.1 Lamprey Robot is being developed under Biomimetic Underwater Robot Program of Marine Science Center in Northeastern University, US (Ayers, 2001).



Figure 2.10: SMA actuated lamprey robot

The vehicle is propelled by ten nitinol actuators forming an array of SMA wires affixed on each side. Wire arrays are staggered along the body axis, which allow the body to flex at any point and for flexion waves to propagate. Body shape of the developed lamprey robot is given with Figure 2.10. Thrust is regulated by modulation of the spatial range of wire-contraction which is achieved by providing current at different distances along the wire. Operation under water allows fast convective cooling necessary for the *nitinol martensite transition* of maximum 4 Hz (Ayers et al, 2000). However, response of the actuators is limited with the cooling speed and response is usually so slow to prevent the robot to reach high speeds whether the ambient is aquatic or not.

2.4.2 Robo-Ray is not a robot but a robotic model of one pectoral fin to mimic the swimming motion of the ray fish (*rajiform*) by using an actuated 2-D surface. The robot uses SMA wire array as linear actuators to manipulate the fin surface in the manner of muscles. SMA wires are attached to the main body of the robot in pairs as ventral and dorsal through eleven evenly spaced parallel cylindrical rods, *battens*. Parallel wires are driven with a phase shift to create a traveling wave on the fin surface while the counter wires in a batten are driven to reshape each muscle. Body length of the pectoral fin is 46 cm and has a beating frequency of 1.29 Hz. The model is tested in British Columbia Research Institute Tow Tank and only the indications of thrust are observed but self-propulsion can not be obtained.

The requirement of controlling the temperature of SMA array in water makes them inefficient and difficult to control. While the heat input to SMA can be controlled easily, factors effecting the cooling of actuators can not be easily modulated.

2.5 Muscle Powered SRFL

The development of functional biomechatronics prototypes with integrated musculoskeletal tissues is the initial threshold toward the long term objective of controllable and robust hybrid biomechatronic actuation. The Biomechatronics Group at MIT built a muscle-powered fish robot (Biomechatronic, 2004).

2.5.1 Muscle Robot utilizes a single pair of whole muscle explants from frog semitendinosus muscle as the actuator (Herr and Dennis, 2004). Single degree of freedom system (despite making use of two actuators), whose layout is shown in Figure 2.11, has 120 mm whole length and 70 mm of it is rigid. The robot performed maximum straight-line swimming speed of 40 mm/sec. Surface swimming is accomplished by modulating electrical signals to each muscle actuator across two electrode pairs, one on each muscle. Tail-beat frequency is 3.1 sec^{-1} . System drains 45 mAh and 6 V. Fatigue of the bioactuators (frog muscle) which are operating outside of their natural environment (tissue) is the critical deficiency of the design. Within a 42 hours lifespan with % 10 duty cycle, muscle loses its functionality.

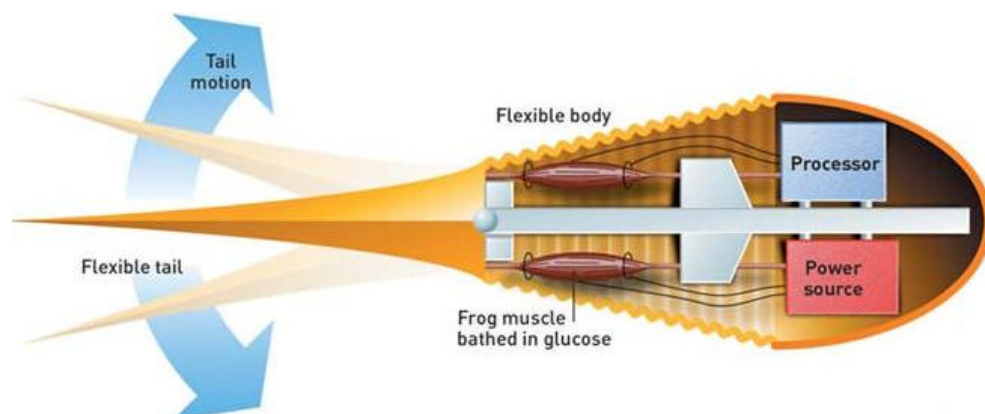


Figure 2.11: Basic operating principle of the muscle robot (New Scientist, 2001).

2.6 SRFL with Ionic Polymer Actuators

Guo et al. (1997), Laurent and Piat (2001), Nakabo et al. (2004) and Mojarrad and Shahinpoor (1997) present successful SRFL, utilizing ionic polymer actuators. These actuators deflect as a response to the voltage applied on the surfaces of polymer composites.

2.6.1 ICPF (Ionic Conducting Polymer Film) actuator is proposed as a biomimetic fish-like propulsion unit by Guo et al. (1997). ICPF is a kind of high polymer gel actuator that works only in wet conditions and known as ion exchange membrane. Fins attached to the tails are driven separately by ICPF actuators. The robot, shown in Figure 2.12, is totally 45 mm in length, 10 mm in width and 4 mm in thickness while the total length of undulating part (tail and fin) is 30 mm. Changing the driving frequency and applied voltage at each ICPF, combined motion of tail is modulated to control steering in 2-D. An additional ICPF is used for adjusting the buoyancy so that the robot is controlled in 3-D (Guo et al, 2003). Maximum propulsive force about 4 μN is obtained at low frequencies while a forward speed of 5.5 mm/sec is reported at driving frequency of about 1 Hz with 2.5 V.

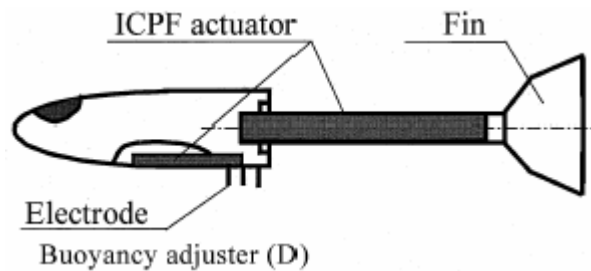


Figure 2.12: Structure of the ICPF microrobot (Guo et al., 1997).

2.6.2 IPMC actuated beating fins are used in a millimeter scale swimming microrobot (Laurent and Piat, 2001). With limited operating frequency at 2 Hz, 10

% deformation can be obtained for 2 V. In order to obtain more undulatory motion for increased efficiency, polyethylene film ($20 \times 10 \times 0.01$ mm) is chosen due to its flexible characteristics. Two 12×2 mm IPMC strips which are excited with 1 Hz sinusoidal 2 V are attached to the fins. Overall size of the robot is $50 \times 10 \times 10$ mm. It only weighs 0.69 g since control and power supply is not onboard. The reported maximum mean speed of robot is 1.8 mm/sec.

2.6.3 Biomimetic Soft Robot using IPMC imitates undulatory swimming by controlling more number of composite surfaces along the body (Nakabo et al., 2004). Using more composite sections increase the complexity while it enables the design resemble to the anguiform type swimming mode more. The developed robot is able to swim backwards freely as well as its forward motion by finding the optimal voltage, phase and frequency. An eel-like motion is realized by a phase-shifted sinusoidal input with maximum voltages of 2 V to each segment of the patterned IPMC. 18 mm segments form the whole artificial muscle as shown in Figure 2.13. In the experiments, maximum speed of 0.9 mm/sec is achieved at 2 V and at a frequency of 8 Hz with phase shift of 60° . Increasing or decreasing the driving frequency results in decrease in the speed of the test-bed.

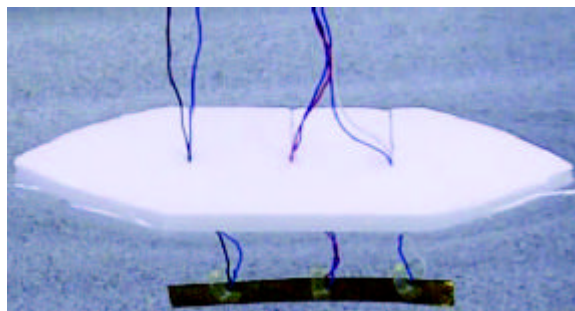


Figure 2.13: Segmented artificial muscle with float (Nakabo et al., 2004)

2.6.4 Polymeric Artificial Muscles – IEEMC (Ion-Exchange Membrane Metal Composites) are the propulsion fin of a boat like structure (Mojarrad and Shahinpoor, 1997). 12×8 cm buoyant styrofoam boat is built to house the driving circuitry and fin. Fin is actually the membrane that is cut in a strip (5×0.7 cm) to resemble fish-like caudal fin for propulsion. Driving circuitry generates ±2 V AC at 50 Hz. The speed of robot is measured as 1.87 cm/sec for the oscillating fin frequency of 5 Hz. Another aquatic vehicle as test-bed utilized by IEEMC has an overall length of 58 cm and 35 cm span (Mojarrad, 2000). Although the robot has not been constructed, the experiments are carried out by a static bench-test setup to characterize thrust capabilities and evaluate efficient input driving signals to the actuator fin. 0.8 gr thrust is obtained by driving the fins (5×4cm) at 3 Hz and 10 $V_{\text{peak_to_peak}}$ sinusoidal signal.

In ionic polymer actuators (IPA), performance relies on the material property of the ion exchange membrane. From the experiments of four robots linearity in between voltage-tip displacement and oscillation frequency-speed are found. However, range of operating frequency of IPA is limited between 0.1 to 5 Hz which should be improved for successful control on speed and steering. In order to increase the speed, oscillation frequency of the tail should be increased in IPA. A rigid or floating component is required for the robots in order to house control and power source. Nevertheless, because the actuator can not be integrated to the hull of robot, non-moving part demolishes the undulation. In addition to the narrow range of operating frequency of these actuators, unavoidable effect of the rigid part reduces the applicability of these actuators to mini swimming robots.

2.7 Piezoelectrically Actuated SRFL

Piezoelectric ceramics are utilized in SRFL with different displacement amplification mechanisms.

2.7.1 MMR (Micro Mobile Robot), with piezoelectric actuation utilizes stroke amplifying compliant mechanism in order to enhance the effect of the resonance condition and increase the strain rate of the piezoelectric actuator (piezoactuator) (Fukuda et al., 1994 and 1995). A pair of legs is stretched out of the body to each side as pectoral fins of fish which ease the steering. Each leg and the fin attached at tip is the end of the magnification mechanism driven by piezoactuators ($2 \times 3 \times 8$ mm). As shown in Figure 2.14, each element in the mechanism rotates around a miniature hinge and the displacement of piezoelectric ceramic stack (piezostack) is magnified at the end of fin. Piezostacks are driven near to the resonance peaks (~ 170 Hz and ~ 400 Hz) where forward mean velocity of 30 mm/sec is obtained. Separately controlled piezoactuators and legs allow the machine to be steered in 2-D successfully.

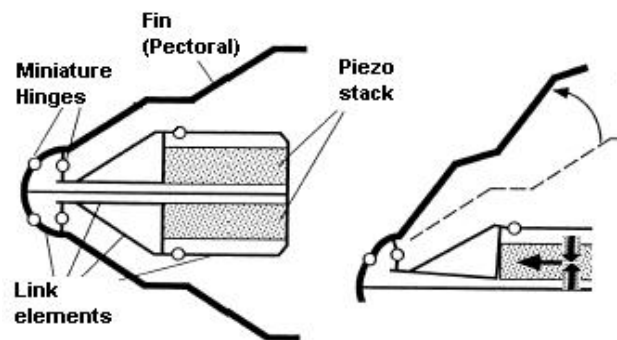


Figure 2.14: Magnification mechanism in MMR (Fukuda et al., 1994)

Compliant mechanism of this type sacrifices output force for increased stroke. Therefore, output deflection at fins is degraded when the system is loaded. Reduced deflection couples with the added inertia and finally result in low amplitude fin deflection and low velocities even the control and power are not onboard.

2.7.2 MSV (Miniature Swimming Vehicle) relies on oscillating foil propulsion activated by high deflection bending piezoelectric actuators (Borgen et al., 2003, Washington, 2004). Unlike to the study presented in 2.7.1, the need for a distinct motion amplifying mechanism is eliminated by employing THin-layer composite UNimorph ferroelectric DrivER and sensor (THUNDER) moving the caudal fin of the swimming vehicle. Except the power source, the hull of the vehicle houses all electronics as shown in Figure 2.15.

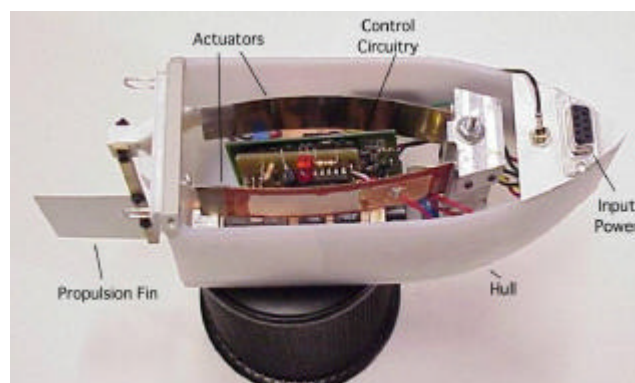


Figure 2.15: Prototype of the miniature swimming vehicle (Washington, 2004)

Actuators (THUNDER TH7R) consist of $95 \times 25.4 \times 0.254$ mm cantilevered steel strip to which a 0.25 mm piezoceramic layer (PZT-5A) is bonded using heat-activated adhesive. Large bending deflections of THUNDER compared to the conventional PZT actuators are because of the pre-strain condition imposed on the actuator during manufacture phase, stated as in (FACE, 2004).

Four-bar mechanism shown in Figure 2.16 is driven by two THUNDER actuators with phase differences in order to translate the motion of the actuators into the oscillating motion of the flexible caudal fin. In order to maximize fin displacement, actuators are driven at their resonance ($1^{\text{st}} = 30$ Hz, $2^{\text{nd}} = 160$ Hz) and at their maximum voltage input. Actuators driven under $600 V_{\text{peak_to_peak}}$ sinusoidal signal at their second resonance frequency (160 Hz) result in a mean

vehicle speed of 0.25 m/sec with 75×40 mm fin head. Steering of the vehicle is achieved by applying a DC to one of the actuators while keeping to drive the other with AC. The design at that stage permits the vehicle to travel on the water only due to the dependency on tethers for powering. Optimizations on the hull and fin design is required for achieving more successful fish-like swimming while optimizations on the actuators are not allowed due to the patent protections. About \$ 100 unit cost of THUNDER actuators is another disadvantage of the design (FACE, 2004).

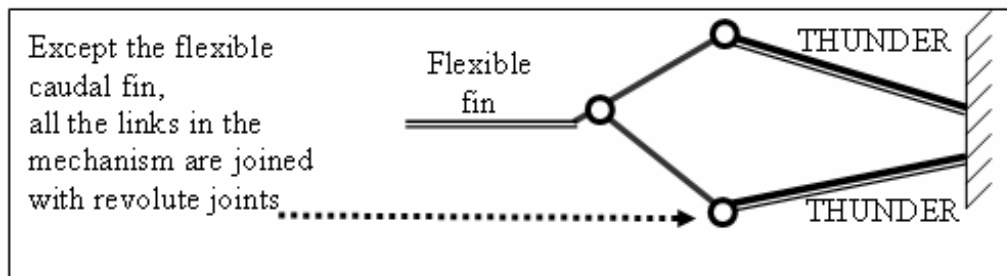


Figure 2.16: Four-Bar mechanism of miniature swimming vehicle.

CHAPTER 3

PRELIMINARY DESIGN

Preliminary design of swimming robot comprises identification of the specification of design, and constraints on the defined specifications. Mechanism and type of actuator is determined according to the comparative study of alternative actuation mechanisms for mini SRFL.

3.1 Design Specification

A robot having the specifications given below is aimed in this study:

- Fish-like swimming
- Small scale (miniaturization)
- Wide tail-beat frequency and amplitude range

While there are other design criteria including weight, cost *etc.* they are all secondary importance and the design will proceed with primary specifications and design constraints.

3.1.1 Fish-like swimming

Fish-swimming is not the optimal but it is highly efficient way of underwater propulsion and has numerous advantages over the conventional screw type propellers as it was discussed in Chapter 1.

Among the swimming modes which don't have strict boundaries, ostraciform type motion is the simplest of all due to the decreased degree of freedom. The more the undulatory motion in fish-swimming, the more control joints (degree-of-freedom) and links are required. More the number of the links, better the mechanism's maneuverability and redundancy, but harder the control and construction of the robot. With its still body and one-joint controlled flapping rigid fin characteristics, ostraciform type swimming will be imitated in the robot. Simplicity in swimming mode which minimizes the need of handling the complicated hydrodynamics and control of flexible surfaces, serves for the main scope of this thesis. Reducing the number of control joints degrades the accuracy of the model but enhances the understanding of actuators. A simple sketch for an ostraciform model is given in Figure 3.1. Model is composed of two rigid links that rotate around AA' (joint O).

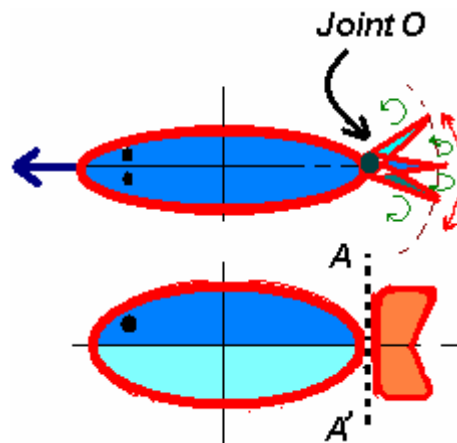


Figure 3.1: Mechanical model of ostraciform type swimming

3.1.2 Small scale (miniaturization)

Worldwide growing interest on the concept and possible applications of small scaled (miniature, micro and nanoscale) robots is also valid for SRFL. In order to extend the range of application of current robots while decreasing the cost, we attempted to build a *mini-scale* SRFL.

Trimmer and Jebens (1989) classify a system as micro if it is in centimeter or smaller while Dariot et al. (1992) classify few cubic centimeter robots as miniature and few cubic micrometer robots as microrobot. Most recent classification is made considering the volume of robots: A micro-robot has a volume around 10^{-6}m^3 while a mini-robot has volume around 10^{-3}m^3 which is equivalent to a cube with 10cm edges (Caprari, 2003). Depending on the available resources, facilities and technological advancement in Turkey, emphasis will be given to a mini-scale SRFL. The largest dimension of the robot will be limited to 10 cm in this study.

3.1.3 Broad range for tail-beat frequency and amplitude

The dependency of swimming speed with tail-beat frequency and amplitude of tail beat are known beginning for a long time (Lighthill, 1960). Whether the motion is undulatory or oscillatory, fish modulate the tail-beat frequency as well as the tail-beat amplitude, in order to control its speed and direction (Colgate and Lynch, 2004), (Moyle and Ceche, 2004).

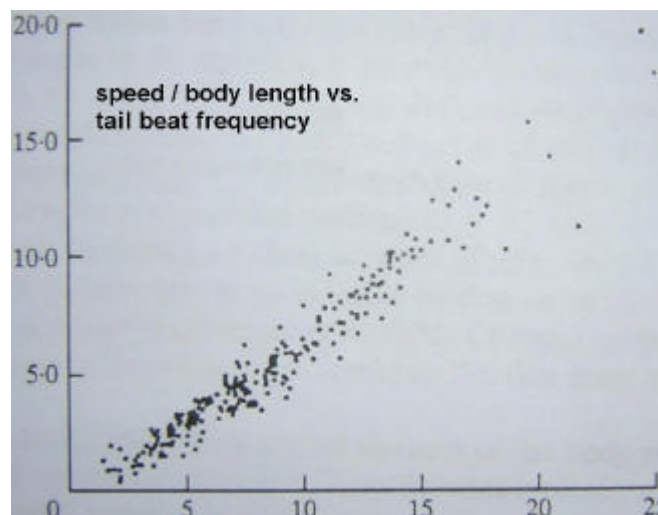


Figure 3.2: Relationship between swimming velocity and frequency of caudal undulations (tail-beats) for dace (*Leuciscus leuciscus*)

Plot of non-dimensional swimming speed against the caudal undulations (tail-beats) for dace (*Leuciscus leuciscus*) according to the study of Bainbridge (1958) is given in Figure 3.2 which is adopted from (Moyle and Cache, 2004). Although the plot in Figure 3.2 is given for a specific kind, tendency of increasing the speed of swaying for higher velocities is common for all fish.

Webb (1992) proposed a model of the mechanical thrust power for a BCF at an average speed U as given in (3.1)

$$P_T = \frac{B^2 \cdot \mathbf{r} \cdot f^2 \cdot A^2 \cdot \mathbf{p}^3}{8} \cdot U \cdot \left(1 - \frac{U}{V}\right) \cdot \left(\frac{(2\cos\mathbf{q} - 1)V + U}{2V \cos\mathbf{q}}\right) \quad (3.1)$$

where B is the trailing edge span, \mathbf{q} is the angle of trailing edge to the lateral plane of motion, \mathbf{r} is the density of the water, V is the velocity of the propulsive wave, f and A are the frequency and amplitude of caudal fin oscillations respectively. The power from fish to water is related with frequency and amplitude of tail-beat in second order. Increasing frequency or amplitude of tail-beat result in higher power output of the fish. In mobile robotic applications, speed linearly varies with the scale related to power and energy (Webb, 1992, Caprari et al, 2002).

Although the heaving motion and angle of attack of tail are important parameters in swimming, controlling swimming speed in robots mostly relies on amplitude but especially on frequency modulation of the tail-fin (Sfakiotakis et al, 1999, Colgate and Lynch, 2004).

It is reported that swimming speed of BRF that is given in section 2.1.4, increases with the oscillating frequency (Yu et al., 2003). Hirata (2000) states the linear relation of oscillating tail frequency with the forward swimming of NMRI Fish Robot, in section 2.1.5. In section 2.6, frequency dependent forward velocities of swimming robots that are utilizing various ionic polymer actuators are given. Frequency dependent forward velocities of piezoelectrically actuated small scale swimming robots are presented in section 2.7. Table 3.1 summarizes available dimensional and locomotion characteristics of the reported experiments of the BCF type swimming robots.

Table 3.1: Locomotion and dimensional characteristics of swimming robots

Section	Swimming mode	Speed mm/s	Body length (BL) mm	Speed BL/s	Actuator	Osc. (Hz)
2.1.1	Thunniform		1200		DC Servo	
2.1.2	Labriform	50	2000	0.025	DC Servo	0.5
2.1.3	Caran. / Pect.	600	500	1.2	DC Servo	
2.1.4	Carangiform	320	400	0.8	DC Servo	2
2.1.6	Carangiform	420	600	0.7	DC Servo	3
2.1.6	Carangiform	200	343	0.6	DC Servo	2.3
2.1.6	Carangiform	400	350	1.15	DC Servo	10
2.1.7	Carangiform	250	600	0.42	DC Servo	1
2.1.7	Carangiform	500	1200	0.42	DC Servo	1
2.1.8	Caran. / Pect.	150	1600	0.1	DC Servo	0.7
2.1.9	Anguilliform	600	800	0.75	DC Servo	2
2.1.9	Carangiform	2000	1210	1.65	DC	
2.2.1	Thunniform	1250	2400	0.52	Hydraulic	1
2.3.1	Ostraciform	120	747	0.16	Stirling	3
2.4.1	Anguilliform				SMA	4
2.4.2	Rajiform		460		SMA	1.29
2.5.1	Ostraciform	40	120	0.33	Muscle	3.1
2.6.1	Subcarangiform	5.5	45	0.12	ICPF	1
2.6.2	Carangiform	1.8	50	0.036	IPMC	1
2.6.3	Anguilliform	0.9	54	0.0167	IPMC	8
2.6.4	Carangiform	18.7	120	0.16	IEMMC	5
2.7.1	Labriform	30	35	0.9	PZT	400
2.7.2	Ostraciform	250	300	0.83	PZT	160

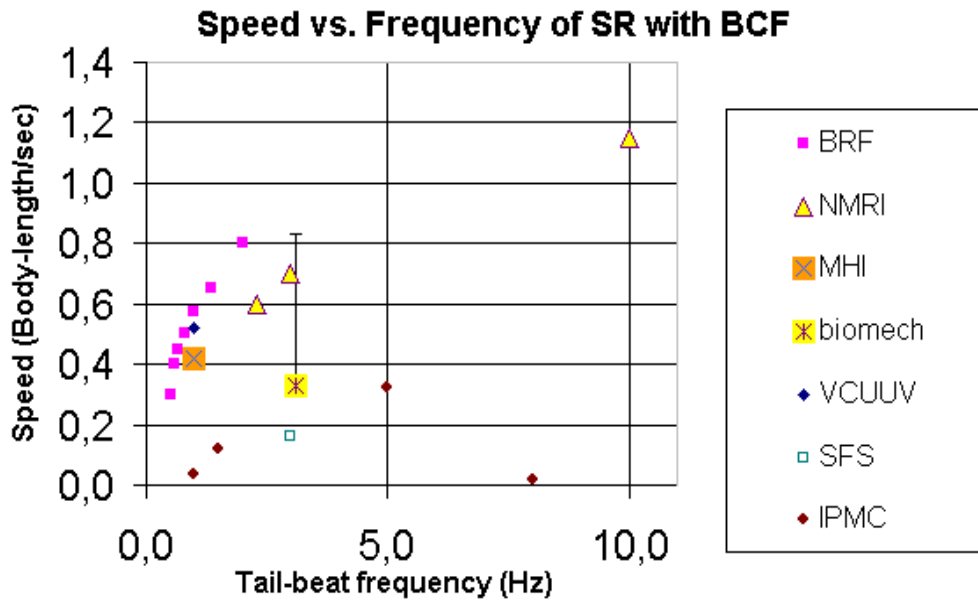


Figure 3.3: Forward swimming speed vs. tail-beat oscillation frequency characteristics of some swimming robots utilizing BCF type locomotion.

Frequency modulation is preferred more than amplitude modulation in swimming speed and direction control because the oscillation frequency is observable while it's difficult to measure the deflection at tail end.

Figure 3.3 is plotted in order to show the trend of increasing oscillation frequency for higher speeds even for different actuation mechanisms. In the figure, BRF, NMRI, MHI, biomech, VCUUV, SFS and IPMC denotes the reported data of the robots presented in the sections 2.1.4, 2.1.5, 2.1.6, 2.5.1, 2.2.1, 2.3.1 and 2.6. Frequency modulation in SRFL is achieved by applying various driving signal schemes to actuators which is limited to the operating frequency of the actuators and response characteristics of the actuation materials. Broad operating frequency range of actuation materials and mechanisms will determine the performance of the swimming robot.

For efficient swimming, the range of non-dimensional Strouhal (St) number is given in equation (3.2) where f , d and U are oscillation frequency, width of the

wake formed by the tail (related with the amplitude) and forward velocity of the robot in still water respectively (Triantafyllou et al., 1993).

$$0.25 \leq \left\{ St = \frac{f \cdot d}{U} \right\} \leq 0.35 \quad (3.2)$$

Moving the tail at such a frequency and amplitude for controlling the robot and at the same time maintaining the range given in equation (3.2) requires broad range for tail-beat frequency and amplitude.

3.2 Design Constraint

Constraints on the design of mini swimming robot originates mainly from the dimensional requirements and cost of the components used in robot. Storage (power supply) and utilization (actuators) of energy should be performed in a smaller volume than in conventional means (in macro domain). Since power is an amalgam of tail beat frequency and amplitude which should be properly arranged, proper motion of actuators should also be supplied for limited space and power. In addition, as the robot and in the same way the components are miniaturized, availability and machinability of the components reduces but the cost of these parts increases. Therefore, primary constraint on the design originates from the downscaling of swimming robot.

3.2.1 Constraint on Dimension and Weight

Since the final goal of this study is an underwater SRFL, the robot should be designed to free float. For floating freely, mini swimming robot having a volume of 1000 cm³ can only weight 1000 gr where a micro robot is limited up to only 1 gr in a water-like media.

Previous work on the biomimicry suggests some limitations on the shape of SRFL due to the hydrodynamics. Most robots are designed to be three dimensional ellipsoids in streamlined-shape. Following the design parameters and dimension ratios of a robot fish, given by Tzeranis et al. (2001); $L_1=2L_2$, $3L_1=10L_3$, $L_1\cong 3H_1$ where L_1 is the body length (rigid part), H_1 is the approximate length of the tail, L_2 is the body-height and L_3 is the thickness of the robot. According to the parameters given above, a mini robot-fish, which has a total body length smaller than 10 cm, can only occupy a volume about 60 cm^3 .

Therefore, the weight of the design has an upper limit of 60 gr in a water-like environment while the volume is kept at about 60 cm^3 . Reduced volume of the robot also limits the weight of the robot and so the components.

3.2.2 Effects of Downscaling on the SRFL

Downscaling effects will be considered via subsystems in order to point out the most critical subsystems and to clearly define the design constraint. Discussion and understanding of the scaling effects and its consequences on the SRFL will be performed through the scaling law approach on the subsystems which gives the tendency of a physical dimension when scaling down. Non-dimensional numbers that combine important system parameters are useful when dealing with systems that have similar configurations but different dimensions. L will be used as the characteristic length of reference.

In Table 3.2, basic mechanical quantities are summarized according to the scaling law, based on the studies (Caprari, 2003, Trimmer and Jebens, 1989, Waldron and Hubert, 2000, Fearing, 1998, Thielicke and Obermeier, 2000).

Table 3.2: Summary of the effect of scaling on some physical quantities

Unit	Symbol	Scaling
Volume	Q	$\sim L^3$
mass	m	$\sim L^3$
Mass related force	F	$\sim L^3$
Friction force	F_m	$\sim L^3$
Energy losses due to friction	E_m	$\sim L^4$
Drag force	F_{drag}	$\sim L^2 \sim L^3$
Viscous force		$\sim L^2$
Structural stiffness	c	$\sim L$
Stress related to the mass	s	$\sim L$
Structural eigenfrequencies	f	$\sim L^{-1}$
Electrostatic forces	F_{ES}	$\sim L^2$
Electromagnetic force	F_{EM}	$\sim L^4$
Pressure related forces (hydraulics, SMA)		$\sim L^2$
Biological forces		$\sim L^2$
Piezoelectric forces		$\sim L^2$
Electromagnetic motor torque for constant efficiency	T_{EMM}	$\sim L^5$
EMM torque for similar motor temperatures	T_{EMM}	$\sim L^{3.5}$
EMM mechanical power	P	$\sim L^4$
Rotational speed of EMM	Ω	$\sim L^{-1}$
Electrochemical energy		$\sim L^3$
Energy sources*		$\sim L^3$
Solar panel		$\sim L^2$

* Energy source types included in this category are: silver-oxide, alkaline, lithium, zinc-air, rechargeable NiCd, NiMH, Li-ion, rechargeable lithium-polymer, fuel cell, gasoline, spring, rubber band. Housing of the sources is ignored while applying the scaling law to this category.

Main subsystems of a swimming robot can be listed as:

- 1) Hull
- 2) Sensors and Communication Devices
- 3) Control Unit and Driving Circuitry
- 4) Energy Source
- 5) Actuator

Scaling down the mechanical systems leads to stiff ($\sim L$) and to comparatively lightweight structures with high shock resistance. As the complex hydrodynamics effects are ignored in this study for simplicity in modeling the system, surface quality and other properties affecting the flow patterns around the robot can be ignored for material selection and design of hull. **Hull** of the robot should only maintain to be lightweight, stiff, easy to machine and assemble, water-proof and low-cost.

Recent advances in silicon microfabrication and microdevice technology lead to availability of, low-cost, high performance sensors, communication devices and processors. Since environmental interaction and high level intelligence of the robot are not the primary goals, even the effect of scaling down on power consumption of **sensors** and **control unit** are ignored in this study.

Comparable space is required for the **driving circuitry** made up of on-the-shelf elements considering the cost.

On board energy source or the capability to harvest required energy is essential for mobile robots and therefore SFRL. Harvesting energy is not a reliable method since the source may not be available every time. Although the batteries are the energy sources with highest power densities included in table, densities are far away from the order of a few watt-hours per grams even the housings are not taken

into account. Scaling down the energy sources does not favour them to drag and friction related energy losses either. Although the high density power supply is one of the most vital requirements in SRFL, utilization of the limited power with actuation methods having high power and torque density will be focused more in this study, rather than supplying it. Actuator is the subsystem which demands the energy most. Thus, small and lightweight on-the-shelf batteries will be used instead of developing a novel means of supplying high density power.

Scaling effects on basic actuation forces are compared in Table 3.2 and it was showed that while electrostatic, hydraulics, pneumatics, piezoelectric and biological forces scale well into the micro domain, electromagnetic forces do not. Apart from the scalability, each type of actuator has advantages and disadvantages and none is perfectly suitable for different specifications. Therefore, actuators will be investigated according to not only 1) scalability but also 2) availability, 3) input power requirement and auxiliary supply, 4) power/torque density, 5) strain and 6) operating frequency which are the important parameters for our case.

In most of the SRFL studies, electromagnetic motors are preferred as the actuators because of their superior characteristics at macro domain as given in section 2.1. Although miniature robot studies are mostly focused on unconventional/smart materials since electromagnetic motors (EMM) suffer at small scale, a more detailed emphasis will be given to the unavailability of EMM.

3.2.2.1 Unavailability of EMM for small scale SRFL

Poor torque density, (3.3), of small electromagnetic motors are due to the order of fourth dimensional dependence on electromagnetic force ($\sim L^4$). Thus, they can obtain high power density (3.4) only at high speed. Brackets in (3.3) and (3.4) are used to show dimensional dependence.

$$\text{Torque density} = \left\langle \frac{N \cdot m}{kg} \right\rangle \quad (3.3)$$

$$\text{Power density} = \left\langle \frac{N \cdot m}{kg} \cdot \frac{1}{s} \right\rangle \quad (3.4)$$

Since speed is inversely proportional to motor diameter ($\sim L^{-1}$), scaling down can result in very high motor speeds requiring large speed reduction ratios to match motor speed to robotic joint speed.

The need for efficient transmission to obtain large forces and torques at low speeds from inherently high speed force actuators is a very significant problem for small robots (Fearing, 1998). Speed reducers, mostly the gears, introduce friction, backlash, torque ripple and noise. Unavoidably increased inertia due to gearing slows the system response. In addition, the practical reduction ratio achievable any type of speed reducer is limited thus high ratios mean multiple and more complex reduction stages. Waldron and Hubert (2000) point out that, complexity includes mechanically bulky, heavy and inefficient designs since efficiency degrades exponentially with the number of reduction stages. In order to avoid the disadvantages of gearing, direct-drive is a solution for industrial robots but not for mobile robotics (Pratt and Williamson).

Nevertheless, today electromagnetic motors dominate centimeter-size domain while electrostatic actuators are superior in micro-domain due to the advances in MEMS technology. Between the scales of centimeter and micrometer, there is a demand for powerful actuators.

3.2.2.2 Comparison of the available actuation mechanisms for small scale SRFL

The actuator comparison criteria for mini robot swimming include the following:

- 1) Scalability
- 2) Availability

3) Input power requirement and auxiliary supply

4) Power and Torque density

5) Strain

6) Operating frequency

Actuators rely on the use of different types of transducing materials and of energy conversion principles. Advances on these material properties can largely affect the performance and characteristics of actuators which make the comparison of these actuators difficult. Cost of the actuators also heavily depends on the cost and availability of these materials. The actuators which are not commercialized yet and are not utilized in a previous SRFL research will be ignored due to funding constraint of this study.

Therefore, comparison of the performance and characteristics of these actuators will be limited to the ones and materials used in SRFL studies available in literature.

Muscle actuators are successfully applied to SRFL as presented in section 2.5.1. Since real muscles work in an intensively controlled intravascular media, these conditions should be maintained which limits the use in mobile applications.

Although **pneumatic**, **hydraulic** and **stirling-engine** type actuators have good strain, power and torque densities they suffer from the agility. Low response rate of these actuators are due to the inertial operating fluidic effects. The requirement of auxiliary pressure supply unit and noisy operations are the other drawbacks of these actuators.

SMA is an attractive material for the SRFL studies because of the exceptional strain rate with excellent torque density and high power density. However, as seen in Table 2.1, SMA cannot be utilized successfully for small scale SRFL. Unavailability of these materials for small scale SRFL is not due to the scalability effect as in EMM but because of the temperature dependent low operating

bandwidth. Especially for small scale SRFL, the constraint of having a broad range of operating bandwidth becomes significant. Therefore, SMA cannot sustain one of the specifications of robot.

Ionic polymer artificial muscles have excellent power and torque density characteristics (Madden et al., 2004). However, they require an aqueous operating medium and high operating power which make them unsuitable for mobile applications. Although the successful propulsion characteristics and experiments of these polymeric materials are presented in section 2.6, application of these materials for a SRFL with on-board power has not been demonstrated yet due to these drawbacks.

Piezoceramic Actuators (PZT) also have excellent power density with fastest response time. Broad operating frequency and high density power utilization can be achieved via a successful mechanism design. They can generate large forces in compact sizes due to the high pressure densities thus; they can be miniaturized further without being effected from scalability. As seen in Table 2.1 and Table 3.1, PZT are suitable for miniaturization since considerable swimming speeds have been achieved with PZT actuators mounted on small scaled structures. Two successful applications of these materials are presented in sections 2.7.1 and 2.7.2.

The main drawbacks of these materials are the low strain rate and the need of special driving circuitry. Low deflection rates of these materials are amplified through different mechanisms. The necessity of complex circuitry can be avoided by a simplified mechanical design.

3.3 Piezoceramics

As a result of the specifications and constraints on the design, piezoceramics are selected for the actuator material.

Piezoelectricity is a phenomenon that occurs in a certain class of naturally occurring crystalline materials such as quartz, Rochelle salt and tourmaline (Jaffe et al., 1971). Because of the crystalline structure, piezoelectric materials change their geometry when an electric field is applied to them, and conversely they produce an electric charge for mechanical pressure. However, these materials exhibit such a small amount of this very useful behavior in contrast to other materials have been created with improved piezoelectric properties. Piezoelectric ceramics made of polycrystalline ferroelectric materials such as BaTiO₃ and Lead Zirconate Titanate (PZT) have been manufactured with improved piezoelectric properties. Typical free strains induced in traditional piezoelectric materials (PZT) are reported to be on the order of 0.1 % to 0.2 % while new relaxor ferroelectric single crystals (PZN-PT and PMN-PT) can develop strains in excess of 1 % having 5 times as much strain energy density in conventional piezoceramics. Merits and demerits of these actuators are summarized in Table 3.3.

Table 3.3: Merits and Demerits of piezoelectric actuation

Merits	Demerits
<ul style="list-style-type: none"> ○ Excellent operating bandwidth, ○ Can generate large forces in compact size, ○ High power density. 	<ul style="list-style-type: none"> ● Minute deflection, ● The need of high-voltage high frequency driving circuitry.

For most piezoelectric actuators, the focus of research has been on an attempt to amplify the deflection of the material to cast it into a useful form. Piezoelectric actuation architectures can generally be placed into one of three defining categories based on the amplification scheme (Niezrecki et al., 2001)

- 1) Externally leveraged
- 2) Internally leveraged
- 3) Frequency leveraged

3.3.1 Externally leveraged

Externally leveraged actuators include an external mechanical component for their magnified actuating ability. Lever Arm Actuators is a type of externally leveraged piezoelectric actuator. It's the simplest way to increase the displacement of an actuator. The mechanism increases the displacement, decreasing the output force. A typical way to fabricate such a device is to use a flexure-hinged mechanism and a piezostack. As given in section 1.7.1, micro mobile robot utilizes a displacement magnification mechanism by lever arm hinged to piezostack (Fukuda et al., 1994).

3.3.2 Internally leveraged

This type of amplification scheme generates amplified strokes through the internal structure without the use of an external mechanical component. THUNDER actuator as shown in Figure 3.4, is the most known and highly commercialized example of pre-stressed curved beam piezoelectric bender actuators which have multi layers of piezoelectric material and flexible strips (FACE, 2004). The indirect effect of the internal piezoelectric strain of the layers which are poled and activated such that layers on opposite sides of the neutral axis have opposing strain causes the entire bender to flex. As given in section 1.7.2, miniature swimming vehicle utilizes THUNDER actuators in a four-bar mechanism for the sway motion of caudal fin. Rather than externally amplifying the strain, using internally leveraged actuators make the mini robot advantageous over the robot presented in 1.7.1. Moreover, main drawback of the mini swimming robot with THUNDER actuators is the high cost of the actuators.



Figure 3.4: Thunder[®] Model TH 8-R

3.3.3 Frequency leveraged

These actuators rely on an alternating control signal to generate motion. Inchworm and ultrasonic (linear and rotary) motors are the two general subclass of this group (Niezrecki et al., 2001).

The strain output from actuators is increased by using the frequency performance of the piezoelectric material to rapidly move the actuator in series of small steps. This type of actuator architecture trades the speed of the piezoelectric material for infinite stroke. Nevertheless, this scheme suffers from limited force generation due to frictional effects.

In the next chapter, the design of frequency leveraged piezoelectric actuator requiring a simple driving circuitry will be presented for imitating ostraciform type swimming mode in a small-scale hull design. The design of actuator and driving circuitry depends on the previous studies on a novel type ultrasonic motor in Atilim University, Turkey (Tunçdemir and Koç, 2004).

CHAPTER 4

ACTUATOR DESIGN

“Actuators are devices which perform the final output stage of mechatronic behavior” (Anthony Lucas-Smith, 1999). Actuators convert energy from the power supply to various mechatronic means. In our design, electrical energy stored in batteries will be transformed into oscillating tail motion for locomotion (ostraciform type swimming) as the final output stage of mechatronic behavior.

Frequency-leveraged piezoelectric actuators which are usually called as ultrasonic motors (UM) generate motion from electrical energy. In order to obtain swaying fin motion, mechanical displacement produced by UM should be converted to a useful form by means of a mechanism. UM requires special driving circuitry providing high voltage and high frequency signals, as stated in Chapter 3. Type of the signals required for driving different number of stacks or layers of ceramics in phase determines the complexity of the driving circuitry. Structure of UM depends on the way of utilization and placement of piezoelectric ceramics. Thus, mechatronic integration should be carefully stated for a simple mechatronic structure. Basic components of locomotion system and energy flow between the main components are shown in Figure 4.1.

4.1 Design of Piezoelectric Ultrasonic Motor: Resonator Design

Basic construction of the piezoelectric ultrasonic motor is depicted in Figure 4.2 adapting from (Flyer, 1995), (Uchino and Koc, 1999). Two-stage energy conversion mechanism is the fundamental of operating principle of the motor.

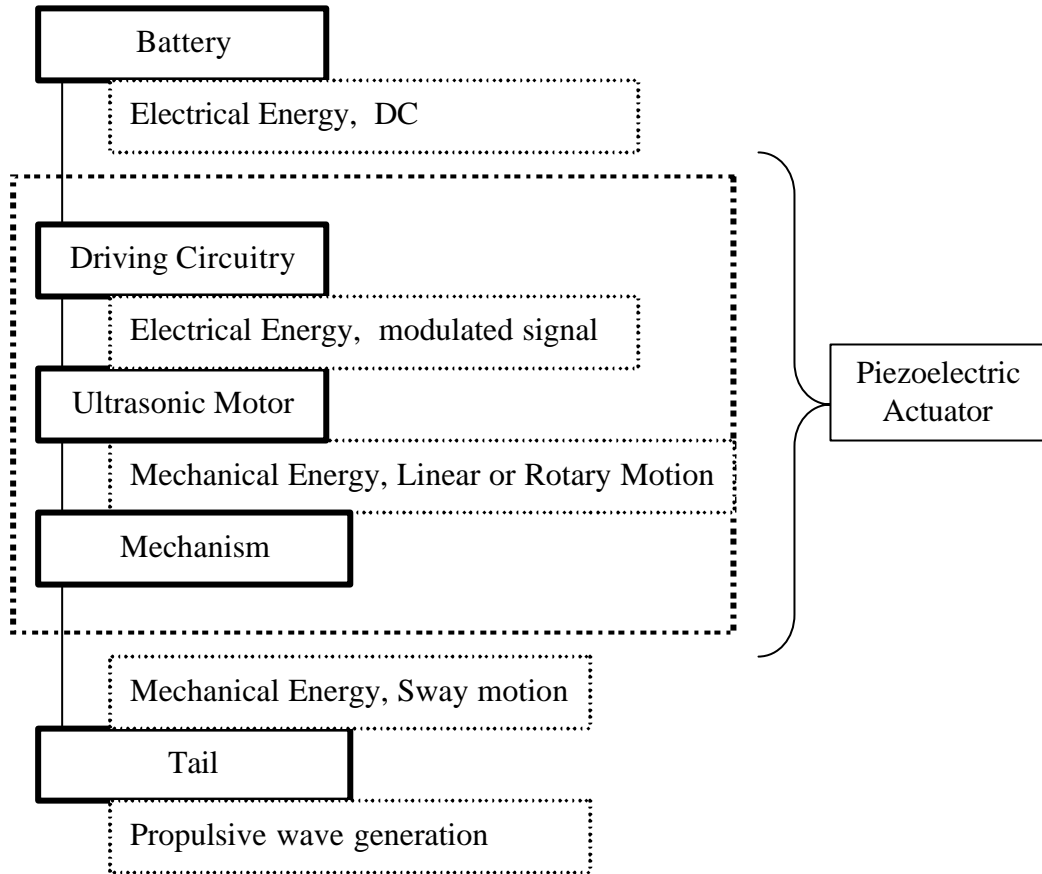


Figure 4.1: Energy flow schema of locomotion

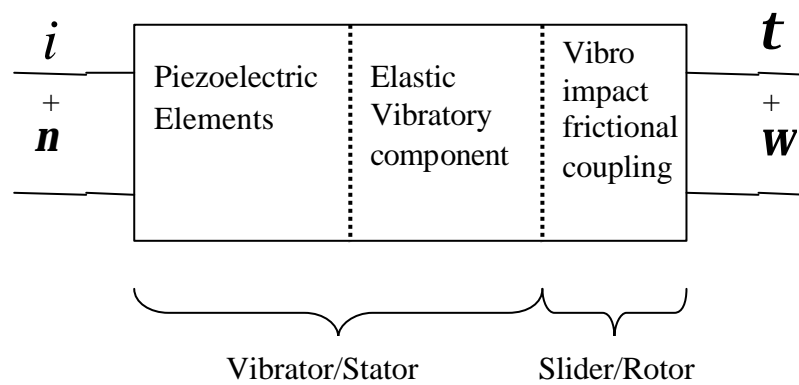


Figure 4.2: Basic construction of piezoelectric ultrasonic motor

In the first stage, electrical energy is converted to strain energy in form of high frequency mechanical oscillations through piezoelectric elements. Time changing electrical fields induce vibratory motion on piezoelectric elements. Depending on the physical embodiment of the device and the formation of vibratory elements as well as the form of the excitation of piezoelectric elements, high frequency mechanical oscillations take different form of deformations. Orthogonal (longitudinal, torsional or flexural) vibrational modes are induced in the structure to give standing or traveling wave type. Whatever the type of deformation, common output motion obtained on the surface is an elliptical trajectory. Through an intermittent or continuous *vibro-impact* frictional coupling of the elliptical trajectory and rotor, piezoelectric strain is transferred to a linear or rotary motion. Second stage energy conversion in an UM is the rectification of high frequency surface motion into lower frequency, macroscopic, unidirectional rotary or linear motion of a rotor or a slider.

According to the final mechanical output of the second stage of energy conversion, UM are also classified as *rotary* or *linear*. A linear motor will require an additional mechanism or the couple of the same motor for generating oscillating tail motion. Nevertheless, angular control of rotary UM will enable to control the degree of rotation of the tail without using an additional mechanism. Therefore, rotary type UM will be considered with its gearless direct drive characteristics.

Construction of standing wave type ultrasonic motor is simpler than a traveling wave type (Morita, 2003). Due to the reduced number of drive circuit components, standing-wave type motors are also electrically simple (Uchino, 2002). Rod, cylinder and rectangular plates are the most popular shapes of active piezoelectric elements used in the stator structure. Rod type structures will be focused on as they are simple to model and easy to fix the frame. Holding the vibrator from the nodal point without disturbing the vibration is crucial. Vibrator is connected to mainframe through nodal points which are the motionless points in a vibrating structure. Even if the stator is held at its nodal, the fixed point can move to a non-nodal point due to the vibration. As the motors are miniaturized, very small changes in the position of the holder would easily result in diminishing the

performance of the motors or even causing them not to operate. Mobile robots are designed to operate in various environments and are usually subject to various disturbances which can diminish the performance of UM. Holding the vibrator is therefore an important problem of UMs.

In addition to the requirement of high voltage high frequency signals in a small volume, intolerability to mechanical instability of UM is another major problem of UM's that negatively affects the utilization of these actuators in mini/micro mobile robots.

A new piezoelectric motor applicable for mini mobile applications is designed in order to benefit from the piezoelectric actuation in swimming mini robot. The key idea of the design of the motor is reducing the mechatronic complexity of it (Tunçdemir and Koç, 2004). Emphasis in UM design is given to design a stator simple enough to be miniaturized without a holding problem. Driving circuitry is also simple enough to be miniaturized and to be controlled easily.

A brief overview of the motor including the comparison with the available ones in the literature having the similar operating principles is presented in the next section.

4.1.1 Overview

In the proposed motor, a stator structure is devised using a *sandwiched type* cantilever beam. Geometry of the *bimorph* structure is tailored for matching the frequencies. First longitudinal (L1) and third bending (B3) resonance modes are coupled on a cantilever resulting in an elliptic motion at the tip. For *multimode excitation* (L1 and B3) at *resonance*, piezoceramic is induced at a certain frequency. Rotary motion of the rotor is obtained via the *intermittent frictional contact* with the tip of the vibrator. Since the vibrator is fixed from one end, it does not require any nodal point correction but only the rotor or slider requires adjustment with a suitable pre-stress. Piezoceramics are poled and fixed to the

resonator in such a way that *bidirectional* rotation can be obtained by switching the *single power source* from one ceramic to other.

Several examples of rotary UM utilizing the piezoceramics by means of the similar method on a rod or beam type vibrator as mentioned above are investigated previously. Despite the high torque characteristics, traveling wave type motors are omitted due to their structural complexity which makes them difficult to manufacture and to miniaturize further.

An UM making use of resonant longitudinal vibrations of a rod-shaped metallic resonator is proposed in (Fleischer et al., 1989a). An AC voltage with the frequency of the longitudinal mode of the mechanical resonator is applied to piezoceramics. Resonator is diagonally arranged to a drum-like structure which is utilized as the rotor. Harmonic motion of the stator is transmitted to a continuous motion on rotor by intermittent frictional contact.

Another UM, developed by Fleischer et al. utilizes the vibration of two orthogonal modes (Fleischer et al., 1989b). Two sets of piezoceramics are induced to generate longitudinal and flexural vibrations separately. Mechanical oscillations of a metallic resonator induced by piezoceramics sets result in *Lissajous Figures* at the tip of the resonator. Whatever the frequency and phase shift of the signals fed to the ceramics, an elliptical trajectory is obtained. The driving action originates from the intermittent friction contact between the resonator end with elliptical trajectory and the rotor.

Based on the design given in (Fleischer et al., 1989a, b), two distinct piezoelectric actuators are used in order to obtain bidirectional motion (Kurosawa et al., 1991). First actuator, named as torsional vibrator, is composed of four PZT disks and generates traveling-wave type vibrations that drive the motor. Second actuator with multilayered stacks arranges the frictional force between the stator and rotor. Rotor is pre-stressed to the stator via second actuator and a spring.

A rotary motor which is used as a card forwarding mechanism as shown in Figure 4.3 is developed using double-mode vibrators (Tomikawa et al., 1992).

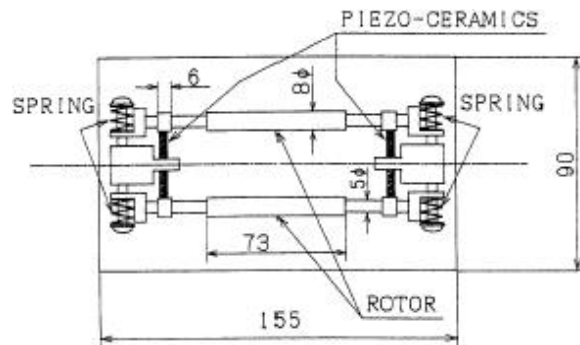


Figure 4.3: Structure of the motor given in (Tomikawa, 1992)

Dimensions of piezoceramics are set to a specific height to length ratio to degenerate first longitudinal and second bending modes independently. Surface of each piezoceramics at each side are divided into two regions to be induced separately for generating two modes independently. Number of components for the structure makes design complex for miniaturization and manufacture.

As an improvement to the design in (Tomikawa,1992), Aoyagi and Tomikawa (1993) obtain double mode coupling by the additional asymmetry of a piezoelectric vibrator regardless of the height to length ratio of ceramic. Mode coupling on a diagonally symmetric piezoelectric ceramic plate with a specific length to thickness ratio is reported in (Aoyagi and Tomikawa, 1996). Although it is not necessary to divide the ceramic to obtain two modes and bidirectional rotation is possible with one channel driving, structures are fixed at their nodal points leading to assembly problems. Structure of UM is shown in Figure 4.4.

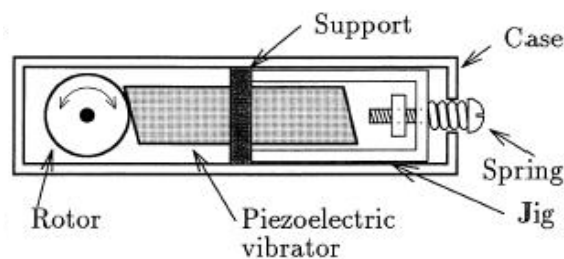


Figure 4.4: Structure of the motor given in (Aoyagi and Tomikawa 1993)

Tomikawa et al. (1995) proposed a rod type UM utilizing two second flexural vibration modes with a phase difference of 90° . The stator is a hollow cylinder in which a pair of piezoelectric ceramics is inserted in its axial direction at the center portion of cylinder between two steel blocks. As seen in the Figure 4.5, rotors are pressed to the end faces of the stators and the whole motor is fixed at the center which lead holding problem.

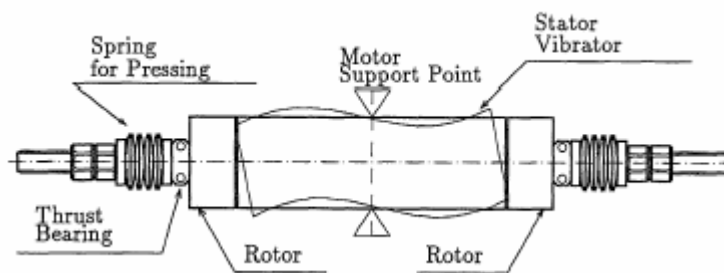


Figure 4.5: Rod type UM (Tomikawa et al.,1995)

Utilizing the driving principle of rotating stepwise mechanism presented in (Bexell and Johansson, 1996), a 4 mm diameter piezoelectric motor is manufactured which is shown in Figure 4.6 (Bexel and Johansson, 1998). Neither 4 mm motor, nor the improved design by Tong et al. (2003) are UM since the operations depend on quasi-static positioning of ceramics rather than vibrating at resonance.

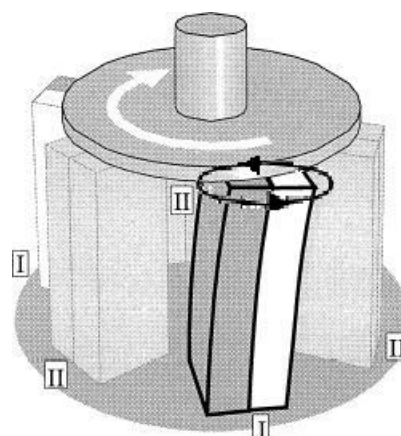


Figure 4.6: The motor based on serial bending arms. (Bexel and Johansson,1998)

With appropriate phase shift drive, elements which are fixed on a silicone substrate rotate the upper part. Tong et al (2003) state the manufacturing errors as the reason for the low efficiency. Manufacturing errors are due to mechanical complexity of whole structure and difficult manufacturing and assembly process of the arms.

It was observed that the simpler the structure, the easier the miniaturization and commercialization of these motors. In order to build UM thin enough for micro applications, ceramic plate vibrator will be utilized inducing longitudinal and bending vibrations (Tomikawa et al., 1992). Longitudinal and bending modes are two orthogonal modes that can generate an elliptical trajectory.

Despite the similarity of structures and operating principles, the developed motor can be distinguished from its predecessors by its simple structure. Simplicity in electrical driving is due to the simple stator design that also avoids the holding problem.

Design parameters of stator are determined according to the dimensional requirements for frequency matching on a cantilever structure.

4.1.2 Symmetric PZT/Elastic Cantilever Laminate

In the three layered symmetric piezoelectric/elastic laminate structure which is shown in Figure 4.7, a metal layer is sandwiched in between two uniformly poled piezoelectric layers.

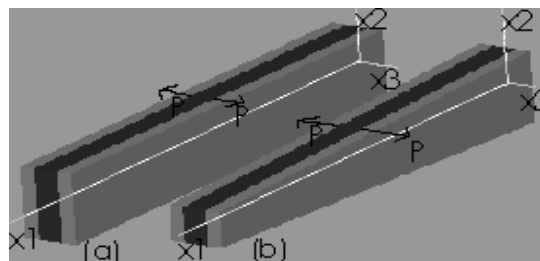


Figure 4.7: Two different geometries proposed for the cantilever beam

Two methods proposed for frequency-matching on a bimorph which is used for amplifying the vibration, are:

- 1) Setting the beam at a specific length to thickness ratio for constant width which is shown on the left side of Figure 4.7,
- 2) Tapering the width of the beam for constant length and thickness as shown on the right of Figure 4.7. Moreover, two methods can be used together (Tunçdemir and Koç, 2004).

In order to match the resonant frequencies of longitudinal and bending vibrations, equation of motion of the structure in Figure 4.8 is derived assuming the two vibrations are free. Therefore, equation of motion and resonance frequency calculations will be performed neglecting the effects of one mode to other. Other assumptions made throughout the vibration analysis of the bimorph structure can be listed as follows.

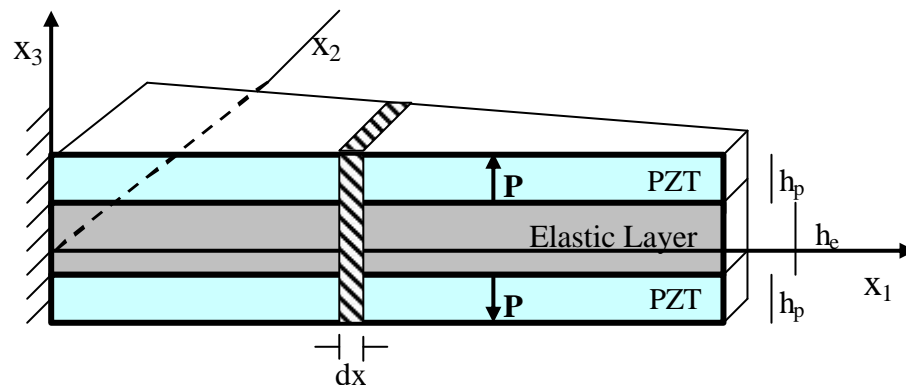


Figure 4.8: Three layered symmetric piezoelectric/elastic laminate (cantilever bimorph) structure with coordinate axes and basic dimensioning

Thin Euler Bernoulli Beam assumption is made and layers of the bimorph are assumed perfectly attached to each other without generating internal stress along the contact.

Thickness of the structure (h) remains constant after deformation.

$h_b = 2h_p + h_e$ is the thickness of bimorph where h_p is the thickness of a piezoelectric layer and h_e is the thickness of elastic layer, ignoring the thickness of adhesive layer.

4.1.3 Derivation of Equation of Motion for Longitudinal Vibration of Bimorph Beam

Equation of motion for longitudinal vibration of the bimorph with no external forcing is derived by using Newton's Law of Motion.

The forces along x_1 , acting on the cross sections of a small element of the bar are given by F_1 and $F_1 + dF_1$ and shown in Figure 4.8. Strain along x_1 -direction (S_1) is given in equation (4.1):

$$S_1 = \frac{du_1(x_1, t)}{dx_1} \quad (4.1)$$

Since the strain is independent from time, displacement along x_1 direction can be simply expressed as u_1 .

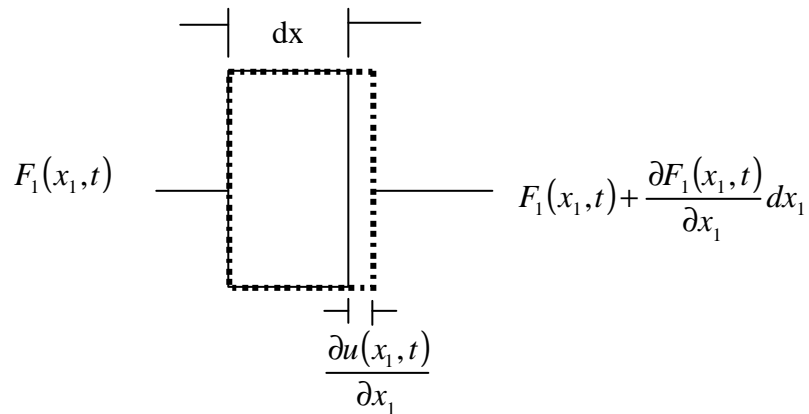


Figure 4.9: Forces on a small section of a beam in longitudinal vibration

Because of the directional rigidity of piezoelectric layers, force ($F_1(x_1, t)$) is not linear with normal stress. Force along x_1 direction with no time dependency is expressed as:

$$F_1(x_1) = 2 \int_0^{\frac{h_e+h_p}{2}} T_1 \cdot b(x_1) \cdot dx_3 \quad (4.2)$$

where T_1 is the normal stress along direction x_1 and $b(x_1)$ is the width of the beam along x_2 as a function of x_1 .

T_1 is obtained following the formulation and asymptotic method presented by Rogacheva et al (Rogechava, 1998) and using the constitutive equations supplied for piezoelectric materials (IEEE, 1988).

Constitutive equations for piezoelectric material are presented in (4.3) and (4.4).

$$S_1 = s_{11}^E \cdot T_1 + d_{31} \cdot E_3 \quad (4.3)$$

$$D_3 = d_{31} \cdot T_1 + \mathbf{e}_{33}^T \cdot E_3 \quad (4.4)$$

$$S_1 = \frac{T_1}{E} \quad (4.5)$$

Strain for elastic material is simply given by equation (4.5) in terms of stress and Young's modulus of elasticity. Moreover, for piezoelectric materials, strain along x_1 direction (S_1), is function of elastic compliance (s_{11}^E , along x_1 direction at constant electric field), stress (T_1 , along x_1), piezoelectric constant (d_{31} , induced along x_3 to deform along x_1 direction) and electric field (E_3 , through x_3 direction).

Electrical displacement in direction x_3 , (D_3), is given in equation (4.4) where \mathbf{e}_{33}^T denotes dielectric constant for piezoelectric material at constant stress. For quasistatic electric condition, there is no electrical displacement in direction x_3 :

$$\frac{dD_3}{dx_3} = 0 \quad (4.6)$$

Electrical potential between surfaces of each ceramic is V while elastic layer is grounded. Therefore, there is no electric field (E_3) applied in elastic layer while the electric field in elastic layer is given as:

$$E_3 = \frac{V}{h_p} \quad (4.7)$$

For longitudinal vibration, normal stress along x_1 is expressed as a function of x_3 using (4.5) and (4.7) in (4.3),

$$T_1 = \left\{ \begin{array}{ll} ES_1, & \text{for } 0 < x_3 < \frac{h_e}{2} \\ \frac{S_1}{s_{11}^E} + \frac{2d_{31}V}{s_{11}^E h_p}, & \text{for } \frac{h_e}{2} < x_3 < h_p \end{array} \right\} \quad (4.8)$$

Then, using (4.1) and (4.2), force along x_1 direction can be expressed as:

$$F_1 = b(x_1) \cdot \left(\left(\frac{2h_p}{s_{11}^E} + Eh_e \right) \cdot \frac{du}{dx_1} + \frac{4d_{31}}{s_{11}^E} V \right) \quad (4.9)$$

The summation of forces which are shown in Figure 4.9, in the x_1 direction gives the equation of motion

$$(F_1 + dF_1) - F_1 = b(x_1) m_1 dx_1 \frac{\partial^2 u}{\partial t^2} \quad (4.10)$$

Right side of the equation (4.10) is the inertial force due to the applied force where m_1 is the weighted mass of the beam per cross section which is given in (4.11):

$$m_1 = h_e \mathbf{r}_e + 2h_p \mathbf{r}_p \quad (4.11)$$

$$dF_1 = \left(\frac{\partial F_1}{\partial x_1} \right) dx_1 \quad (4.12)$$

By using (4.12), equation (4.10) reduces to (4.13).

$$\frac{\partial F_1}{\partial x_1} = b(x)m_1 dx_1 \frac{\partial^2 u}{\partial t^2} \quad (4.13)$$

Using the force equation (4.9) in (4.13) gives the equation of motion (4.14) for longitudinal vibration of the structure shown in Figure 4.8.

$$\frac{\partial}{\partial x_1} \left(b(x_1) \cdot \left(\frac{2h_p}{s_{11}^E} + Eh_e \right) \cdot \frac{\partial u_1}{\partial x_1} \right) = b(x)m_1 dx_1 \frac{\partial^2 u}{\partial t^2} \quad (4.14)$$

Defining a weighted stiffness constant (K_1) in (4.15) for longitudinal vibration, equation (4.14) reduces to (4.16)

$$K_1 = \frac{2h_p}{s_{11}^E} + Eh_e \quad (4.15)$$

$$K_1 \frac{\partial}{\partial x_1} \left(b(x_1) \cdot \frac{\partial u_1}{\partial x_1} \right) = b(x)m_1 dx_1 \frac{\partial^2 u}{\partial t^2} \quad (4.16)$$

4.1.4 Derivation of Equation of Motion for Lateral Vibration of Bimorph Beam

Moments and forces implied on a small section of a bimorph are shown in Figure 4.10, where $w(x_l, t)$ is the displacement.

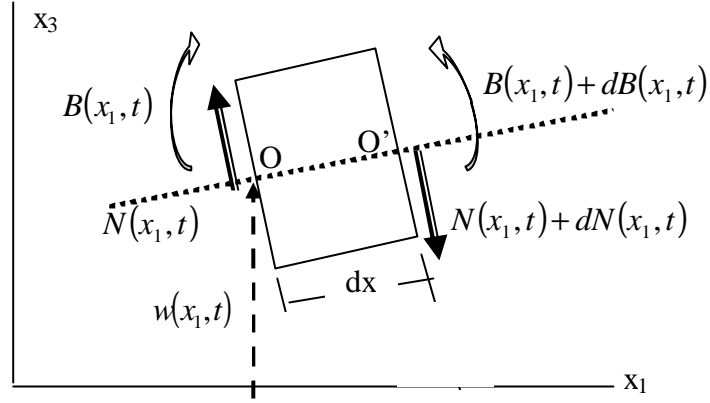


Figure 4.10: Forces on a small section of a beam in transverse deflection

In the Figure 4.10, $B(x_1, t)$ is bending moment and $N(x_1, t)$ is shear force per unit length. Inertia force acting on the element is given as in (4.17)

$$b(x_1)m_1dx \frac{\partial^2 w(x_1, t)}{\partial t^2} \quad (4.17).$$

The force equation of motion is;

$$-(N(x_1, t) + dN(x_1, t)) + N(x_1, t) = b(x_1)m_1dx \frac{\partial^2 w(x_1, t)}{\partial t^2} \quad (4.18)$$

The moment equation of motion about the axis passing through the points (O-O') in Figure 4.10 is given in (4.19)

$$(B(x_1, t) + dB(x_1, t)) - (N(x_1, t) + dN(x_1, t))dx - B(x_1, t) = 0 \quad (4.19)$$

$$dN = \left(\frac{\partial N}{\partial x_1} \right) dx_1, \quad dB = \left(\frac{\partial B}{\partial x_1} \right) dx_1 \quad (4.20)$$

$$N(x_1, t) = \left(\frac{\partial B}{\partial x_1} \right) \quad (4.21)$$

By using (4.20) and (4.21) in (4.18) and (4.19), and disregarding terms involving second powers, (4.22) is obtained which is the partial differential equation of motion of bending vibration.

$$-\frac{\partial^2 B(x_1, t)}{\partial x_1^2} = b(x_1) m_1 dx \frac{\partial^2 w(x_1, t)}{\partial t^2} \quad (4.22)$$

Bending moment in the bimorph structure is expressed as in equation (4.23):

$$B = \int_{-\left(\frac{h_e+h_p}{2}\right)}^{\left(\frac{h_e+h_p}{2}\right)} b(x_1) x_3 T_{1_Bending} dx_3 \quad (4.23)$$

For bending vibration, normal stress in direction x_1 takes the form given in (4.24), adopted from (Rogacheva, 1998).

$$T_1 = \begin{cases} E \frac{d^2 w}{dx_1^2} x_3, & \text{for } 0 < x_3 < \frac{h_e}{2} \\ -\frac{d_{31}^2 (h_e + h_p)}{2s_{11}^E (s_{11}^E \mathbf{e}_{33}^T - d_{31}^2)} \frac{d^2 w}{dx_1^2} + \frac{2d_{31} V}{s_{11}^E h_p}, & \text{for } \frac{h_e}{2} < x_3 < h_p \end{cases} \quad (4.24)$$

Using (4.24) in (4.23) and taking the integral along the thickness gives (4.25)

$$B = b(x_1) \left(\left(\frac{2}{3s_{11}^E} \left[\left(\frac{h_e}{2} + h_p \right)^3 - \frac{h_e^3}{8} + \frac{h_p^3 d_{31}^2}{4(s_{11}^E \mathbf{e}_{33}^T - d_{31}^2)} \right] + \frac{E h_e^3}{12} \right) \frac{d^2 w}{dx_1^2} + \frac{2d_{31} (h_e + h_p) V}{s_{11}^E} \right) \quad (4.25)$$

With (4.25), equation of motion given in (4.22) reduces to (4.26) where the weighted stiffness term for bending vibration (K_2) and is defined in (4.27)

$$-\frac{\partial^2}{\partial x_1^2} \left(K_2 \cdot \frac{\partial^2}{\partial x_1^2} \left(b(x_1) \frac{\partial^2 w(x_1, t)}{\partial x_1^2} \right) \right) = b(x_1) m_1 dx \frac{\partial^2 w(x_1, t)}{\partial t^2} \quad (4.26)$$

$$K_2 = \frac{2}{3s_{11}^E} \left[\left(\frac{h_e}{2} + h_p \right)^3 - \frac{h_e^3}{8} + \frac{h_p^3 d_{31}^2}{4(s_{11}^E e_{33}^T - d_{31}^2)} \right] + \frac{Eh_e^3}{12} \quad (4.27)$$

4.1.5 Frequency Matching on a Uniform Cantilever Bimorph

For uniform beam ($b(x_I) = b$), equation (4.14) reduces to an eigenvalue problem (EVP) defined in (4.28) which must be satisfied throughout the domain $0 \leq x_I \leq L$ and the homogeneous boundary conditions (BC) at $x_I=0$ and $x_I=L$ given in (4.29) and (4.30).

$$-K_1 \frac{d^2}{dx_1^2} U(x_1) = \mathbf{w}^2 m_1 U(x_1) \quad (4.28)$$

$$U_1(x_1) \Big|_{x_1=0} = 0 \quad (4.29)$$

$$\frac{dU_1(x_1)}{dx_1} \Big|_{x_1=L} = 0 \quad (4.30)$$

EVP given in (4.28-30) has a general solution set given in (4.31).

$$U(x_1) = C_1 \sin(\mathbf{b}x_1) + C_2 \cos(\mathbf{b}x_1) \quad (4.31)$$

$$\mathbf{b} = \mathbf{w} \sqrt{\frac{m_1}{K_1}} \quad (4.32)$$

Using BC's (4.29) and (4.30), frequency equation is obtained as in (4.33) which gives the solution set (4.34) of natural frequencies of longitudinal vibration for r^{th} mode (\mathbf{w}_{r-L}).

$$\cos(\mathbf{b}L) = 0 \quad (4.33)$$

$$\mathbf{w}_{r-L} = (2r-1) \frac{\mathbf{p}}{2L} \sqrt{\frac{K_1}{m_1}} \quad (4.34)$$

Equation of motion for bending vibration given in (4.26) reduces to EVP defined in (4.35) for constant width unimorph bimorph structure ($b(x) = b$).

$$K_2 \frac{d^4 Y(x_1)}{dx_1^4} = \mathbf{w}^2 m_1 dx Y(x_1) \quad (4.35)$$

4 boundary conditions that $Y(x_1)$ should satisfy at base (4.36, 37) and at tip (4.38, 39) of the cantilever are given

$$Y(x_1) \Big|_{x_1=0} = 0 \quad (4.36)$$

$$\frac{dY(x_1)}{dx_1} \Big|_{x_1=0} = 0 \quad (4.37)$$

$$\frac{d^2 Y(x_1)}{dx_1^2} \Big|_{x_1=L} = 0 \quad (4.38)$$

$$\frac{d^3 Y(x_1)}{dx_1^3} \Big|_{x_1=L} = 0 \quad (4.39)$$

The general solution of the EVP defined in (4.35-39), is given as in (4.40)

$$Y(x_1) = C_1 \sin(\mathbf{b}x_1) + C_2 \cos(\mathbf{b}x_1) + C_3 \sinh(\mathbf{b}x_1) + C_4 \cosh(\mathbf{b}x_1) \quad (4.40)$$

$$\mathbf{b} = \sqrt[4]{\frac{\mathbf{w}^2 m_1}{K_2}} \quad (4.41)$$

Using (4.41) frequency equation is obtained which is given in (4.42), by imposing the boundary conditions (4.36-39) to (4.40).

$$\cos(\mathbf{b}L) \cdot \cosh(\mathbf{b}L) = -1 \quad (4.42)$$

Numerical solution of (4.42) yields infinitely many solutions for $\mathbf{b}_r L$, where r indicates the number of vibrational mode. For the first three modes, $\mathbf{b}_r L$ takes values of $\mathbf{b}_1 L = 1.875$, $\mathbf{b}_2 L = 4.694$, $\mathbf{b}_3 L = 7.855$. The resonance frequency expression of r^{th} bending mode (\mathbf{w}_{r_B}) of a beam in free vibration is given as in (4.43).

$$\mathbf{w}_{r_B} = (\mathbf{b}_r L)^2 \sqrt{\frac{K_2}{L^4 m_1}} \quad (4.43)$$

Available ceramics are 10 mm in length, 0.3 mm in thickness and 1.5 mm in width. For the available ceramics and elastic layer defined in Table 4.1, natural frequencies of the first three bending and longitudinal modes are plotted against the thickness of the elastic layer in Figure 4.11. Because of the constraints on available ceramics, only L1 and B3 match at a reasonable metal layer thickness which is shown in Figure 4.11.

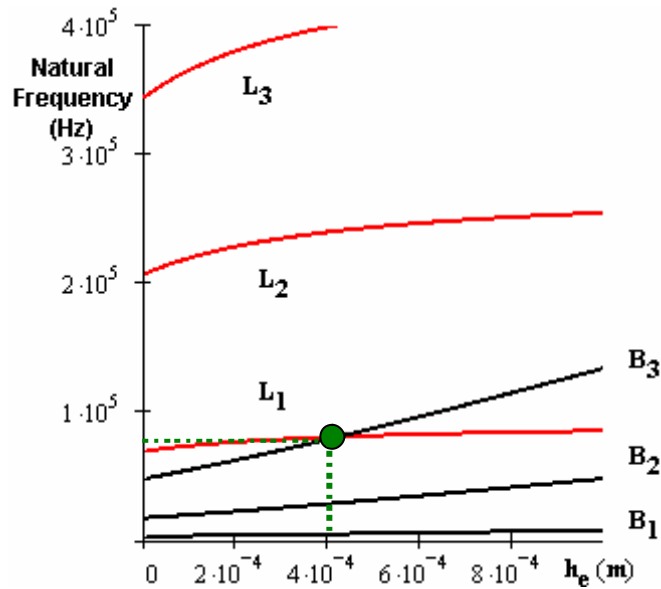


Figure 4.11: Natural frequencies of longitudinal and bending modes vs. elastic layer thickness

Table 4.1: The material properties of metal and piezoelectric layers.

	Phosphor-Bronze Cu94/Sn6	APC 841
ρ	8.9 g cm ⁻³	7.6 g cm ⁻³
E	90 GPa	-
s_{11}^E	-	17.3 10 ⁻¹²
k_{31}	-	0.33

4.1.6 Frequency Matching on a Tapered Cantilever Bimorph

Second method, proposed for frequency matching includes tailoring the beam by tapering the tip or base while setting length and thickness to a specific ratio. For a linearly tapered beam as shown in Figure 4.7, width of the beam (in x_2 direction) is not constant but is expressed as in (4.44)

$$b(x_1) = b_0 \left(1 - \left(1 - \frac{b_1}{b_0} \right) \frac{x_1}{L} \right) \quad (4.44)$$

Because of the non-uniform mass and stiffness distribution which are due to the variable cross section area, of the tapered beam eigenvalue problems defined for longitudinal (L) and bending (B) vibrations cannot be solved.

Although it is impossible to obtain exact solutions for the natural frequencies as well as the vibrational mode shapes, it is sufficient to know only the lowest frequencies in order to figure out the vibrational characteristics of the system. As followed from the formulation given in (Meirowitch, 1968), Rayleigh-Ritz method is utilized to obtain *Galerkin Equations* for approximating the solution by an n degree of freedom system where n is a finite number depending on the accuracy.

Rayleigh-Ritz method assumes a solution in the form of a finite series, consisting of known functions multiplied by unknown constants. It consists of selecting a trial family of comparison function Ψ_i . Suitably chosen trial family of n-comparison functions, Ψ_i ($i=1, 2, 3 \dots n$), should satisfy boundary conditions of the problem and constructs a linear combination expressed in (4.45)

$$\Psi_n = \sum_{i=1}^n a_i \Psi_i \quad (4.45)$$

In equation (4.45), a_i denotes the unknown coefficients to be determined in order to obtain Ψ_n , which is the trial (comparison) function that will be used in Rayleigh's Quotient (4.46).

$$R(\Psi_n) = \frac{\int_D \Psi_n L[\Psi_n] dD}{\int_D \Psi_n M[\Psi_n] dD} \quad (4.46)$$

In (4.46), L and M are the linear differential operators obtained from the generalized formulation of the EVP (4.47) with satisfied boundary conditions:

$$L[\Psi_n] = I \cdot M[\Psi_n] \quad (4.47)$$

For our problem, $I = w^2$

Differential operators of the eigenvalue problems given for longitudinal (4.28-30) and bending (4.35-39) vibrations are expressed as follows:

$$L = -\frac{d}{dx} \left[K_1 b(x) \frac{d}{dx} \right] \quad (4.48)$$

$$L = -\frac{d^2}{dx^2} \left[K_2 b(x) \frac{d^2}{dx^2} \right] \quad (4.49)$$

Since K_1 and K_2 are constant over x_1 , (4.48) and (4.49) reduce to (4.50) and (4.51), respectively

$$L = -K_1 \frac{d}{dx} \left[b(x) \frac{d}{dx} \right] \quad (4.50)$$

$$L = -K_2 \frac{d^2}{dx^2} \left[b(x) \frac{d^2}{dx^2} \right] \quad (4.51)$$

$$M = b(x)m_1 \quad (4.52)$$

Linear differential equation for mass component (4.52) can be used in both modes while the stiffness component (4.50) is given for longitudinal and (4.51) is expressed for bending vibrations.

When the approximated solution set Ψ_n is identical to the eigenfunction of the system, Rayleigh's Quotient ($R(u)$), expressed by equation (4.46), takes the minimum which is the corresponding exact eigenvalue. In Rayleigh-Ritz Method, instead of guessing the best eigenfunction, a_i 's are found which give the Ψ_i that yield the best approximation.

$$R(\Psi_n) = \frac{\int_D \Psi_n L[\Psi_n] dD}{\int_D \Psi_n M[\Psi_n] dD} = \frac{N(\Psi_n)}{D(\Psi_n)} \quad (4.53)$$

In order to minimize $R(\Psi_n)$ whose minimum is exactly ω^2 , derivative of (4.53) with respect to a_r is equated to zero which finally yields (4.54).

$$\frac{\partial N(\Psi_n)}{\partial a_r} - \omega^2 \frac{\partial D(\Psi_n)}{\partial a_r} = 0 \quad (4.54)$$

Galerkin's Equation (4.55) is obtained by using (4.45) in (4.54):

$$\sum_{j=1}^n (k_{rj} - \omega^2 m_{rj}) a_j = 0 \quad (4.55)$$

Equation (4.55) represents an EVP for n-degree-of-freedom system

$$k_{ij} = \int_D \Psi_i L[\Psi_j] dD \quad (4.56)$$

$$m_{ij} = \int_D \Psi_i M[\Psi_j] dD \quad (4.57)$$

$k_{ij} = k_{ji}$ $m_{ij} = m_{ji}$ are symmetric since L and M are self-adjoint linear differential operators. EVP expression in discrete system can be given as in (4.58):

$$[k^*] \{a\} = \omega^2 [m^*] \{a\} \quad (4.58)$$

In (4.58), $[k^*]$ and $[m^*]$ denote stiffness and mass matrices while $\{a\}$ contains the constants which give the best ω_i 's.

For longitudinal vibration, elements of non-dimensional stiffness and mass matrices take the general form, given as in (4.59) and (4.60).

$$k_{ij} = -K_1 \cdot b_0 \int_0^1 V_i \left((b_r - 1)u \cdot V_i' + (1 + (b_r - 1)) \cdot V_j'' \right) du \quad (4.59)$$

$$m_{ij} = m_1 \cdot b_0 \int_0^1 V_i \cdot (1 + (b_r - 1)u) \cdot V_j du \quad (4.60)$$

where V is used instead of Ψ (for comparison functions) for longitudinal vibration and V' denotes the first order differentiation with respect to u while V'' denotes the second order differentiation. $b(x)$ is defined in non-dimensional form in (4.61).

$$u = \frac{x}{L} \quad 0 \leq u \leq 1 \quad (4.61)$$

$$b(u) = b_0(1 + (b_r - 1)u) \quad (4.62)$$

$$b_r = \frac{b_t}{b_0} \quad (4.63)$$

b_r is the ratio of the width at tip (b_t) and base (b_0).

For lateral vibration, mass matrix is in the same form as in (4.60) but with different comparison functions, W (used instead of ϕ for bending vibration), given in (4.64) and stiffness matrix takes the general form given in (4.65).

$$m_{ij} = m_1 \cdot b_o \int_0^1 W_i \cdot (1 + (b_r - 1)u) \cdot W_j du \quad (4.64)$$

$$k_{ij} = K_2 \cdot b_o \int_0^1 W_i \cdot \left((1 + (b_r - 1)u) \cdot W_j^{(4)} + 2(b_r - 1) \cdot W_j^{(3)} \right) du \quad (4.65)$$

$W^{(3)}, W^{(4)}$ denote the order of differentiation with respect to u .

Solution of (4.58) yields $\phi_n^{[r]}$ which is the estimated eigenfunction for the r^{th} mode.

$$\Psi_n^{[r]} = \sum_{i=1}^n a_i^{[r]} \Psi_i \quad (4.66)$$

4.1.6.1 Approximate solution for the first three natural frequencies of longitudinal vibration using 6 modes

As stated by Rao (2002), a large number of suitably chosen assumed functions leads to more accurate results although it involves more computational work. For the first three natural frequencies, 6 comparison functions are chosen.

Comparison functions for longitudinal vibration are chosen as:

$$V_r = \sin\left(\frac{(2r-1)\pi \cdot u}{2}\right) \quad r = 1, 2, \dots, 6 \quad (4.67)$$

V_r defined in (4.67) are linearly independent functions of the dimensionless coordinate u , given in (4.61), which satisfy all the boundary conditions. Solution of the EVP is approximated by the linear combination given in (4.68)

$$V_n = \sum_{i=1}^n a_i V_i \quad (4.68)$$

In order to solve EVP for estimated natural frequencies, 6x6 matrices $[m^*]$ and $[k^*]$ in (4.58) are constructed in MATLAB environment, by using (4.59) and (4.60). Solution of (4.58) in case of longitudinal vibration for different system parameters is summarized and necessary codes generated in MATLAB are presented in Appendix-A with a flowchart of solution algorithm. Since 6 nodes are utilized to construct the approximation method, first three modes can be well estimated. Although first three natural frequencies of the bimorph for longitudinal vibration can be obtained, L1 is returned as functions of L, h_p , h_b , s_{11}^E , k_{31} , q and mass density of each layer in the function named *piezotapered_L1B3_vs_btaper.m* whose code is presented in Appendix- A.

4.1.6.2 Approximate solution for the first three natural frequencies of bending vibration using 6 modes.

Solution of the EVP is approximated by the linear combination given in (4.69)

$$W_n = \sum_{i=1}^n a_i W_i \quad (4.69)$$

Comparison functions W_r are chosen similar to the general solution of bending vibration of a clamped-free beam (4.40), satisfying all the boundary conditions.

$$W_r = \sin(\mathbf{b}_r u) - \sinh(\mathbf{b}_r u) - \mathbf{a}_r (\cos(\mathbf{b}_r u) - \cosh(\mathbf{b}_r u)) \quad (4.70)$$

$$\mathbf{a}_r = \frac{\sin(\mathbf{b}_r) + \sinh(\mathbf{b}_r)}{\cos(\mathbf{b}_r) + \cosh(\mathbf{b}_r)} \quad (4.71)$$

where β_r takes specific values for r, from 1 to 6, which denotes the mode number. Values of β_r for the first six bending modes are given as; $\beta_1 = 1.875$; $\beta_2 = 4.694$; $\beta_3 = 7.855$; $\beta_4 = 10.996$; $\beta_5 = 14.137$; $\beta_6 = 17.278$;

In order to solve EVP for estimated natural frequencies, 6x6 matrices $[m^*]$ and $[k^*]$ in (4.58) are constructed in MATLAB environment, by using (4.64) and (4.65). Solution of (4.58) in case of lateral vibration for different system parameters is summarized and necessary codes are supplied in Appendix-B with a flowchart of solution algorithm. Since 6 nodes are utilized to construct the approximation method, first three modes can be well estimated. Integrals derived from (4.65) and (4.64), cannot be evaluated explicitly by using the Symbolic toolbox of MATLAB, in the domain of u . Therefore, frequency of bending vibrations is obtained utilizing a different method and functions than the one followed for L1. Numerical integration of the integrands (4.64) and (4.65) are required. Boole's Rule is utilized with 5 segments over 1000 data points.

Although first three natural frequencies of the bimorph for bending vibration can be obtained, only the B3 is returned as functions of L , h_p , h_e , s_{11}^E , k_{31} , b_t and mass density in the function named *t_plotLIB3.m* whose code is presented in Appendix-B.

Using the parameters given in Table 4.1 and for 10×0.3 mm ceramics in length and thickness, natural frequencies of the L1 and the B3 modes for different elastic layer thicknesses ($h_e = 0.4; 0.45; 0.5; 0.55; 0.6$ mm) versus the tapering ratio are plotted in Figure 4.12.

Because of the different characteristics of two modes around $b_0/b_1 = 1$, varying the width of a beam becomes crucial if the length and the thickness parameters should remain constant.

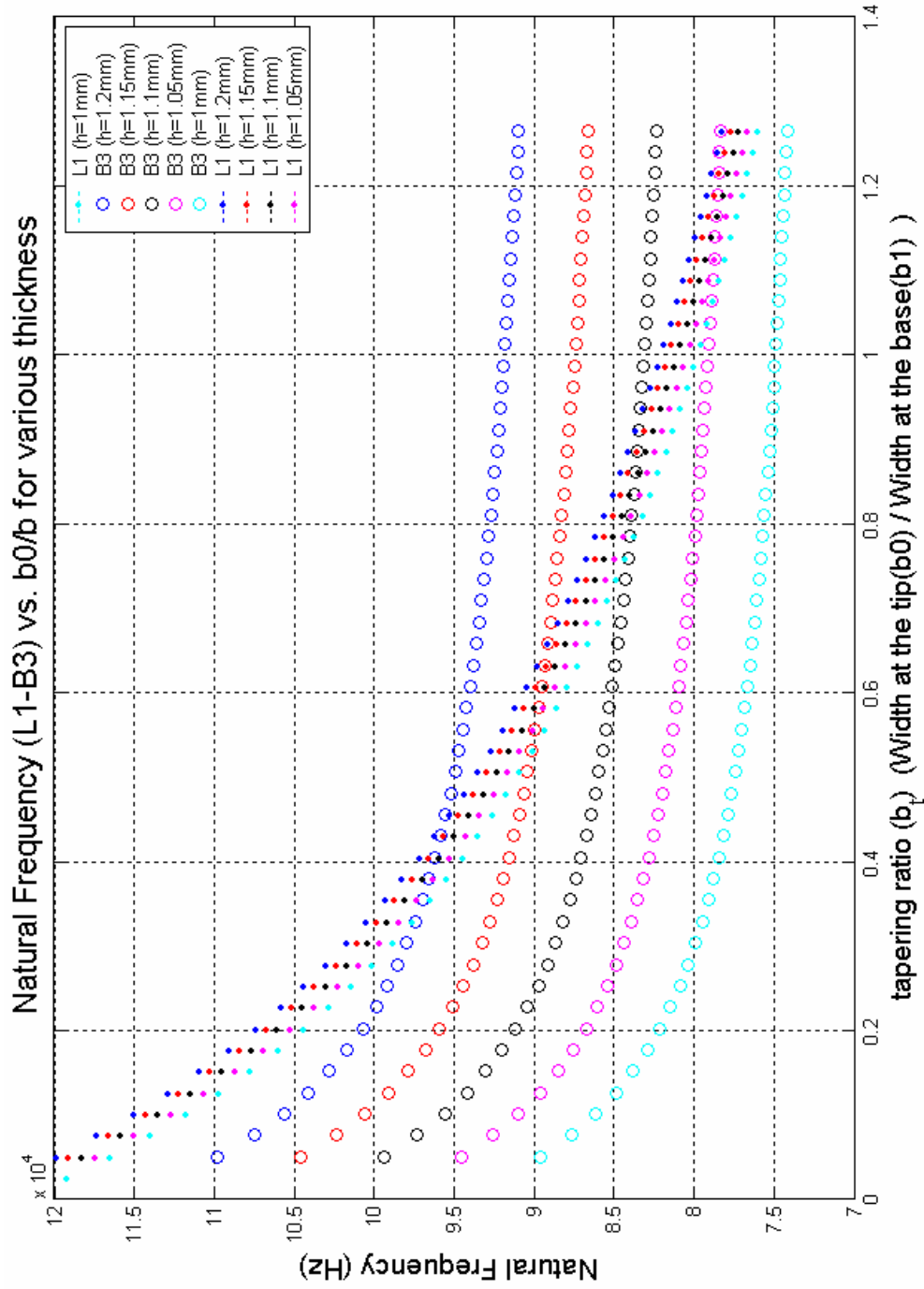


Figure 4.12: Natural Frequency (L1-B3) vs. the tapering ratio (b_0/b_1) for various thickness of resonator

4.1.7 Selection of the Bimorph Parameters for Constructing the Motor

In this work, most important constraint on the design of ultrasonic motor is the dimensions of the available ceramic. APC-841 ceramics with the given parameters in Table 4.1 are $10 \times 1.5 \times 0.3$ mm in length, width and thickness respectively. Therefore, from Figure 4.11, $L1$ and $B3$ match at near 70 kHz, on a cantilever bimorph of 10 mm in length and 1.5 mm in width if 0.3 mm thick piezoelectric ceramics are fixed onto a 0.45 mm thick elastic layer. For given parameters, $L1$ and $B3$ are the only available orthogonal matching frequencies on a cantilever structure.

In Figure 4.12, tapering the beam does not change the bending frequency much but cause longitudinal frequency to decrease as the end is thickened. Increasing the thickness of elastic layer (going up in Figure 4.12 and going right in Figure 4.11) does not affect natural frequencies of longitudinal vibrations but lateral vibrations.

During manufacturing many factors especially the adding of adhesive chemical between the layers detour the mechanical structure and change the frequency conditions. Because of the unavoidable occupied space of adhesive, slight increase in thickness results in a big rise of $B3$. In order to compensate the fact in the example case, beam can be tapered at end, causing a significant increase in $L1$ if rise of matching-frequency can be tolerated in design.

Because of the significant changes in frequencies, corresponding to a slight change in tapering ratio, second method (tapering the width) is strongly proposed for frequency tuning if appropriate machining and measuring utilities are available.

In this work, elastic layer thickness is specified for the given geometries. Dimensions for cantilever structure are tabulated in Table 4.2.

Table 4.2: Dimensions of the symmetric piezoelectric/elastic laminate cantilever structure

Component	Thickness	Length	Width
Phosphor Bronze	Various sizes from 0.4 to 0.8mm	10 mm	1.5 mm
APC 841	0.3 mm	10 mm	1.5 mm

With the given dimensional constraints, operating frequency of motor which is the matching frequency of L1 and B3 is theoretically found as 70 kHz.

4.2 Operating Principle of the Motor

Elliptical trajectory generation at the tip of the designed symmetric piezoelectric elastic laminate is the operating principle of the motor. Although the theoretical calculations result in mode coupling at the matching resonance frequency, the model constructed for bimorph structure includes assumptions which may cause deviations from the actual response. In order to realize and minimize the deviation, two empirical tests are implemented before and after the construction of motor.

First step possesses the visualization of the resulting motion and testifying the matching frequency condition of stator via ATILA (Magsoft, 2004) which is specialized finite element method software in piezoelectric actuation.

Second test includes the test of matching frequency by measurement of the voltage response of one piezoelectric ceramic layer to the mechanical vibrations on stator because of the excitation of other layer.

Resonant frequency of the laminate structure for L1 and B3 modes which are calculated with ATILA were close to the results given with Figure 4.11. Mode

coupling on the beam and the resultant motion due to coupling are also observed via ATILA. Elliptical trajectory of the tip of the beam as a resultant motion of mode coupling is presented with the circle in the center of Figure 4.13. In Figure 4.13, stator structure is excited by a single piezoelectric layer and one period of the motion is shown with ten equal intervals which were obtained separately by ATILA.

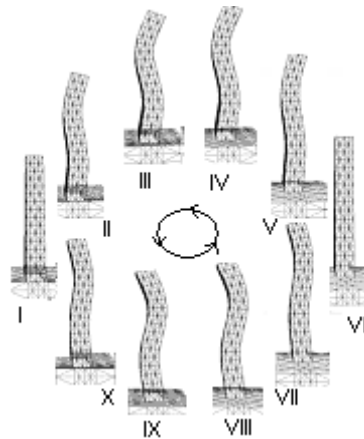


Figure 4.13: ATILA simulation of the motion of the resonator excited by a single piezoelectric layer.

In case of the excitation of other layer on the opposite side, direction of the elliptical motion at the tip is reversed. Stator structure contracts and expands while it bends from one side to other with a $\pi/2$ phase difference between bending and longitudinal vibration.

Second test to verify the matching frequency of cantilever is performed by utilizing both *direct* and *inverse piezoelectric effect*. Direct piezoelectric effect is the generation of electric field due to mechanical stress while inverse piezoelectric effect is the generation of mechanical displacement by electrical field change. One ceramic layer is driven with variable frequencies and the voltage difference

between the surfaces of other layer is measured via oscilloscope. Resonance modes cause the beam to move with great amplitudes and hence cause to generate large voltage outputs on the other ceramic layer. Voltage peaks are mapped within the region of shifted frequency driving signal. Despite the absence of specific test and measurement facilities to identify the exact modes for corresponding frequencies, the observations of occurrence of larger amplitude voltage gain around 70 kHz is interpreted as the result of the large amplitude deflections due to coupled mode.

The elliptical motion of the tip of the resonator is transmitted to the rotor, intermittently, via the frictional contact between the stator and the rotor. While the stator expands, it will push the rotor along longitudinal axis (x_1 direction) enabling a frictional tangential driving force which will move the rotor due to bending of stator. In order to keep the frictional contact between stator and rotor, two components must be continuously pushed against each other. Spring force is the most common way for contact. Although the force is applied continuously, contact is named as “intermittent frictional” since the contraction of ceramic is faster than the spring and hence contact force is higher in expansion than in contraction of the stator. Difference in between these two forces for two phases of longitudinal vibration prevents the symmetrical part of the elliptical locus to stop the rotor. Therefore, motor should be constructed in such a way that the position of rotor can also vary with respect to the stator without staying still.

4.3 Structure of the Motor

Operational requirements of the piezoelectric ultrasonic motor are extracted from the operating principle. These are: 1) the flexible base differences of rotor and stator, 2) rigid base for clamping the stator, 3) continuously applied pre-stress between stator and rotor.

In order to benefit from the merits of UM which satisfy the design requirements of the actuator for mini swimming robot, operational requirements of the motor are maintained in a structure which shows the following characteristics:

- Simple structure
- Easy manufacturing process
- Compact size
- Lightweight

Based on the previously given operating principle and the initial structural design, three different versions of the motor are developed and manufactured in Mechatronics Laboratory at Atilim University by the author (Tunçdemir and Koç, 2004). Since the operating principle is same in each version, consequent motors do not show large differences. Therefore, structure will be presented via the latest design. Variance and improvements in these versions will be stated following the fabrication of the motor.

The motor is assembled from 8 basic elements which are shown in Figure 4.14. Layered structure leads to low cost manufacturing and fast assembly. In the Figure, parts are exploded in the solid model along their fixing direction.

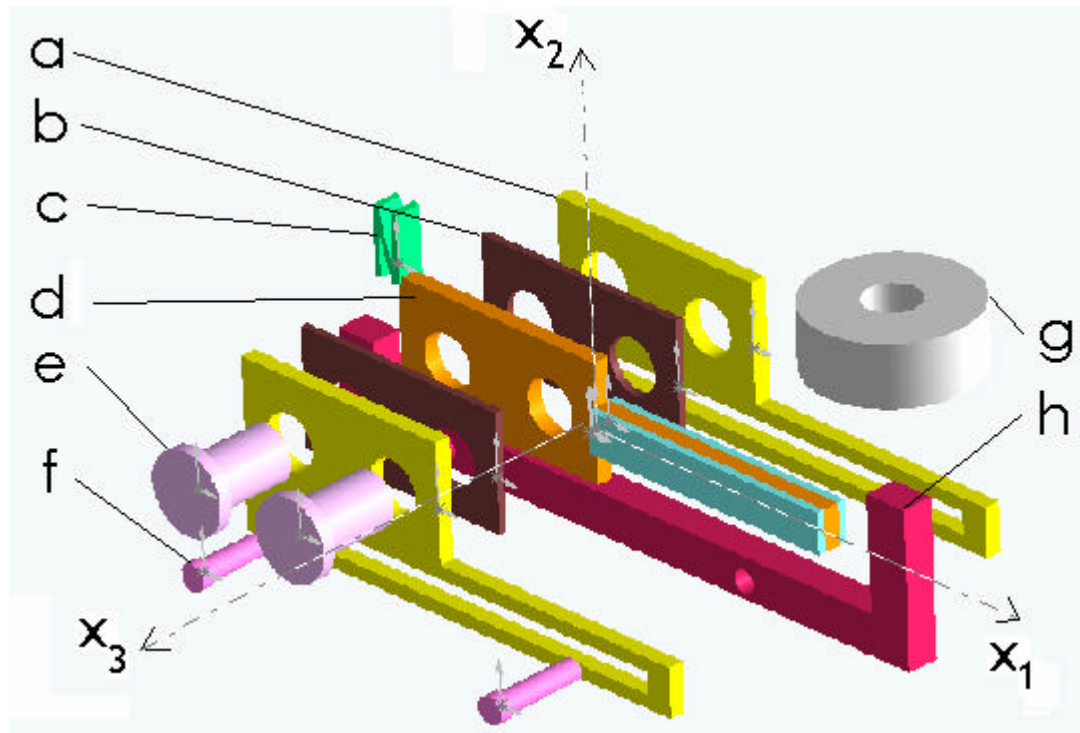


Figure 4.14: Exploded view of the solid model of the motor. (a) Motor case. (b) Intermediate layer of stator. (c) Compression spring. (d) Middle layer of stator. (e) Connecting rods. (f) Sliding rods. (g) Bearing. (h) Rotor base

Piezoelectric ceramics (APC 841, $10 \times 15 \times 0.3$ mm) are attached to the 10 mm extension of middle layer (d), which becomes the resonator of the motor. The stator is obtained by fixing the case of motor (a), intermediate layer (b) with middle layer (d) by 2 mm diameter bolts (e). Single sided roll bearing (g) which is the rotary element of motor is fitted to rotor base (h) along x_1 direction. 0.8 mm rods which are actually pins (f) are fit to rotor base (h) along x_3 direction. On the two rods (f), rotor base and hence the rotor can slide along the slots (in x_1 direction) and groove that are formed by stator elements. Spring (c) which is N-shaped-bent, 0.3 mm, spring steel, presses the stator and rotor to each other on the bearing end of rotor base.

4.4 Fabrication of the Motor

Fabrication process includes three main phases which are listed below:

1. Manufacture of Metal Parts
2. Preparation of Stator
3. Assembly of Motor

Other than the first phase which is the manufacture of metal parts, manufacturing process is wholly carried out by author in Mechatronics Laboratory in Atilim University. Fully self funded manufacturing process is the main reason for the constraint on the cost.

As a merit of layered structure, given in previous section, 3-D machining or forming process is avoided to reduce the machining costs and to make the structure free of the limitations on miniaturization due to the available machining ability. Components are machined in 2-D which reduces the cost of machining such a small workpieces. 0.6 mm and 0.3 mm Phosphorus-Bronze metal sheets specified in Table: 4.1 and 1.2 mm stainless steel sheets are machined by wire-EDM. The reason for choosing wire EDM is the need of the accuracy. Precisely machined cantilever bimorph is required for frequency matching condition and low tolerances for other components are due to the exact alignment requirement of stator and rotor. Although wire-EDM is an expensive machining method, more than 10 sets of motor components can be machined at one time which reduces the machining cost per motor. Machined parts of motor prototypes are shown in Figure 4.15. In the figure, mechanical components belong to the initial, second and latest versions are shown from left to right, respectively. In the figure, outer layer is shown at the top, while intermediate layers are shown above the middle layer of stator. Rotor base of each version is placed on the bottom.

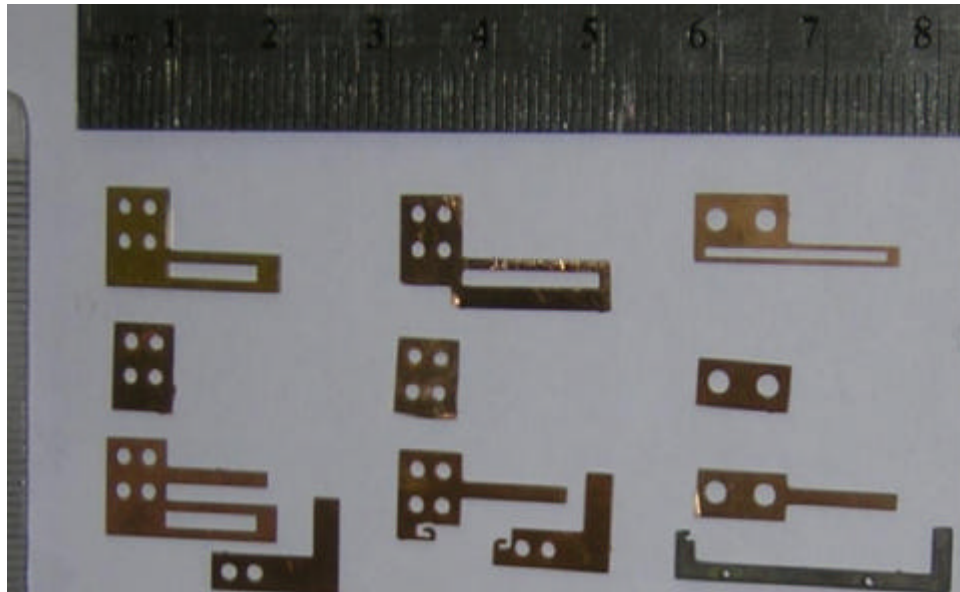


Figure 4.15: 2-D machined components of motor prototypes.

In the second step, piezoelectric ceramics are attached to mid-layer of stator forming the resonator of the motor. Piezoelectric ceramics were supplied from ICAT (International Center of Actuators and Transducers) at Pennsylvania State University, US as properly polarized and cut in specific dimensions.

Negatively polarized surfaces of the ceramics which are previously coated with silver, are cleaned and cantilever extension of the middle layer of stator is grinded for better gluing performance. Adhesive layer for gluing the ceramics to the elastic layer is obtained by the mixture of “STYCAST 2651MM BLACK” Emerson&Cuming’s epoxy and “CATALYST 15LV BLACK” Emerson&Cuming’s catalyst in 3/1 weight ratio. Negatively poled surfaces of two ceramics and both faces of the cantilever extension of mid-layer of the stator are coated with a thin epoxy layer. Pressure is applied onto the surfaces of resonator (from the positive surface of the ceramics) for distributing epoxy equally on the surfaces in order to obtain uniform bonding by a thin epoxy layer. Negatively polarized surfaces of ceramics are assumed that they are electrically grounded by fixing the ceramic surface to the metal layer.

Heat treatment is necessary for epoxy-layer to turn into a strong and solid bonding material even at micro thicknesses. Resonator which is glued with epoxy and compressed between surfaces is put inside an incubator at 100°C for 1 hour.

After the ceramics are attached to metal layer to form the resonator, electrical connections of ceramics are done via the positive surfaces as shown in Figure 4.16. In the figure, resonators for the stators of 3 versions of the motor are shown in a chronological order from top to bottom. Metal layer and hence the negative surface of the piezoelectric ceramics are grounded.

Final step of fabrication is the assembly of previously obtained components. Assembly directions of components are given in Figure 4.14 as the explosion directions. Stator layers are fixed to each other with M2 bolt and nut. Spring which is made up from proper deformation of spring-steel strip is glued to the rotor base. After constructing the stator, rotor base is aligned to stator with two sliding rods. Finally, bearing is fixed to rotor base, pressing to the stator because of the spring.

Avoiding the 3D machining and utilizing the layered structure are in good compliance with the goal of simplicity. As a result of the fabrication, pictures of the prototypes are given in the next section.

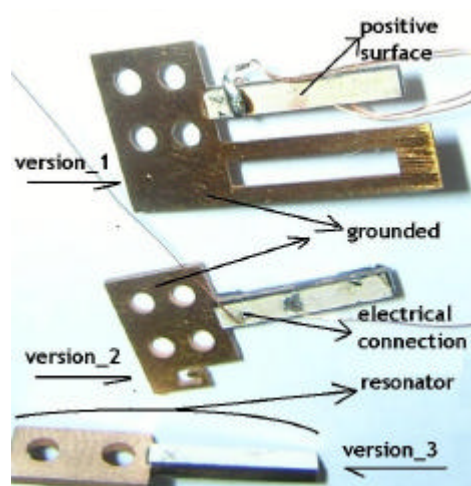


Figure 4.16: Resonators of prototypes

4.5 Prototypes of the Motor

Three versions of the motor are presented in Figure 4.17. In the figure, three different views of each version are given in a table format. Columns indicate the perspective and rows indicate the version while the latest is shown on the bottom.

In the initial version, (V1) (Figure 4.17 a, b, c), stator and rotor is pressed against each other by a helical spring which is connected to rotor at sliding rods.

In the second version (V2) (Figure 4.17 d, e, f), spring is taken inside of the motor for reducing the dimensions and for enhancing the mounting characteristics of the motor. Dimension of the motor is reduced from 22x9x12 mm to 21x9x7 mm. Spring is connected to stator and rotor via hooks which are extended from rotor and the stator. Although the spring is taken inside for increasing the reliability and applicability of motor, V2 still suffers from alignment problem of stator and rotor.

In the third version (V3) (Figure 4.17 g, h, i), helical spring is replaced by a two-fold leaf spring. Eliminating the helical spring and the hooks at stator and rotor reduced the mechanical complexity. Assembly time for motor is also reduced significantly since time for attaching the 6 mm spring to the hooks was half of the total time for whole assembly. The number of bolts used to fix stator is reduced to two but the diameter of bolts is increased from 1.5 mm to 2 mm. Prototype of V3 has the dimensions 25x6x6 mm. One of the main goals of V3 is increasing the mechanical stability by reducing the couple moment which is due to the non-axial interaction of stator and rotor.

In the first two versions, the direction of the spring force between stator and rotor is not along the longitudinal axis of resonator. Therefore, two equal forces (spring force and the *vibro-impact* of resonator to the rotor) create couple which causes the rotor base to rotate at any of the contact points of sliding rods. One of the reasons leading the loss of contact between stator and rotor in case of mechanical disturbance during the operation is avoided by improved design. However, the performance of the motor is still unfavorably low.

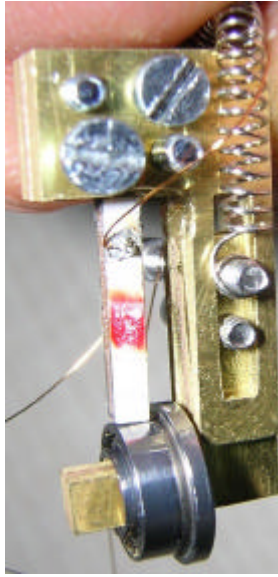
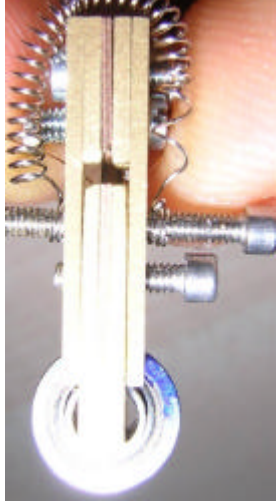
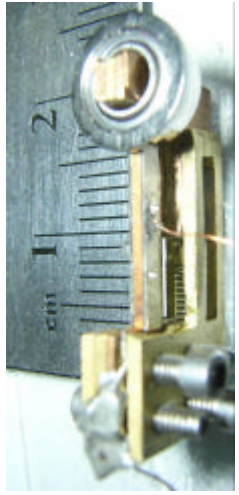
	General View	Side View	Bottom/Top View
V1	 a)	 b)	 c)
V2	 d)	 e)	 f)
V3	 g)	 h)	 i)

Figure 4.17: Pictures of the prototypes of motor

4.6 Driving Circuitry of the Motor

Bidirectional rotation of motor is due to the symmetric piezoelectric elastic laminate cantilever structure of the resonator. In the motor, two piezoelectric layers are utilized separately for specific direction of rotation. Each piezoelectric ceramic layer in the motor is excited at the same frequency with natural frequency of the cantilever bimorph.

To get long battery life in a compact form, the power dissipation of the driving electronics must be as small as possible. Meanwhile, whole circuit which supplies high voltage signals at high frequencies should be small and lightweight for satisfying the design specifications of a mini swimming robot. Voltage is set up by means of a switching amplifier instead of linear amplifier since efficiency of latter is lower than that of former for high voltage at high frequency applications (Campolo, 2003).

Switching amplifier can be classified as a single-ended multi-resonant (SE-MR) amplifier (Lin, 1997). SE-MR amplifier is capable of delivering a sinusoidal voltage to the load and achieving zero-voltage switching for the main switch. In order to amplify input voltage to ceramics, sinusoidal driving signal is kept at resonance. For achieving an idealized resonant circuit at undamped natural frequency, LC-series resonant circuit is utilized. Rather than using a parallel resonant circuit, series resonant circuit provides voltage amplification at resonance (Hayt et al., 2002). Resonance occurs when the voltage and current at the input terminals are in phase which correspondence to a purely real admittance. Necessary condition for this is given by equation (4.72);

$$\omega_0 C - \frac{1}{\omega_0 L} = 0 \quad (4.72)$$

Resonant frequency is expressed as in (4.73) or (4.74).

$$\omega_0 = \frac{1}{\sqrt{LC}} \text{ rad/s} \quad (4.73)$$

$$f_0 = \frac{1}{2p\sqrt{LC}} \text{ Hz} \quad (4.74)$$

In the series resonant circuit, capacitive element is the static capacitance (C_s) of ceramic layer which is equal to the electrical equivalent of piezoelectric layer for ideal case. For equating the resonance frequency of the circuit to the calculated natural frequency (f_0) of cantilever bimorph, inductor (L) is adjusted in (6.3) according to the measured static capacitance of ceramic layer. For $f_0=70$ kHz and $C_s=0.6$ pF, L is calculated as 9 mH (4.74).

Resonant inverter circuit given in (Chang, 2004) is adapted for bidirectional rotation of the motor. Circuitry built for the bidirectional motor is shown in Figure 4.18. In the circuitry, frequency of the sinusoidal waveform before C_s is equal to the switching frequency (S_r) of the main switch. BD-139 (Philips, 2004) switches the DC supply voltage for resonant circuitry by square wave signal (S_r) at resonance frequency, f_0 .

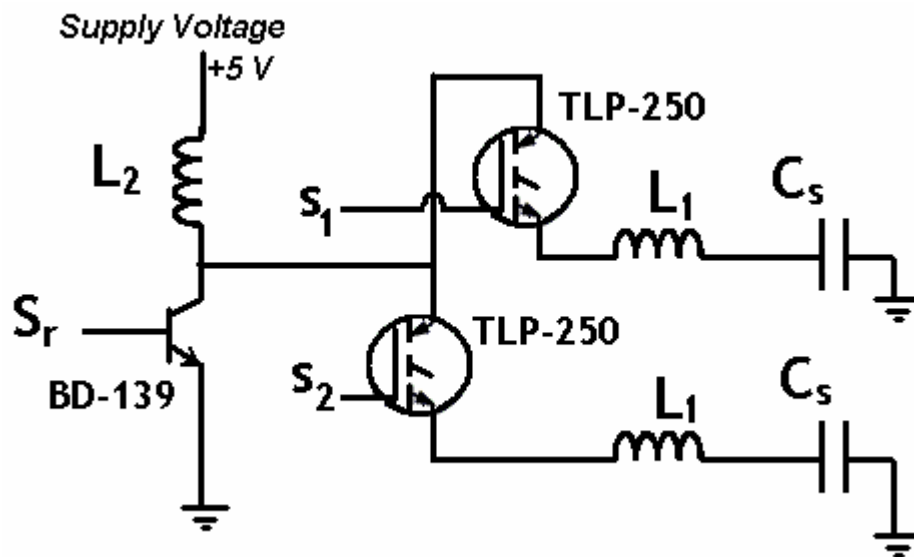


Figure 4.18: Driving circuitry of motor

Because of the equal characteristics of each layer, single source of the motor should be switched for each layer. Second type of switch used in the circuitry is TLP-250 (Toshiba, 2004) which is a optocoupler for isolated gate bipolar transistor (IGBT). Optocoupler is utilized for controlling the connection or disconnection between the voltage source and ceramic layer. High speed, high voltage signals can be switched by TLP-250 which is driven by TTL signals (s_1) and (s_2). Therefore, bidirectional rotation can be controlled with TTL that are isolated from the voltage source.

4.7 Measuring the Characteristics of the Motor

Before applying the motor on mini swimming robot, speed of revolution, no-load torque and power consumption are measured. Load characteristics are obtained and shown in a torque-speed and efficiency-speed curves. Torque of the motor is calculated using a transient characterization method (Nakamura et al, 1991). In the measuring system which is schematically illustrated in Figure 4.19, a rotary encoder is mounted on the motor by means of a coupling rotary inertia disk.

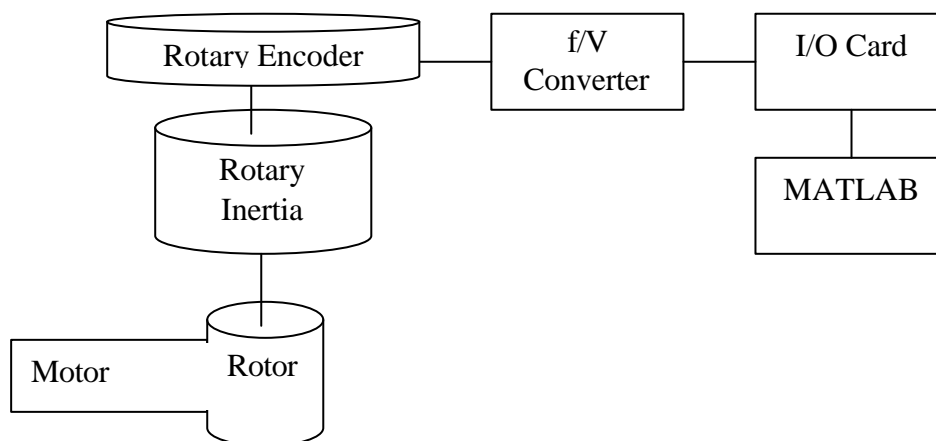


Figure 4.19: Block diagram of the measuring system.

Angular acceleration of the motor (\ddot{q}) is measured as MATLAB output in the measuring system. Torque (T) is calculated according to the equation given in (4.75), where J denotes the polar moment of inertia of the load including the rotor of motor, rotary inertia and rotary encoder. Using (4.75), starting transient response of the motor gives the speed-torque relation.

$$T = J \cdot \ddot{q} \quad (4.75)$$

Rotary inertia which is mounted on the motor acts as coupler between motor and rotary disk of the optical encoder (US Digital, HEDS-9100-S00) as shown in Figure 4.20. Total polar moment of inertia of the load is calculated as $0.64 \text{ kg} \cdot \text{mm}^2$ and details of calculation with the material and geometrical properties of the rotary elements are presented in Appendix-C. The motor is driven at 69 kHz with DC supply-voltage of 5 V using the circuit given in Figure 4.18.

As shown in Figure 4.19, the transient position data is first converted to variable pulse train on rotary encoder. Variable frequency pulse train is expressed as voltage signal which corresponds to a specific angular speed, using a frequency-voltage converter. Linear frequency-voltage converter LM2907 is utilized for measuring transient characteristics of the motor (National, 2004), (Koc et al., 2002). Voltage expression of angular speed of the rotor is fed to MATLAB through analog input port of HUMUSOFT MF 614 Multifunction I/O Card.

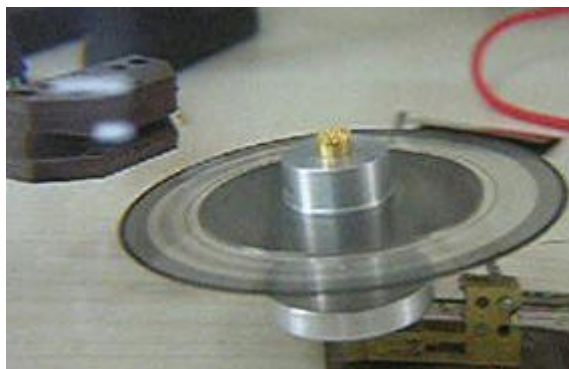


Figure 4.20: Rotary inertia and encoder disk mounted on the motor.

A MATLAB Simulink[®] model is built for real-time data acquisition from the I/O card. Corresponding speed values are converged from the input voltage from LM2907 in MATLAB (Appendix-D) before obtaining the motor characteristics. Flowchart of the algorithm followed for obtaining motor characteristics from angular speed data acquired via real-time data acquisition card in MATLAB is also supplied at Appendix-E. As presented in Appendix-E, the angular acceleration of the motor is estimated using the numerical differentiation of the angular speed at each time interval. Torque is calculated according to the formula given in (4.75) and power is obtained by multiplying the speed and torque at each time step. Transient speed under no-load condition is shown in Figure 4.21. Transient speed and power is plotted as a function of torque in Figure 4.22.

According to the Figure 4.21, the motor's steady state velocity is about 250 RPM (revolution per minute). Since the motor speed does not show monotonically increasing characteristics, there are two speeds where motor produce the single torque.

Maximum torque is about 45 μNm and maximum power output is 0.5 mW (Figure 4.22). Input power is measured as 125 mW, by multiplying 5 V with the drained current from power supply.

Since the motor is not undergone an optimization procedure, the efficiency is not satisfactory.

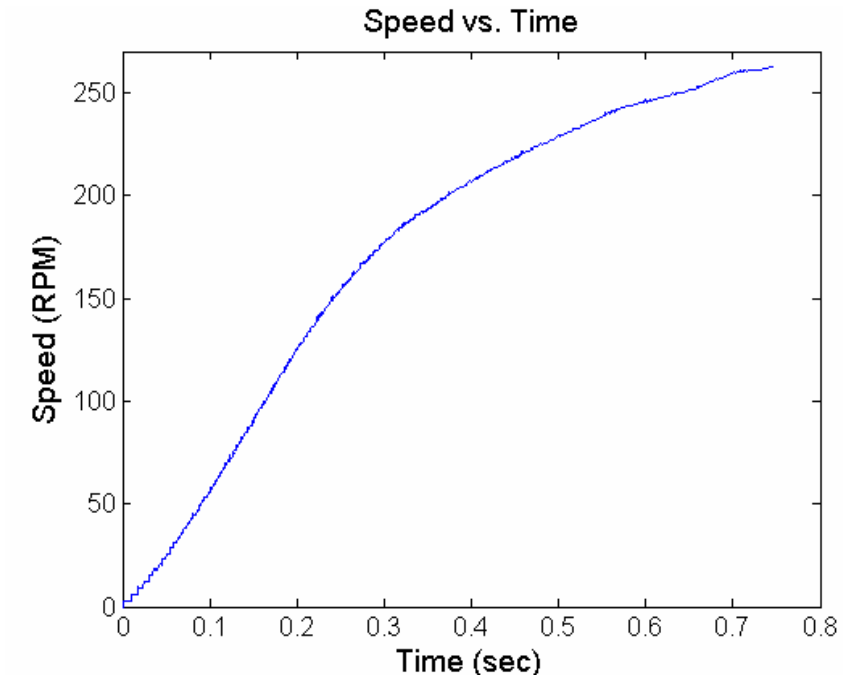


Figure 4.21: Transient speed under no-load condition

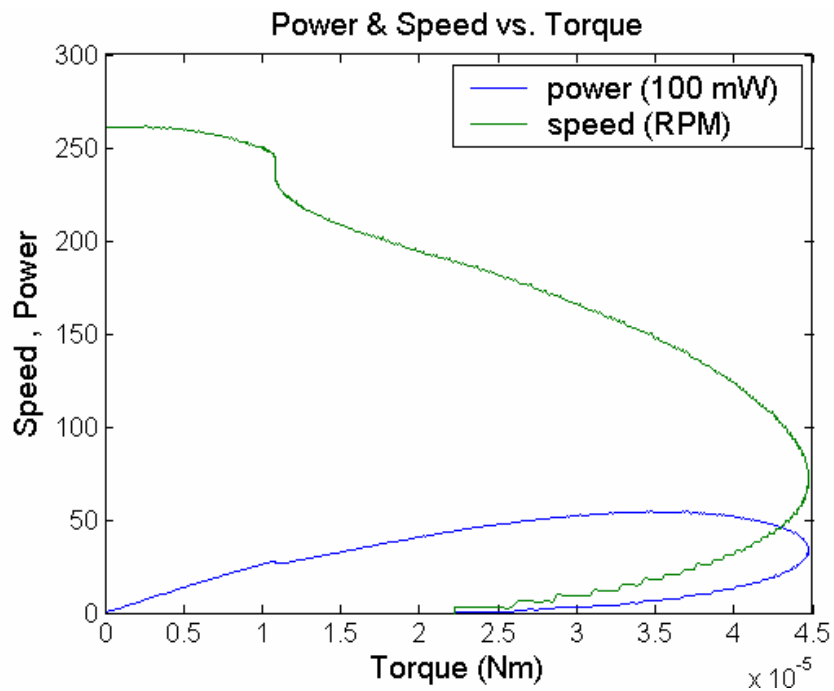


Figure 4.22: No-load characteristics: Transient speed and power as a function of torque

CHAPTER 5

SWIMMING ROBOT

Implementation of the actuator in an ostraciform type swimming mode for obtaining locomotion requires flapping tail motion control as discussed in the sequel.

5.1 Flapping Tail Motion of Swimming Robot

Actuator and driving circuitry is designed according to the design specifications and constraints which were defined previously. Despite the unfavorable performance and low torque gain of the motor, bidirectional motion which can be controlled by TTL is obtained in a compact structure. Moreover, in order to imitate the ostraciform type swimming mode, tail-like structure with controlled degree of oscillation should be added to the actuator.

Thrust generation tests are carried out before applying the actuator on a swimming machine. In the tests, a fin like structure is attached directly to the rotor and direction of rotation is changed periodically. Oscillating tail caused the iron dusts that were intentionally spread on the water, move backward which states the existence of the backward propulsion of water.

5.2 Structure of Flapping Tail Actuator

Structure of flapping tail actuator presented in (Tunçdemir et al., 2004), includes an elastic fin attached directly to the rotor. Restricted rotation of the rotor of the motor leads to controlled flapping of the tail. For commanding the bidirectional

rotation of the rotor, control is implemented on the driving circuitry that is given in Figure 4.18. By means of the non-touching encoder, the degree of rotation of the rotor and flapping angle is fed back to the circuitry. Feedback signal is processed by the microcontroller, PIC12F675 (Microchip, 2004) for controlling the excitation period of each piezoelectric layer.

Flapping tail actuator of the robot including the block diagram of the drive circuitry is illustrated in Figure 5.1. In the figure, resistor-set linear oscillator (LTC1799) supplies the required signal for switching transistor (BD139). BD139 switches at the matching resonance frequency of L1 and B3 modes. Thus, on-board DC supply voltage of 5V and 25 mA is converted to a sinusoidal signal with $180 V_{\text{peak-to-peak}}$ via the principles explained with driving circuitry of the motor. Each optocoupler (TLP250) is used to route the high voltage- high frequency signals by TTL from microcontroller.

5.3 Control of Angular Rotation

Microcontroller, (Microchip-PIC12F675) operates in a closed loop which determines the direction and the period of rotation of the rotor. Feedback to the microcontroller is through a non-touching encoder. Non-touching encoder which is shown with dashed-line in Figure 5.1 is composed of a gray-gradient slip attached to the rotor and a reflective optic sensor (CNY70). Gray value of the slip corresponds to a preset angle of rotation of the motor.

Sensor converts the intensity of the light reflected from the slip into analog voltage output. As the reflected light will vary with the corresponding region of the slip, degree of rotation of the rotor is expressed as an analog voltage value by means of the non-touching encoder. Analog output from CNY70 is supplied to the analog input port of PIC12F675. PIC12F675 is an 8-bit microcontroller with 8 pins and 6 I/O pins one of which can be programmed for analog input.

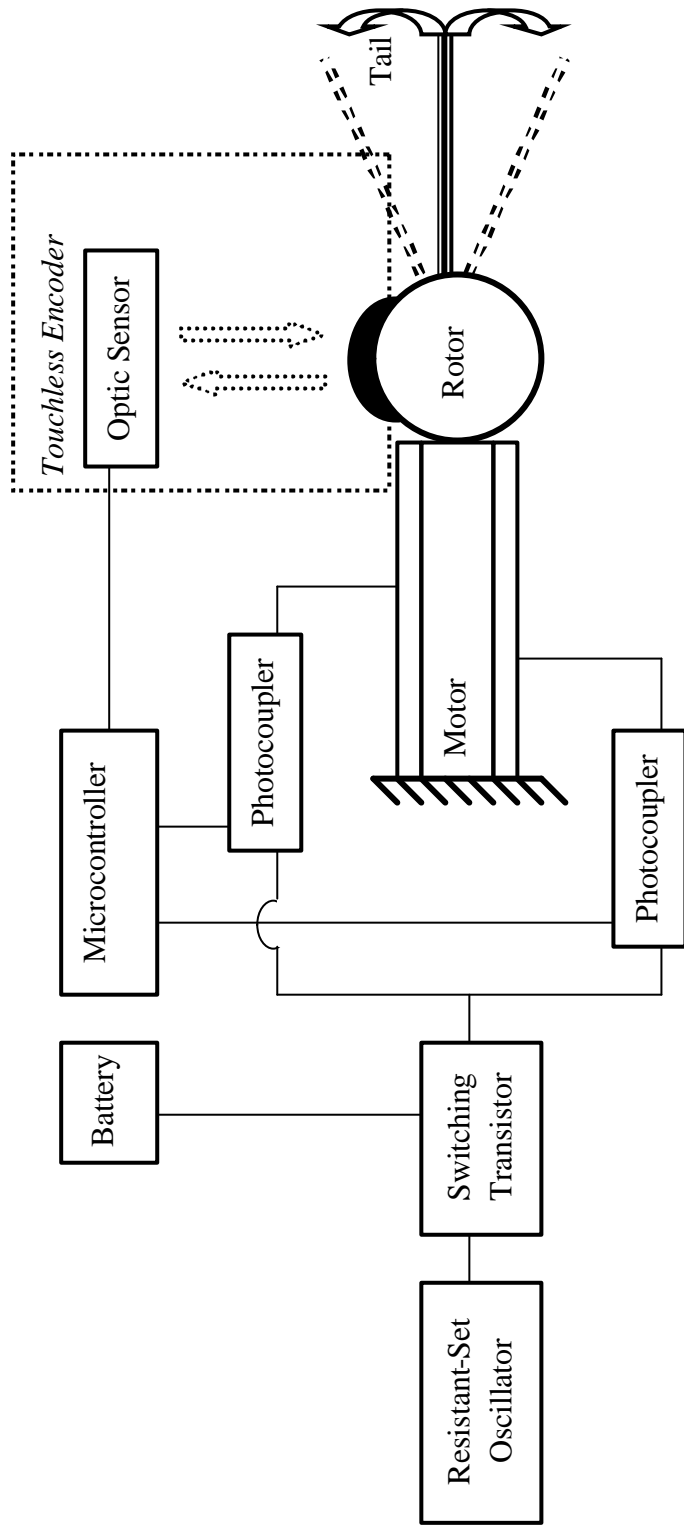


Figure 5.1: Block diagram of the flapping-tail actuator

With its A/D conversion and comparator module and without requiring an external oscillator, it is suitable for mini-mobile robotics applications due to its functional design in a compact form. Although the input can be digitized with 10-bit resolution, most significant three bits are utilized for the A/D conversion of the input signal. Algorithm implemented in PIC12F675 returns the on/off time of each photocoupler after each successive A/D conversion. Although, on/off time scheduling of photocouplers can be arranged for different degree of rotation variations, algorithm is implemented to discriminate two distinct flap angles. Flowchart of the algorithm for determining the triggered photocoupler according to the degree of rotation is given in Appendix-E. PIC is programmed through ALL-11 programmer and MPASM-developer using PIC-assembler. Assembler code, including the initializing steps for analog input, A/D conversion is supplied at Appendix E.

5.4 Test Boat as the Preliminary Design of Mini Swimming Robot

Preliminary tests are carried out on a test-boat for the fine tuning of actuator which is shown in Figure 5.2 and Figure 5.3. Boat is designed to be half of the fish robot along its height. 0.5 mm 9020-Styrene Plastic Sheet is used as the hull, which weights only 5 gr. Control circuitry is implemented on a printed circuit board (PCB) for on-board control of the robot. Non-touching encoder is fixed to the motor. Encoder attached motor, hull, batteries, inductor array and printed drive-circuitry are shown in Figure 5.2. Figure 5.3 shows the flapping tail actuator mounted on the test boat.

Electrical characteristics are measured and final tests on the circuitry are performed for determining the power requirements. NiMh 11AAAM type batteries are chosen to be most appropriate according to the observed operating conditions given in Table 5.1.

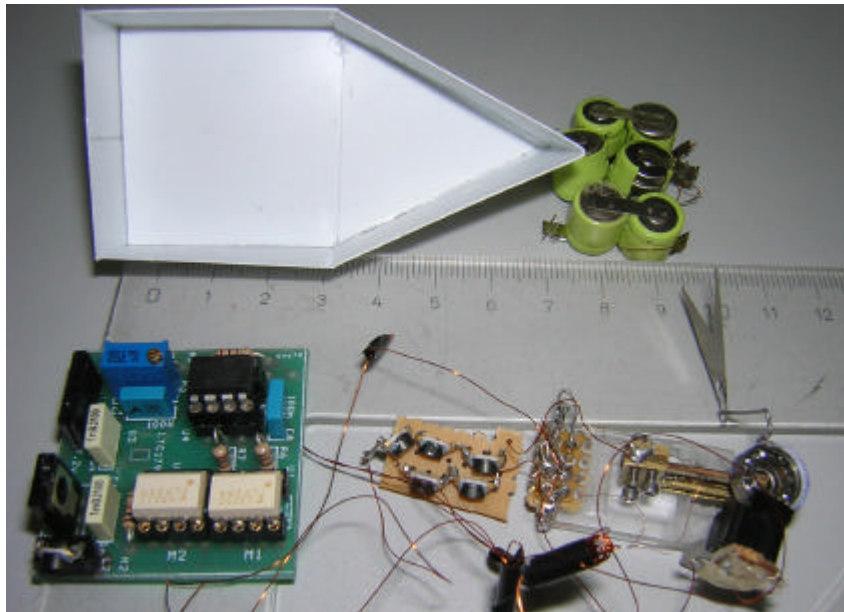


Figure 5.2 Components of the swimming robot.

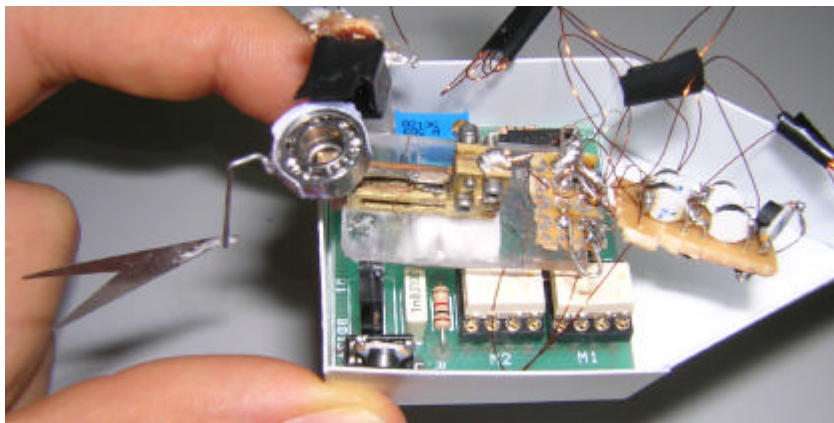


Figure 5.3: Test Boat and the fin attached actuator.

Table 5.1 Weight and power requirements of the components.

Component	Power Requirement	Weight
Microcontroller	5 V, ~10 mAh	2 gr.
Encoder	5 V, ~50mAh	4 gr.
Driving Circuitry	5 V, ~20mAh	10 gr.
Motor	5-7 V, ~30 mAh	4 gr.
Hull	-	2 x 5 gr. = 10 gr.
Batteries, 1.2 V 110 mAh	-	6 x 3 gr. = 18 gr.
Total	5-7 V, ~110 mAh	~48 gr.

CHAPTER 6

CONCLUSION

As the conclusion of this study, discussion of the work is presented and contribution of the thesis is given before the suggestions for future work..

6.1 Discussion

The aim of the thesis is to design a mini swimming robot. The largest dimension of the robot is planned to be smaller than 10 cm in order to classify the robot as mini.

Dimensional constraints on the robot bring additional constraints on the subsystems. For this purpose, the effects of scaling down some physical quantities are analyzed for subsystems of the robot. As a result of the analysis of scaling effects, actuator is determined to be the most critical component of a mini swimming robot. Available actuators that are utilized in swimming robots are investigated thoroughly. Investigation of actuators revealed that actuation including the material and mechanism development is a key technology for not only the mini swimming robots but whole field of micro/mini mobile robotics. Since the progress in actuators will heavily affect the future development and miniaturization of swimming robots, the emphasis of the thesis is placed on the area of actuators.

Fish-like swimming is selected for underwater locomotion due to its proven supremacy in nature. Swimming robot (SR) is defined as the underwater free floating robot which utilizes fish-like locomotion. Biomimicry of fish swimming

for SR is examined by classifying and characterizing the swimming modes in fish and their adoptability on robots. Although the research on swimming robots is focused more on *Carangiform* swimming mode, *Ostraciform* swimming is selected because of its simple characteristics to model, analyze and build. Single joint controlled flapping tail motion is proposed for the final behavior of the actuator.

In this study, the complexity of the field of swimming robotics is also highlighted. Real progress in this area requires interdisciplinary efforts and contributions from different research fields including hydrodynamics and control of deformable bodies in compressible environments, advanced material developments for hull and actuator, mechanism synthesis and fluid mechanics for wake generation by undulatory body motions. Despite the requirement of multidisciplinary research on SR topic, this thesis contributes to SR studies by development of a novel actuator utilizing inverse piezoelectric effect.

Available SRFL and their actuators are discussed in detail. Robots are compared according to the utilized actuation method and material, imitated swimming mode, body length, appropriateness for further miniaturization, swimming speed and tail oscillation frequencies. The dependency of swimming speed of SRFL to oscillating frequency is observed. Increasing the tail-beat oscillation and amplitude leads faster robots. SRFL with wide range of oscillating tail frequencies are more agile and have better maneuvering characteristics. Inapplicability of the conventional actuation methods to small scale systems and the trend of making use of smart actuators for small scale applications are highlighted explicitly in the thesis.

Design constraints of actuators in mini swimming robots are ascertained as; broad range of operating frequency, high power and torque density, sustained efficiency for downscaling, low operating power requirement and easily applicable output motion generation. A new type piezoelectric ultrasonic motor is designed according to the appointed specifications and constraints.

Available piezoelectric motors were investigated. It was observed that the simpler the structure, the easier the miniaturization and commercialization of these motors. The motor can be distinguished from its predecessors by its simple structure. Motor utilizes the excitation of a piezoelectric layer at the matching frequency of the B3 and L1 modes. Symmetric piezoelectric/elastic laminate cantilever structure is used as the stator in order to avoid holding problem of the vibrator. Two methods are proposed for tailoring the resonator for frequency matching. Length to thickness ratio of the cantilever beam is set in order to match the resonance frequencies of first longitudinal and third bending modes. Although only one method is utilized in this work, other method is suggested for fine tuning and optimizing the motor. Simple holding mechanism of the whole body and simple stator structure with single driven ceramic for a specified direction of rotation, bring the simplicity of the whole motor design. Reducing the mechatronic complexity is one of the key ideas in the design for miniaturization of the motor. Simplicity in design leads to easy, reliable and low cost manufacturing process.

Before fabricating the motor, theoretical results are reconsidered and tuned by using ATILA finite element software. The elastic layer thickness is decided to be 0.45 mm and driving frequency of 70 kHz is selected.

As a merit of layered structure of the motor, 3-D machining or forming process is avoided to reduce the machining costs and to make the structure free of the limitations on miniaturization. Precisely machined cantilever bimorph and other components are required for frequency matching condition and exact alignment requirement of stator and rotor. Without the precision in manufacturing, a robust motor can not be obtained. Avoiding the 3-D machining and utilizing the layered structure are in good compliance with the goal of simplicity.

Other than the manufacture of metal parts, manufacturing process is wholly carried out by author in Mechatronics Laboratory in Atilim University. Fully self funded fabrication is the main reason for the constraint on the cost. Despite the need of precise manufacturing methods and facilities for the construction of such a small motor, actuator was built-up by utilizing and adopting the available methods and

facilities designed for macro applications because of the limited funding. Although the fabrication procedure is quite common, design and manufacture of the ultrasonic motor is adopted for available tools.

Fabrication of the resonator is one of the most sensitive steps in manufacture since it needs precisely placed components to be fixed by a thin adhesive layer. Slight increase in thickness of adhesive layer which yields to reduced electrical conduction between ceramic and elastic layer will demolish the grounded-surface assumption and will cause the motor to operate improperly. Moreover, bimorph-structure assumption is based on neglecting the thickness and effects that are not due to the elastic and piezoelectric layer. Therefore, arrangement and control on the thickness of adhesive layer is crucial in ultrasonic motor design. However, more than 70 % of the resonators built by author could not be utilized in motors successfully because of the faults in manufacturing most of which are due to the imprecise machining and unsymmetrical layered structure of resonators.

The last prototype has the dimensions of $25 \times 6 \times 6$ mm and attains 300 rpm at no load condition when driven with a single AC source ($180 V_{\text{peak_to_peak}}$, at 68.5 kHz) that is converted with an inverter circuitry from 5 V DC source drawing 25 mA. Due to its low voltage driving and gearless mechanism, motor is suitable for battery operated micro robotic applications.

Improvements of motor, via two additional versions, are achieved for increasing the power efficiency, torque output of the motor and for obtaining more robust design which is insensitive to the disturbances. Nevertheless, final design can only produce 0.5 mW for 125 mW input. Maximum torque of the motor is limited with $45 \mu\text{N}$. Main reasons for low efficiency and low output torque are the missing optimization step for the motor and the imprecise fabrication. Effects of geometrical fine tunings and driving frequency shifting on frequency coupling and elliptical trajectory generation (which are closely related to the performance of the motor) could not be observed due to the absence of a high speed camera or a laser vibrometer. Imprecise fabrication causes misalignments which results in an unreliable design due to the intolerable disturbance while operating.

Motor is implemented on the flapping tail actuator with a maximum beating frequency of 8 Hz in air but lower than 1 Hz in water. Beating frequency and amplitude as well as the spanning angle of the elastic fin-like structure attached to the motor is controlled via a non-touching encoder and a microcontroller. Results of the initial measurements of the actuator system in air are promising with high oscillation frequency range and compromising amplitude and frequency control.

Before submerging the robot, preliminary tests are carried out on a 6 cm test-boat. Oscillation frequency is drastically lowered in water due to the low torque output of the motor and fin-like structure can not generate propulsion. In addition to this, tests on the boat showed that the ignored dynamic effects such as the inertial forces etc. disturb the stability of the robot. Because of the dynamically unstable system, thrust generated by the tail motion can not be transformed to a forward motion.

Nonetheless, developed actuator is a promising design since it has key specifications for mini swimming robots even it has not been optimized and carefully tuned yet. Prominent features of present state of the actuator are:

- Low power battery operated driving conditions and compact circuitry,
- Bidirectional highly controllable flapping with quick response,
- Small size with simple structure allowing for further miniaturization.

Developed actuator system is a good candidate to be utilized in mini swimming robots if slight improvements on the design, test and fabrication phases are performed.

6.2 Contribution of the Thesis

Constraints on the design of mini swimming robot are specified. Scaling effect on components of a robot is firstly studied for a swimming robot in which there is a strict dimensional constraint.

A detailed summary of the available swimming robots with fish like locomotion is presented briefly and locomotion characteristics of the robots are classified. Different from the previous surveys on swimming robots, this study focuses on the robots with fish-like swimming and their actuators.

Although forward swimming speed and tail beat oscillation frequency has been related in many studies, this work gathers the experimental results of many researchers and shows that the general speed-oscillation relation is consistent with the individual findings.

Although there are examples of piezoelectrically actuated swimming robots for the first two categories of piezoelectric actuation architectures as internally leveraged and externally leveraged PZT actuators, there is not any example for the third category which is the frequency leveraged PZT actuators. This study fills the gap for the example of third category.

The motor designed for flapping tail actuator is a unique rotary piezoelectric ultrasonic motor having various virtues compared with its predecessors.

Although tailoring the dimensions of a uniform width cantilever symmetric piezoelectric/elastic laminate for resonance frequency matching of longitudinal and bending vibrations are proposed previously, the second method explained in this study for tailoring a tapered symmetric piezoelectric/elastic laminate is unique in the literature.

6.3 Suggestions for Future Work

A precise method should be followed while building the resonator in order to obtain symmetric laminate structure attached by an adhesive layer with negligible thickness for accurate frequency matching.

Elliptical trajectory of the vibrator should be observed and fine tuning of stator design and driving frequency modulation should be performed according to the observations from a high speed visualization utility and frequency response tests.

Second method proposed for tailoring a tapered beam can be applied for fine tuning if precise measuring and machining utilities are available.

After obtaining a high performance and a robust motor, actuator system should be tested by varying flapping tail actuator parameters in order to characterize and model the locomotion and robot. Varying the elasticity and dimensions of fin-like structure and changing the frequency and amplitude of tail-beat will respond differently. Results of these experiments will supply important data to estimate the locomotion characteristics and the model of the robot to design command and control strategies.

In order to call the swimming boat as a robot, it should act in a predetermined way by responding the environmental changes. For input to the system perceptive or communicative devices should be integrated onto the hull as a next step of the design.

REFERENCES

Anderson, J. M and Kerrebrock, P. A, 1999, “The Vorticity Control Unmanned Undersea Vehicle (VCUUV) Performance Results”, *11th International Symposium on Unmanned Untethered Submersible Technology*, Durham, NH.

Anderson, J. M and Kerrebrock, P. A, 2000, “The Vorticity Control Unmanned Undersea Vehicle (VCUUV): An Autonomous Robot Tuna”,
[url:http://www.draper.com/publications/digest2000/paper6.pdf](http://www.draper.com/publications/digest2000/paper6.pdf),
(Included in CD – Download Date: 19.07.2004).

Anthony Lucas-Smith, 1999, “Chapter 7: Actuators”, in, Rzevski G., Edt., *Mechatronics, Designing Intelligent Machines Volume 1 Perception, Cognition and Execution*, Alden Press, Oxford, United Kingdom, pp. 195-217.

Aoyagi, M. and Tomikawa, Y., 1993, “Ultrasonic Rotary Motor Using Longitudinal and Bending Multimode Vibrator with Mode Coupling Caused by External Additional Asymmetry”, *Japanese Journal of Applied Physics (JJAP)*, Vol. 32, pp. 4190-4193, Part 1, No. 9B.

Aoyagi, M. and Tomikawa, Y., 1996, “Ultrasonic Motor Based on Coupled Longitudinal-Bending Vibrations of a Diagonally Symmetric Piezoelectric Ceramic Plate”, *Electronics and Communications in Japan*, Part 2, Vol. 79, No. 6, pp 60-67.

Aquaroid, 2004, <http://www.toysfinder.com/aquaroid/aquaroid.html>
(Included in CD – Download Date: 21.12.2004).

Ayers, J., Wilbur, C. and Olcott, C., 2000, “Lamprey robots”. *Proceedings of the International Symposium on Aqua Biomechanisms*, Tokai University.

Ayers, J., 2001, "Lamprey Robot in Northeastern University",
<http://www.neurotechnology.neu.edu/lamprey.html>
(Included in CD – Download Date: 19.07.2004).

Bainbridge, R., 1958, "The speed of swimming of fish as related to size and to the frequency and amplitude of tail beat", *Journal of Experimental Biology*, Vol. 35, pp.109-133.

Barrett, D. S., Triantafyllou, M. S. and Yue D. K. P., 1999, "Drag reduction in fish-like locomotion", *Journal of Fluid Mechanics*, Vol. 392, No. 10, pp. 183-212.

Bexell, M. and Johansson, S., 1996, "Characteristics of a piezoelectric miniature motor", *Proceedings of 5th International Conference on New Actuators (ACTUATOR96)*, Bremen.

Bexell, M. and Johansson, S., 1999a "Fabrication and evaluation of a piezoelectric miniature motor", *Sensors and Actuators*, Vol. 75, pp. 8-16.

Bexell, M. and Johansson, S., 1999b "Characteristics of a piezoelectric miniature motor", *Sensors and Actuators*, Vol. 75, pp. 118-130.

Biomechatronic, 2004, "Biomechatronics - A Swimming Robot Actuated by Living Muscle Tissue", http://biomech.media.mit.edu/research/pro2_3.htm
(Included in CD – Download Date: 21.12.2004).

Borgen, M. G., Washington, G. N. and Kinzel, G. L., 2003, "Design and Evolution of a Piezoelectrically Actuated Miniature Swimming Vehicle", *IEEE/ASME Transactions on Mechatronics*, Vol. 8, No. 1, pp. 66-76

Campolo, D., Sitti, M., Fearing, R. S, 2003, "Efficient Charge Recovery Method for Driving Piezoelectric Actuators with Quasi-Square Waves", *IEEE Ultrasonics Ferroelectrics and Frequency Control (UFFC)*, Vol. 50 No. 3.

- Caprari, G., 2003, "Autonomous Micro-Robots: Applications and Limitations", Ph.D. Dissertation, http://asl.epfl.ch/aslInternalWeb/ASL/publications/uploadedFiles/Caprari_phd2753.pdf (download date 11.07.2004)
- Caprari, G., Estier, T. and Siegwart, R., 2002, "Fascination of down scaling- Alice the sugar cube robot", *Journal of Micromechatronics*, Vol.1, No.3, pp177-189.
- Chang, K.-T., 2004, "Finding Electrical Characteristics of a Piezoelectric Transformer through Open-Circuit Operation", *Japanese Journal of Applied Physics* Vol. 43, No. 9A, pp. 6204–6211.
- Chiu, F.-C., Guo, J., Chen, J.-G. and Lin, Y.-H., 2002, "Dynamic characteristic of a biomimetic underwater vehicle", *Proceedings of the 2002 International Symposium on Underwater Technology*, pp. 172-177
- Colgate, J. E. and Lynch, K. M., 2004, "Mechanics and Control of Swimming: A Review", *IEEE Journal of Oceanic Engineering*, Vol. 29, No. 3, pp. 660-673,
- Dai, X., 2003, "Some New Progress of Advanced Robotics in China" report to JCP'2003 OF IARP, www.iai.csic.es/iarp/sapr/05_CHINA_IARP_JCF_2003.pdf, (Included in CD – Download Date: 21.12.2004).
- Dario, P., Valleggi, R., Carrozza, M. C., Montesì, M. C. and Cocco, M., 1992, "Microactuators for microrobots: a critical survey", *Journal of Micromechanics and Microengineering*, Vol. 2, pp. 141-157.
- Dudek, G. and Jenkin, M., 2000, *Computational Principles of Mobile Robotics*, Cambridge University Press, New York.
- Edd, J., Payen, S., Rubinsky, B., Stoller, M. L., and Sitti, M., 2003, "Biomimetic Propulsion for a Swimming Surgical Micro-Robot," *Proc. IEEE/RSJ Intl. Conf. on Intelligent Robots and Systems*, Las Vegas, Nevada.

FACE, 2004, ‘Face International - THUNDER Home Page - Thunder Actuators’,
<http://www.face-int.com/thunder/thunder.htm>,

(Included in CD – Download Date: 11.12.2004)

Fearing, R. S., 1992, “Micro Structures and Micro Actuators for Implementing Sub-millimeter Robots”, *Precision Sensors, Actuators and Systems*, Kluwer Academic Publishers, pp. 39-72.

Fearing, R. S., 1998, “Powering 3 Dimensional Microrobots: Power Density Limitations”, Tutorial on ‘Micro Mechatronics and Micro Robotics’, IEEE Int. Conf. Robotics and Automation

Flaps, 2001, “FLAPS Homegage”,

<http://www.ece.eps.hw.ac.uk/Research/oceans/projects/flaps/describe.htm>

(Included in CD – Download Date: 11.12.2004)

Fleischer, M., Stein, D. and Meixner, H., 1989a, “Ultrasonic Piezomotor with Longitudinally Oscillating Amplitude-Transforming Resonator”, *IEEE Transactions on UFFC*, Vol. 36, No. 6, pp. 607-613.

Fleischer, M., Stein, D. and Meixner, H., 1989b, “New Type of Piezoelectric Ultrasonic Motor”, *IEEE Transactions on UFFC*, Vol. 36, No. 6, pp 614-619.

Flynn, A. M, Tavrow, L. S., Bart, S. F, Brooks, R. A., Ehrlich, D. J., Udayakumar, K. R. and Cross, L. E., 1990, “Piezoelectric Micromotors for Microrobots”, *Ultrasonics Symposium*, pp. 1163-1172.

Fukuda, T., Hosokai, K. and Arai, F., 1990, “Giant Magnetostrictive Alloy Applications to Micro Mobile Robot As A Micro Actuator Without Power Supply Cables,” *Proc. IEEE Conf. Micro Electro Mechanical Systems*, pp. 210-215.

Fukuda, T., Kawamoto, A., Arai, F. and Matsuura, H, 1994, “Mechanism and swimming experiment of micro mobile robot in water”, *Proc. IEEE International Conference on Robotics and Automation*, Vol. 1, pp. 814 – 819.

Fukuda, T., Kawamoto, A., Arai, F., Matsuura, H, 1995, “Steering mechanism of underwater micro mobile robot”, *Proc. IEEE Intl. Conf Robotics and Automation*, Vol.1, pp363-368.

Gopalkrishnan, R., Triantafyllou, M. S., Triantafyllou, G. S. and Barrett, D., 1994, “Active Vorticity Control in a Shear Flow Using a Flapping Foil”, *Journal of Fluid Mechanics*, Vol. 274, pp. 1-21.

Guo, S., Wakabayashi, K., Kato, N., Fukuda, T., Nakamura, T. and Oguro, K., 1997, “An Artificial Fish Robot Using ICPF Actuator”, *IEEE Intl Symposium on Micromechatronics and Human Science*, pp. 205-210.

Guo, S., Fukuda, T. and Asaka, K., 2003, “A New Type of Fish-Like Underwater Microrobot”, *IEEE/ASME Transactions on Mechatronics*, Vol. 8, No. 1, pp 136-141

Guo, J., Tsai, J.-F., Chiu, F.-C., Cheng, S.-W. and Ho, Y.-S., 2003, “Design of a waypoint-tracking controller for a biomimetic-autonomous underwater vehicle”, *OCEANS 2003. Proceedings*, Vol. 1, pp. 333 – 339.

Hayt, W. H., Kemmerly J. E. and Durbin, S. M, 2002, *Engineering Circuit Analysis*, page 561, McGraw Hill, 2002, Sixth Edition, New York.

Herr, H. and Dennis, B., 2004, “A Swimming Robot Actuated by Living Muscle Tissue”, *Journal of NeuroEngineering and Rehabilitation*
http://biomech.media.mit.edu/images/pro_2/Muscle_Robot_Final.pdf
(Included in CD – Download Date: 11.12.2004)

Hirata, K., Takimoto, T. and Tamura, K., 2000, “Study on turning performance of a fish-robot”, *First International Symposium on Aqua Bio-Mechanisms*, pp. 287-292.

Hirata, K., 2000, “Development of Experimental Fish Robot”, *Sixth International Symposium on Marine Engineering*, pp.711-714.

Hirata, K., 2001a, "A Semi Free Piston Stirling Engine for a Fish Robot", *Proceedings of 10th International Stirling Engine Conference*, pp. 146-151.

Hirata, K., 2001b, "Stirling Engine for a Fish Robot, S-FPSE 2000", http://www.nmri.go.jp/eng/khirata/stirling/sfpse/fpse02/index_e.html,
(Included in CD – Download Date: 11.07.2004)

Hsu, S., Mailey, C., Eade, E. and Janét, J., 2003 "Autonomous Control of a Horizontally Configured Undulatory Flap Propelled Vehicle", *Proc. IEEE, Intl' Conference on Robotics & Automation*, pp. 2194-2199.

IEEE, 1988, "IEEE Standard on Piezoelectricity," ANSI/IEEE Std. 176-1987, New York: IEEE.

Ishihara, H., Arai, F. and Fukuda, T., 1996 "Micro Mechatronics and Micro Actuators", *IEEE/ASME Transactions on Mechatronics*, Vol. 1, pp. 68-79.

Jaffe, B., Cook, W. R. and Jaffe, H., 1971, *Piezoelectric Ceramics*, Academic Press, New York.

Kato, N., 2004, "Fish Fin Motion",
[Url:http://www.naoe.eng.osaka-u.ac.jp/naoe/naoe3/kato/fin9.html](http://www.naoe.eng.osaka-u.ac.jp/naoe/naoe3/kato/fin9.html)
(Included in CD – Download Date: 19.07.2004)

Kato, N., 2000, "Control performance in the horizontal plane of a fish robot with mechanical pectoral fins", *IEEE Journal of Oceanic Engineering*, Vol. 25(1), pp. 121 – 129.

Kato, N. and Furushima, M., 1996, "Pectoral fin model for maneuver of underwater vehicles," *Proc. 1996 IEEE AUV Symp.*, pp. 49–56.

Kato, N., Wicaksono B. W. and Suzuki, Y., 2002, "Development of Biology-Inspired Autonomous Underwater Vehicle 'BASSIII' with High Maneuverability", *Proceedings of the 2000 International Symposium on Underwater Technology*, pp. 84-89.

Koc, B., Cagatay, S. and Uchino, K., 2002, "A Piezoelectric Motor Using Two Orthogonal Bending Modes of a Hollow Cylinder", *IEEE UFFC*, Vol. 49, no. 4, pp. 495-500.

Kurosawa, M. and Ueha, S, 1991, "Hybrid transducer type ultrasonic motor", *IEEE UFFC* Vol. 38, no. 2, pp. 89-92"

Laurent G. and Piat, E., 2001, "Efficiency of Swimming Microrobots using Ionic Polymer Metal Composite Actuators", *Proceedings of the 2001 IEEE Intl. Conf. on Robotics & Automation*, pp. 3914-3919.

Lighthill, M. J., 1960, "Note on the Swimming of Slender Fish," *Journal of Fluid Mechanics*, Vol. 9, pp. 305-317.

Lin, C.-Y. , 1997, "Design and Analysis of Piezoelectric Transformer Converters", Ph.D. Dissertation,

<http://www.scholar.lib.vt.edu/theses/available/etd-82097-163753/unrestricted/diss0917.pdf>

(Included in CD – Download Date: 21.12.2004)

Madden, J., Zimit, R., Vandesteeg, N., Madden, P., Anquetil, P., Lafontaine, S., Takshi, A., Hunter, I. and Wierenga, P., 2004, "Artificial Muscle Technology: Physical principals and naval prospects", *IEEE Journal of Oceanic Engineering*, Vol. 29(3), pp. 706-728.

Magsoft Corporation, 2004, "Homepage", <http://www.atilafem.com>,

(download date: 1.11.2004),

Meirovitch, L., 1967, *Analytical Methods in Vibration*, The Macmillan Comp., New York.

Microchip, 2004, "12F675 Datasheets",

<http://ww1.microchip.com/downloads/en/DeviceDoc/41190c.pdf>

(Included in CD – Download Date: 18.12.2004)

Mojarrad, M. and Shahinpoor, M., 1997, "Biomimetic Robotic Propulsion Using Artificial Muscles", *Proceedings of the 1997 IEEE Intl. Conf. on Robotics and Automation*, Vol. 3, pp. 2152-2157.

Mojarrad, M., 2000, "AUV Biomimetic Swimming", *OCEANS 2000 MTS/IEEE Conference and Exhibition*, Vol. 3 , pp. 2141 – 2146.

Morgansen, K., 2004, "Fish Project",
<http://vger.aa.washington.edu/fishproject.htm> ,
(Included in CD – Download Date: 11.07.2004)

Morgansen, K., 2004, "Modelling and Control of Fin Actuated AUV",
<http://vger.aa.washington.edu/presentations/ngc-040402.pdf>,
(Included in CD – Download Date: 11.07.2004)

Morita, T., 2003, "Miniature piezoelectric motors", *Sensors and Actuators A*, Vol. 103, pp. 291-300.

Moyle, P. B. and Cech., J. J., 2004, *An Introduction to Ichthyology*, Pearson Prentice Hall, Upper Saddle River, NJ,USA, 5th Edition.

Nakabo, Y., Mukai, T., Ogawa, K., Ohnishi, N. and Asaka, K., "Biomimetic Soft Robot Using Artificial Muscle",
[www.bmc.riken.jp/~sensor/papers/IROS2004\(Nakabo\).pdf](http://www.bmc.riken.jp/~sensor/papers/IROS2004(Nakabo).pdf)
(Included in CD – Download Date: 11.12.2004)

Nakamura, K., Kurosawa, M., Kurebayashi, H. and Ueha, S., 1991, "An Estimation of Load Characteristics of an Ultrasonic Motor by Measuring Transient Responses", *IEEE UFFC*, Vol. 38, No. 5.

National, 2004, "P/N LM2917 - Frequency to Voltage Converter",
<http://www.national.com/ds.cgi/LM/LM2907.pdf>
(Included in CD – Download Date: 18.12.2004)

NewScientist, 2001, “Muscling in”, <http://www.newscientist.com> , 21 February 2001.

Niezrecki, C., Brei, D., Balakrishnan, S. and Moskalik, A., 2001, “Piezoelectric Actuation: State of the Art”, *The Shock and Vibration Digest*, Vol. 33, no. 4, pp.269-280.

NMRI, 2000a, “Fish Robot Home Page”,
URL: http://www.nmri.go.jp/env/khirata/index_e.html,
(Included in CD – Download Date: 14.09.2004)

NMRI, 2000b, “Model Fish Robot, PPF-09”,
URL: <http://www.nmri.go.jp/eng/khirata/fish/model/ppf09/index.html>,
(Included in CD – Download Date: 14.09.2004)

Philips, 2004, “BD135; BD137; BD139; NPN power transistors”,
http://www.semiconductors.philips.com/acrobat/datasheets/BD135_137_139_3.pdf
(Included in CD – Download Date: 18.12.2004)

Rao, S., S, 1995, *Mechanical Vibrations*, Addison-Wesley Publishing Company, USA, Third Edition.

Robot Shark, 2004, <http://news.bbc.co.uk/1/hi/england/devon/3083759.stm>
(Included in CD – Download Date: 09.07.2004)

Rogacheva, N. N., Chou, C. C. and Chang, S. H., 1998, “Electromechanical analysis of a symmetric piezoelectric/elastic laminate structure: theory and experiment”, *IEEE Transactions on UFFC*, Vol. 45, No. 2, pp. 285-294.

Sfakiotakis, M., Lane, D. M. and Davies, B. C., 2001, “An Experimental Undulating-Fin Device Using the Parallel Bellows Actuators”, *IEEE, Proceedings of International Conference on Robotics and Automation*.

Sitti, M. and Behkam, B., 2004, "E.Coli Inspired Propulsion for Swimming Microrobots", *Proc.IMECE'04, International Mechanical Engineering Conference and R&D Exposition*, Anaheim.

Thielicke, E. and Obermeier, E., 2000, "Microactuators and Their Technologies", *Mechatronics*, Vol. 10, pp. 431-455.

Tomikawa. Y., Tkano T. and Umeda H., 1992, "Thin rotary and linear ultrasonic motors using a double-mode piezoelectric vibrator of the first longitudinal and second bending modes", *JJAP*, Vol. 31, part1, no.9B, pp. 3073-3076.

Tong, J., Cui, T., Shao, P. and Wang, L., 2003, "Piezoelectric Micromotor Based on the Structure of Serial Bending Arms", *IEEE UFFC*, Vol. 50, No. 9

Toshiba, 2004, "TOSHIBA Photocoupler",
www.toshiba.com/taec/components/Datasheet/TLP250.pdf,

(Included in CD – Download Date: 18.12.2004)

Towtank, 2004, "MIT Towing Tank", <http://web.mit.edu/towtank/www/>,

(Included in CD – Download Date: 11.07.2004).

Triantafyllou M. S., Triantafyllou G. S. and Gopalkrishnan, R., 1991, "Wake Mechanics for Thrust Generation in Oscillating Foils", *Phys. Fluids A-Fluid*, Vol. 3, No. 12, pp. 2835-2837.

Triantafyllou, G. S, Triantafyllou, M. S. and Grosenbaugh M. A., 1993, "Thrust development in oscillating foild with application to fish propulsion", *J Fluid Struct.*, Vol. 7, No: 2, pp. 205-224.

Triantafyllou, M. S. and Triantafyllou, G. S., 1995, "An Efficient Swimming Machine", *Scientific American*, Vol. 272, Issue 3, pp. 64-70.

Triantafyllou, M. S., Triantafyllou, G. S. and Yue D. K. P., 2000, "Hydrodynamics of fishlike swimming", *Annu. Rev. Fluid Mech.*, Vol. 32, pp. 33-53.

Trimmer, W. and Jebens, R., “Actuators for Micro Robots,” *Proceedings of IEEE International Conference on Robotics and Automation*, Vol. 3, pp. 1547 – 1552, 1989

Tsai, J.-F. and Lo, C.-W., 2002, “Study on the Resistance and Propulsion Performance of Biomimetic Autonomous Underwater Vehicle,” *Proceedings of the International Symposium on Underwater Technology*, pp. 167 – 171.

Tunçdemir, S. and Koç, B., 2004, “Piezoelectric motor using first longitudinal and third flexural modes of a cantilever beam”, *Proceedings of 9th International Conference on New Actuators (ACTUATOR2004)*, Bremen.

Tunçdemir, S, Koç, B. and Erden, A., 2004, “Design of a Mini Swimming Robot”, *Proc. the 9th International Conference on Mechatronics (Mechatronics 2004)*, Ankara.

Tzeranis, D., Papadopoulos, E. and Triantafyllou, G., 2003, “On the Design of an Autonomous Robot Fish”, *Proc. 11th IEEE Mediterranean Conference on Control and Automation (MED03)*, Rhodes.

Uchino, K. 1997, *Piezoelectric Actuators & Ultrasonic Motors*, Kluwer Academic Pub., Boston.

Uchino, K., 2002, “Piezoelectric Actuators 2002: New Material, Design and Drive/Control Related Issues”, *Proceedings of 8th International Conference on New Actuators (ACTUATOR2002)*, Bremen

Uchino, K. and Koc, B., 1999, “Compact Piezoelectric Ultrasonic Motors”, *Ferroelectrics*, Vol. 230, pp. 73-86.

Ueha, S, Tomikawa, Y, Kurosawa, M. and Nakamura, N., 1993, *Ultrasonic Motors: Theory & Applications*, Clarendon Press, Oxford.

VideoRay, 2004, "VideoRay ROV - Micro Submersible - Inspection Class Remotely Operated Vehicles", <http://www.videoray.com/>
(Included in CD – Download Date: 09.07.2004)

Waldron, K. J. and Hubert, C., 2000, "Scaling of Robotic Mechanisms", *Proceedings of IEEE, ICRA-2000*, pp. 40-45.

Washington, G., 2004, "The Intelligent Structures and Systems Laboratory, Miniature Swimming Vehicles,
URL: <http://rclsgi.eng.ohio-state.edu/~gnwashin/parts/swim.html>
(Included in CD – Download Date: 05.11.2004).

Webb, P. W., 1992, "Is the high cost of body caudal fin undulatory swimming due to the increased friction drag or inertial recoil", *Journal of Experimental Biology*, Vol. 162, pp. 157-166.

Williamson, M., M., 1995, "Series Elastic Actuators", MIT MS Thesis.
<http://citeseer.ist.psu.edu/cache/papers/cs/26155/ftp:zSzzSzpublications.ai.mit.edu/zSzaipublicationszSzpdfzSzAITR-1524.pdf/williamson95series.pdf>
(Included in CD – Download Date: 21.12.2004)

Wu, T. Y., 1960, "Swimming of a Waving Plate", *Journal of Fluid Mechanics*, Vol. 10, pp. 321-344.

Wu, T. Y., 1971, "Hydromechanics of Swimming Propulsion, Part 1. Swimming of a Two-Dimensional Flexible Plate at Variable Forward Speeds in an Inviscid Flow", *Journal of Fluid Mechanics*, Vol. 46, part 2, pp. 337-355.

Yamamoto, I., Terada, Y., Nagartau, T. and Imaizumi, Y., 1993, "Research on an Oscillating Fin Propulsion Control System", *OCEANS '93 'Engineering in Harmony with Ocean' Proceedings*, IEEE III/259-III/263, Vol. 3.

Yamamoto, I., Terada, Y., Nagartau, T. and Imaizumi, Y., 1995, "Propulsion System with Flexible/Rigid Oscillating Fin", *IEEE Journal of Oceanic Engineering*, Vol. 20(1), pp. 23-30.

Yu, J., Wang, S. and Tan, M., 2003, "Design of a Free-swimming Biomimetic Robot Fish", *Proceedings of the 2003 IEEE/ASME Intl' Conf. on Advanced Intelligent Mechatronics (AIM2003)*, pp. 95-100.

Yu, J., Tan, M., Wang, S. and Chen, E., 2004, "Development of a Biomimetic Robotic Fish and Its Control Algorithm", *IEEE Transactions on Systems, Man and Cybernetics-Part B: Cybernetics*, Vol. 34, No. 4.

APPENDIX A

OBTAINING L1

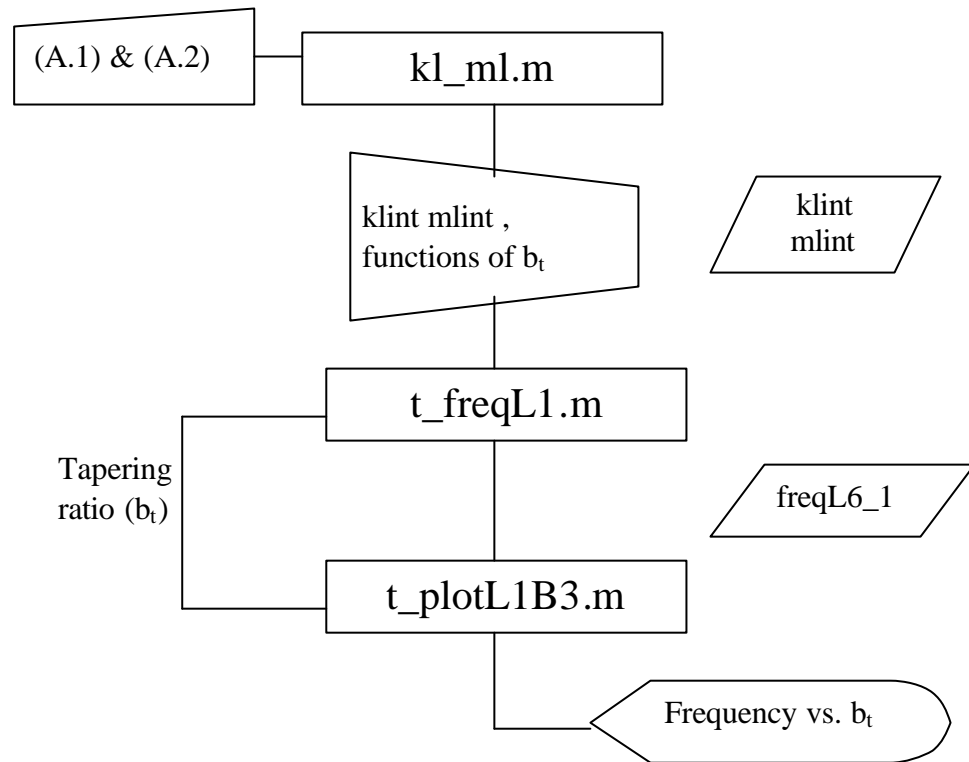


Figure A.1: Flowchart of the method for obtaining L1 frequency explicitly.

kl_ml.m

Integrands of 4.59 and 4.60, which are given in (A.1) and (A.2) are implemented in the function *kl_ml.m*

$$V_i \left((b_r - 1)u \cdot V_i' + (1 + (b_r - 1)) \cdot V_j'' \right) \quad (\text{A.1})$$

$$V_i \cdot (1 + (b_r - 1)u) \cdot V_j \quad (\text{A.2})$$

Integrals are evaluated explicitly from $u= 0$ to 1 , by using the symbolic toolbox of MATLAB. Results are stored in two 6×6 matrices, $klint$ and $mlint$ for stiffness and mass related terms.

$$klint = \frac{k_{ij}}{K_1 b_0} \quad (A.3)$$

$$mlint = \frac{m_{ij}}{m_1 b_0} \quad (A.4)$$

Table A.1: Functions used in the solution given in Appendix A

name	inputs	outputs	comments
kl_ml	Integrands of 4.59 and 4.60 are implemented as a function of u and b_t	$klint = \frac{k_{ij}}{K_1 b_0}$, $mlint = \frac{m_{ij}}{m_1 b_0}$	Output is the integral array of (4.59) and (4.60) in the form of 6×6 matrix as a function of tapering ratio.
tfreq_L1	tapering ratio, $klint$, $mlint$	$freqL6_1 = \frac{freq_{L1} \cdot 2p}{\sqrt{\frac{K_1}{L^2 \cdot m_1}}}$	Frequency (without the constant parts) is obtained by solving (4.58).
t_plotL1B3	L , h_p , h_e , s_{11}^E , k_{31} , b_t and mass density can be changed inside the code.	Plot of $L1$ as well as B3 for different b_t and h/L ratio.	t_freqL1 is called inside the code for various b_t .

t_freqL1.m

Arrays *k* and *m* are implemented as a function of tapering ratio b_t , manually in *t_freqL1*. x is the input to the function for tapering ratio.

$[k^*]\{a\} = \omega^2 [m^*]\{a\}$ is solved leading to an eigenvector. First element is taken out which is *freqL6_1*

$$\text{freqL6_1} = \frac{\text{freq}_{L1} \cdot 2p}{\sqrt{\frac{K_1}{L^2 \cdot m_1}}} \quad (\text{A.5})$$

t_plotL1B3.m

Material properties are entered the system. Tapering ratio (b_t) is sent to the functions *t_freqL1(x)* and *freqB3(x)* as input and *freqL6_1*, *freqB6_1* are returned. Constants are multiplied with *freqL6_1* and *freqB6_3* for obtaining the natural frequency corresponding to a specific b_t . Setting a thickness, first natural frequency of longitudinal vibration and third natural frequency of bending vibration are plotted for tapering ratio (b_t).

APPENDIX B

OBTAINING B3

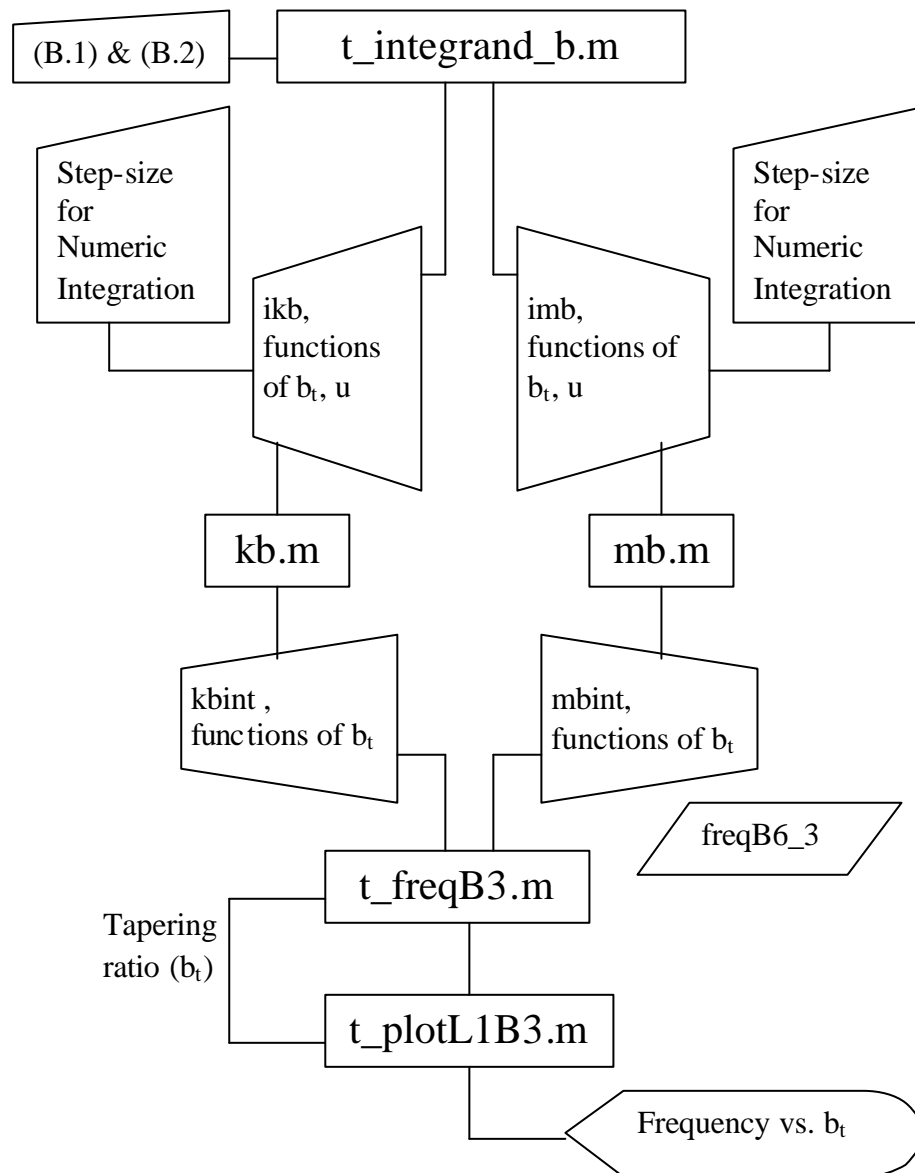


Figure B.1: Flowchart of the method for obtaining B3 frequency numerically.

Generated functions with their input and returning parameters and additional comments are tabulated in Table B.1, in hierarchical order.

Table B.1: Functions used in the solution given in Appendix B

name	inputs	outputs	comments
t_integrand_b	Integrands of (4.64) and (4.65) are implemented as a function of u and b_t	ikb, imb Output is the array of the integrands (4.64) and (4.65) in the form of 6x6 matrix as a function of tapering ratio and u.	For manual inputs in the required format for numerical integration in MATLAB.
mb kb	Manually entered ikb, imb	Numerically integrated stiffness/mass matrices kbint&mbint as a function of b_t	Boole's Rule with 4 segments over 1000 points for numerical integration of ikb and imb.
t_freqB3.m	Tapering ratio, Manually entered kbint, mbint	$freqB6_3 = \frac{freq_{B3} \cdot 2p}{\sqrt{\frac{K_2}{L^4 \cdot m_1}}}$	Frequency (without the constant parts) is obtained by solving (4.58).
t_plotL1B3	L, h_p , h_e , s_{11}^E , k_{31} , b_t and mass density can be changed inside the code.	Plot of L1 as well as B3 for different b_t and h/L ratio.	t_freqB3 is called inside the code for b_t .

t_integrand_b.m

Integrands of 4.64 and 4.65 which are given in (C.1) and (C.2) are implemented.

$$W_i \cdot \left((1 + (b_r - 1)u) \cdot W_j^{(4)} + 2(b_r - 1) \cdot W_j^{(3)} \right) \quad (\text{B.1})$$

$$W_i \cdot (1 + (b_r - 1)u) \cdot W_j \quad (\text{B.2})$$

Function *t_integrand_b.m* is utilized and *ikb(m,n)* and *imb(m,n)* are evaluated separately on command window (for $m=1..6$ and $n=1..6$) and each integrand is pasted to *kb.m*, *mb.m* by equating to [outkb11 ... outkb66].and [outmb11 ... outmb66] respectively.

kb.m, mb.m

Values of *ikb* and *imb* for t-segmented u domain are stored in two (t x 1) arrays of *outkbXX(t)* and *outmbXX(t)* in order to obtain integrands as a function of u. Numerical integrationz are performed utilizing *Boole's Rule* with 5 points, 4 segments over 1000 data points. Sum of the each integration is equated to the specific elements of 6x6 stiffness and mass matrix, *kbint* and *mbint*.

t_freqB3.m

kbint and *mbint* are loaded manually to the function and 6x6 stiffness and mass related matrices are formed as a function of b_r . x is the input to the function for tapering ratio

APPENDIX C

CALCULATION of MOMENT of INERTIA of LOAD on MOTOR

Polar moment of inertia for uniform disk shaped objects is expressed with the formula (C.1), where mass m is given with (C.2) and r is the radius of the disk.

$$J = \frac{1}{2}mr^2 \quad (C.1)$$

$$m = \rho \cdot \pi \cdot r^2 \cdot h \quad (C.2)$$

In C.2, ρ and h is used for the density of the material and thickness of the disk.

Equation (C.1) reduces to (C.3).

$$J = \frac{1}{2}\rho(\pi \cdot h \cdot r^4) \quad kg \cdot m^2 \quad (C.3)$$

Rotary load is assumed such that it is composed of two components, as the coupling disk and rotary disk of encoder neglecting the inertia of bearing used for rotor.

Coupling disk is machined from aluminum which has a specific density of 2800 kg/m³. Disk is composed of two sections with $h_1=3.5$ mm, $r_1=10$ mm and $h_2=7$ mm, $r_2=5.4$ mm.

Rotary disk of encoder is made up of two different materials in three sections, one of which is plastic with 500 kg/m^3 specific density and other two sections are made up of 2800 kg/m^3 specific density aluminum. Dimensions of aluminum sections are given as $h_1=8\text{mm}$, $r_1=6\text{mm}$, and $h_2=1\text{mm}$, $r_2=16.5\text{mm}$. Plastic section has the dimension of $h_3=0.2\text{mm}$, $r_3=25\text{mm}$

Generated MATLAB m-file for inertia calculation using (C.3) with the superposition of the inertias of different sections is given below

inertia.m

```
function result=inertia;
```

```
I1=0.5*2800*pi*(3.5*10^4+7*5.4^4)*10^-15;
```

```
I2=(0.5*2800*pi*(8*6^4+1*16.5^4)+0.5*pi*500*0.2*25^4)*10^-15;
```

```
I=I1+I2;
```

```
result=I
```

```
%result is returned in kg*m^2
```

```
return
```

APPENDIX D

MOTOR CHARACTERISTICS CALCULATIONS in MATLAB

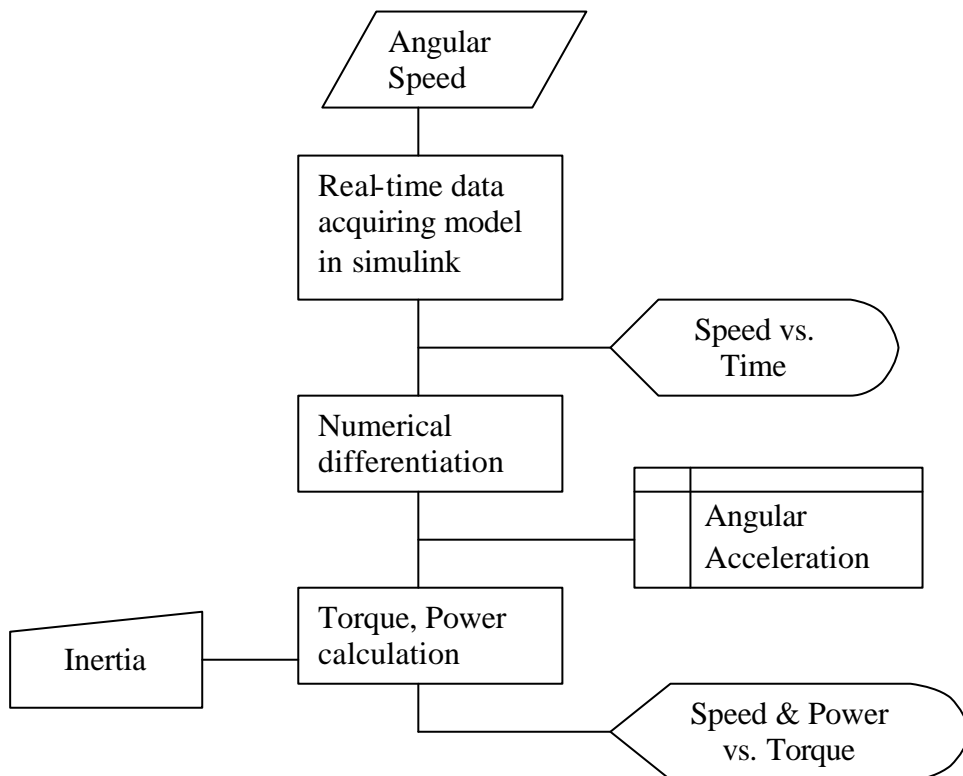


Figure D.1: Flowchart of the algorithm followed for obtaining motor characteristics from angular speed data via real-time data acquisition card.

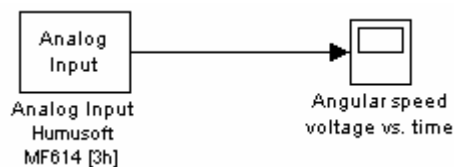


Figure D.2: Matlab Simulink[®] model for real time data acquisition.

Real time data representing the angular speed is taken from the I/O card as analog input and stored in MATLAB by means of the simple model given in Figure D.1. Properties of the scope in the model shown in Figure D.2 are arranged so that the input data (analog voltage) is stored in *torta.mat* data-file in 2 columns-array. In 2xn matrix first columns represents the time steps, while second is for the voltage values and n denotes the length of data acquisition time at 0.001 sample time. Function given below with name *character.m*, takes only a portion of the input data (between 7.055 and 7.8 seconds). The readout pulsewidth (One high and one low) from the optical encoder is 2.2ms. Thus, 1 revolution of 100-portioned encoder disk takes 220ms.

character.m

```
function character
time=torta(7055:7800,1)
time=time-7.054
speed=((2*pi/0.22)/4.570312500000000)*((torta(7055:7800,2))-torta(7055,2))
k=polyfit(time,speed,5)
N=polyval(k,time);
for i=2:745
    Nder1(i)=(N(i+1)-N(i-1))/0.002;
end
Nder1(1)=Nder1(2)
Nder1(746)=Nder1(745)
torque=inertia*Nder1';
for j=1:746
    power(j)=100000*torque(j)*speed(j);
end
Figure(1)
plot(torque,power,torque,(speed*30/pi))
title('power & speed vs. torque')
xlabel('torque (Nm)')
ylabel('speed , power')
legend('power (100 mW)','speed (RPM)')
Figure(2)
plot(time,(speed*30/pi))
title('speed vs. time')
xlabel('time (sec)')
ylabel('speed')
legend('revolution/minute')
```

APPENDIX E

FLAPPING ANGLE CONTROL USING PIC12F675

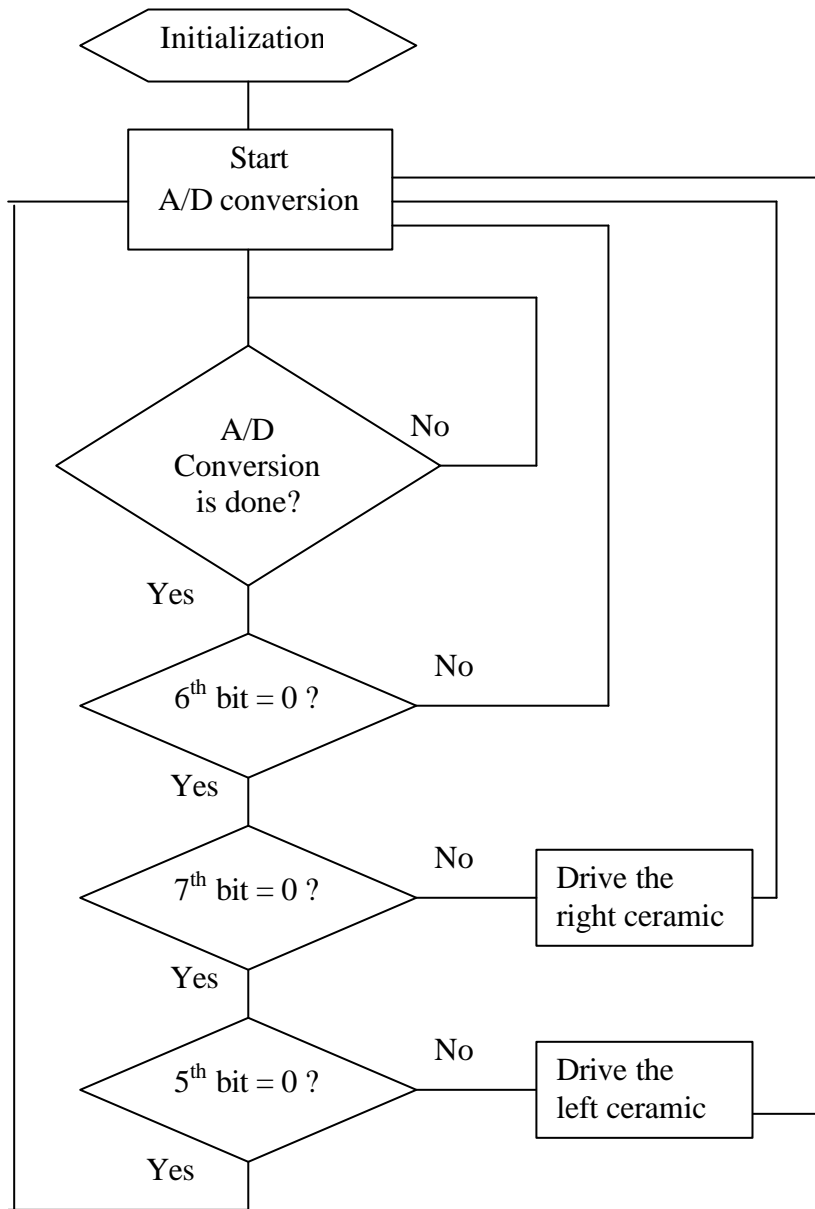


Figure E.1: Flowchart of the flapping angle control algorithm

In the algorithm, most significant three bits that are the 7th, 6th and 5th bits of A/D conversion output register are tested. According to A/D conversion result with 3-bit resolution, right or left ceramic is driven through photocoupler.

Assembler code of the algorithm sketched in Figure E.1 is given below for PIC12F675 microcontroller.

```

;control.asm
;written by Safakcan Tuncdemir
;Flapping tail control with PIC12F675
;Port3 is allocated for analog input from CNY-70
;Port0 and Port1 are allocated for driving
;the left and right optocouplers than the ceramic layers

        LIST P=12F675
        INCLUDE "P12F675.INC"

        BCF     STATUS,    RP0    ;BANK 0
        CLRF   GPIO        ;init GPIO
        MOVLW  07h         ;set GP<2:0> to
        MOVWF  CMCON       ;digital IO
        BSF    STATUS,    RP0    ;BANK1
        MOVLW  58h         ;0th bit input, osc time 16
        MOVWF  ANSEL       ;01011000
        MOVLW  18h         ;set GP<4,3> as inputs
        MOVWF  TRISIO      ;and set GP<5,2,1,0> as outputs
        BCF    STATUS,    RP0    ;BANK 0
        MOVLW  0Dh         ;00001100 to ADCON0
        MOVWF  ADCON0      ;4th channel is set
        CALL   DELAY

START
LOOP
        BSF    ADCON0,    1      ;initiate A/D conversion
        CALL   DELAY

TESTAD
        BTFSC  ADCON0,    1      ;test if A/D conversion is done
        GOTO   TESTAD          ;continue to test if not completed
        BTFSC  ADRESH,    6
        GOTO   LOOP
        BTFSC  ADRESH,    7
        GOTO   RIGHT
        BTFSC  ADRESH,    5
        GOTO   LEFT

```

```

                GOTO    LOOP                ;restart A/D conversion for '0' gray-
                                                ;level
LEFT
    BCF          GPIO,    0
    BSF          GPIO,    1
    GOTO        LOOP

RIGHT
    BCF          GPIO,    1
    BSF          GPIO,    0
    GOTO        LOOP

DELAY
    DECFSZ      $FF
    GOTO        DELAY
    RETURN

END

```